CHARACTERIZING THE MECHANICAL PROPERTIES OF THE GLENOHUMERAL CAPSULE: IMPLICATIONS FOR FINITE ELEMENT MODELING

by

Eric John Rainis

BS, University of Pittsburgh, 2004

Submitted to the Graduate Faculty of

School of Engineering in partial fulfillment

of the requirements for the degree of

Master of Science

University of Pittsburgh

2006

UNIVERSITY OF PITTSBURGH

SCHOOL OF ENGINEERING

This thesis was presented

by

Eric John Rainis

It was defended on

August 18, 2006

and approved by

Patrick J. McMahon, MD, Assistant Professor, Department of Orthopaedic Surgery, University of Pittsburgh Medical Center

Michael S. Sacks, PhD, W.K. Whiteford Professor, Department of Bioengineering

Jeffrey A. Weiss, PhD, Associate Professor, Department of Bioengineering, University of Utah

Thesis Advisor: Richard E. Debski, PhD, W.K. Whiteford Professor, Undergraduate Coordinator, Department of Bioengineering

CHARACTERIZING THE MECHANICAL PROPERTIES OF THE GLENOHUMERAL CAPSULE: IMPLICATIONS FOR FINITE ELEMENT MODELING

Eric John Rainis, MS

University of Pittsburgh, 2006

The glenohumeral joint is the most dislocated major joint in the body; however despite such a high rate of injury, the proper treatment protocol remains unclear. Rehabilitation has proved to be insufficient with an 80% chance of redislocation in teenagers and 10-15% chance after the age of 40. Following surgical repair, nearly 25% of patients still experience redislocation and complain of joint stiffness and osteoarthritis. In an attempt to improve these results, the normal function of the glenohumeral capsule has been evaluated using both experimental and computational methods. Recent data (strain and force patterns) suggests that the capsule functions multiaxially. Therefore, simple uniaxial methods may not be sufficient to fully characterize the tissue and identify the appropriate constitutive model of the tissue. Inconclusive data has been presented in the literature regarding the collagen fiber architecture and the mechanical properties of the capsule that make it unclear whether the capsule is an isotropic or a transversely isotropic material. For instance, the collagen fiber architecture has been shown by one researcher to be randomly distributed, while another researcher reported the fibers to be aligned. In addition, the axillary pouch has been shown to be the primary stabilizer of the glenohumeral joint in positions of extreme external rotation while the posterior region of the capsule has been shown to stabilize the joint in positions of extreme internal rotation. The rate of dislocations, however, is more frequent in the position of external rotation.

Therefore, the overall objective of this work was to utilize a combined experimental - computational methodology to characterize the mechanical properties of the axillary pouch and

posterior region of the glenohumeral capsule. Using an isotropic constitutive model, the stress-stretch relationship of the axillary pouch and posterior regions in response to two perpendicular tensile and finite simple shear elongations showed no statistical difference. Further, the constitutive coefficients of pure tensile and simple finite shear elongations in the direction parallel to the longitudinal axis of the anterior band of the inferior glenohumeral ligament (longitudinal) were able to predict the response of the same tissue sample in the direction perpendicular to the longitudinal axis of the anterior band (transverse). These similarities between the longitudinal and transverse elongations of the tissue imply that the capsule is an isotropic material and functions to resist dislocation the same in all directions, rather than just along the longitudinal axis of the anterior band of the inferior glenohumeral ligament, as previously thought. Further, the coefficients of the axillary pouch and posterior regions of the capsule showed no statistical difference, suggesting that these regions have similar mechanical properties, despite a difference in geometry. Thus, when developing finite element models of the glenohumeral capsule, an isotropic constitutive model should be utilized; and both the axillary pouch and posterior regions could be evaluated using the same coefficients. However, due to discrepancies when comparing the constitutive coefficients of tensile and shear elongations, an update to the constitutive model is required. With the proper representation of the glenohumeral capsule known, finite element models can be developed to pursue the understanding of normal joint function, including the effects of age and gender, as well as injured and surgically repaired joints.

TABLE OF CONTENTS

LIST OF TABLES

LIST OF FIGURES

PREFACE

I would like to acknowledge my thesis advisor, Dr. Richard Debski, for his continual guidance and support. He has given me many great opportunities to expand both my knowledge and research skills. In addition, I would like to acknowledge the clinical advisor on my thesis committee, Dr. Patrick McMahon, for not only his great clinical advice on the project, but also the great ways of showing the "big picture" of the project. Thank you both for your time and patience, and I wish you and your families the best in the years to come.

I would also like to take the time to thank the remaining members of my thesis committee, Dr.'s Sacks and Weiss. Dr. Sacks has added invaluable advice into the mechanical testing of soft tissues and was always willing to lend a helping hand. Dr. Weiss and his staff, particularly Steve Maas, have played a critical role in my thesis work, providing their expertise in the mechanical testing of soft tissues as well as computational modeling. Thank you all for you generous efforts and knowledge that you have given me.

Mentioning a few friends along the way... Susie Q, you have been a large contributor to my thesis work, from writing to experimenting. Thank you for all of the help along the way, and hopefully the good times in the 'Burgh will "keep on truckin'." Danny, we've been through some good times and bad times, but no matter what, we had fun. If we weren't out in the middle of the woods camping, driving up and down the coast of CA, or taking every mode of transportation available in Japan, we were kickin' it back in front of the movie theatre. I'm

looking forward to your return back to the home country, even if it is Oregon. Alexis, if it wasn't you, it was your parents that always had a way of making people laugh, no matter what the situation; even if it meant hijacking someone's pillow and taking it on many adventures… I look forward to many adventures back to Lewisburry to enjoy the home brewing of the Wickwires! I wish the best to all of you.

Ragan, where do I start… You have been the glue that holds me together lately. It is always a good thing to know that there is someone at home waiting to see you and ready to comfort you on bad days. The past couple of months have been quite hectic with our schedules culminating one day apart, but I think we've pulled through with flying colors. I look forward to the days to come, especially when those days are spent on tropical islands or other countries. Thank you for all of your comfort and support along the way, it has really meant a lot. As they say in Germany, Ich liebe dich.

Last, but certainly not least, I would like to thank my family. My brother Mike, you have been a role model of sorts, being so successful and keeping me striding towards the same level of success. It always amazes me that we have come to have such a good relationship, when it seems as though it were only yesterday that you were body slamming me in the backyard. Just remember though, I could always be waiting for you around the corner, paint can in hand… Mom and Dad, I could never even come close to thanking you enough for helping me this far. Your constant support in everything I've done in my life has always driven me farther and farther. I know it may have seemed as though I didn't appreciate it at times, but believe me, you have made me the person that I am today. Thank all of you from the bottom of my heart.

NOMENCLATURE

Abbreviations

APTL – Axillary pouch tensile longitudinal

APTT – Axillary pouch tensile transverse

APSL – Axillary pouch shear longitudinal

APST – Axillary pouch shear transverse

PTL – Posterior region tensile longitudinal

PTT – Posterior region tensile transverse

PSL – Posterior region shear longitudinal

PST – Posterior region shear transverse

Computational

W – Strain energy density

C_1, C_2 – coefficients of the strain energy density function

F – Deformation tensor

B – Left Cauchy-Green deformation tensor

I_1, I_2 – Invariants of the left Cauchy-Green deformation tensor

λ - Stretch tensor

T – Cauchy stress tensor

1.0 INTRODUCTION AND BACKGROUND

Stability of the glenohumeral joint is maintained through a complex interplay of active and passive constituents, where active refers to the musculature surrounding the joint and passive refers to the bony contact and soft tissue restraints. One of these soft tissue restraints is known as the glenohumeral capsule, and will be the primary focus of this work. The structure and function of the capsule has been analyzed by many in the past, and will be discussed in detail in Sections 1.1 and 1.2. Even with all of the research that has been performed, however, the specific contribution of each capsular region to stability has been debated and is still controversial.

1.1 STRUCTURE OF THE GLENOHUMERAL CAPSULE

The glenohumeral capsule is a sheet of fibrous tissue composed of variably thick regions (superior glenohumeral ligament, middle glenohumeral ligament, anterior and posterior bands of the inferior glenohumeral ligament) that surrounds the ball and socket glenohumeral joint. [1, 2] (Figure 1.1) Engineers and clinicians have interpreted the mechanical function of these variably thick regions as uniaxial ligaments, and as the primary contributors to stability of the joint. [3-6] Additionally, these structures have been the primary focus of research efforts for several

decades. Anatomic studies of cadaveric specimens [7-9] and observations during surgery [10-12] have been the most common methods used to elucidate their function. For

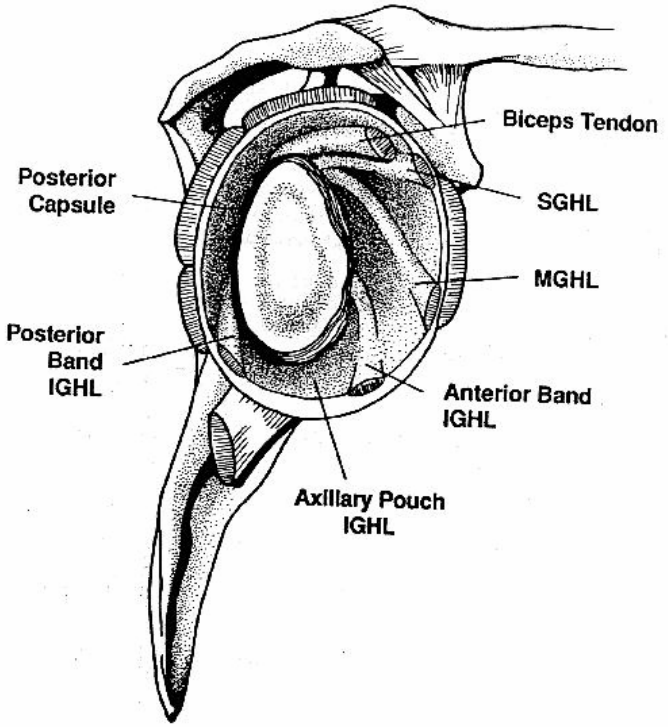

Figure 1.1: Lateral view of glenohumeral joint with humerus removed, showing regions of the capsule

instance, DePalma and coworkers [1] described the marked variability of the regions of the capsule and noted six types of anatomic arrangements that they believed could be correlated with the risk for anterior instability. Arthroscopic examinations have confirmed the high variability in size and appearance of the thickenings. [13-15]

In an effort to better understand the structure of the capsular regions, their collagen fiber orientation has been examined qualitatively by several researchers, [16-19] using standard and polarized light microscopy. Cooper and associates [19] demonstrated that the superior glenohumeral ligament has a ligamentous structure with collagen fibers organized parallel to the

longitudinal axis. O'Brien *et al* [17] reported that the axillary pouch was less organized than either the anterior band or posterior band of the inferior glenohumeral ligament (AB- and PB-IGHL). Furthermore, a great deal of crossing of the fibers was noted. In some shoulders, the anterior and posterior bands of the inferior glenohumeral ligament and the axillary pouch were best visualized by placing the humeral head in internal or external rotation in varying degrees of abduction. In contrast, Gohlke *et al* [16] found an organized pattern of collagen fibers in the axillary pouch with the fibers predominately organized parallel to the longitudinal axes of the anterior and posterior bands of the inferior glenohumeral ligament. Although both investigators [16, 17] reported that the fiber organization in the AB-IGHL was greater than in the axillary pouch, some discrepancy regarding the overall alignment in the axillary pouch remained. More recent studies have used a small angle light scattering (SALS) device to analyze the collagen fiber alignment in the axillary pouch and posterior regions of the glenohumeral capsule. [20] The results showed that localized regions had a preferred direction of alignment, suggesting a transverse isotropic organization; however on a global scale the fibers were disorganized, suggesting the overall structure of the tissue to be isotropic.

The structural and mechanical properties of the capsular regions have been measured under uniaxial tension applied in the direction parallel to their longitudinal axes. [3, 6, 21-26] The mechanical properties of four different sites (anterior, posterior, superior, and inferior) of the glenohumeral capsule have also been examined by Itoi and coworkers. [6] The posterior site exhibited the greatest ultimate stress and modulus compared to the other three sites tested, with the superior site having the least strength. No significant differences could be demonstrated between the ultimate loads of the four sites. In contrast, position dependent variations were found in the mechanical properties of the inferior site. Furthermore, the AB-IGHL was also examined

with the joint in the apprehension position. [23-26] The mechanical properties of the axillary pouch and posterior regions of the capsule have also been tested under uniaxial tension applied parallel and perpendicular to their longitudinal axes. [27] Significant differences were found for ultimate stress and tangent modulus between loading directions, however, no significant differences were found for ultimate strain and strain energy density between loading directions. Currently, with the inconclusive results regarding the mechanical properties and collagen fiber architecture that have been presented in the literature, the true nature of the glenohumeral capsule remains elusive.

1.2 FUNCTION OF THE GLENOHUMERAL CAPSULE

At the mid-range of motion, all capsular regions are relatively lax and contribute very little to joint stability [5, 28]. At end-range, extreme positions, however, the regions of the glenohumeral capsule play a significant role in stabilizing the joint. The roles of each capsular region are highly dependent upon the extreme joint position in question. Selective sectioning experiments have shown that the coracohumeral and superior glenohumeral ligaments limit external rotation in the lower range of abduction [5]. During the mid-range of abduction, the middle glenohumeral ligament and AB-IGHL provide anterior restraint, but at 90° of abduction the AB-IGHL and axillary pouch are the dominant anterior stabilizers. The axillary pouch, AB-IGHL, and anteroinferior capsular regions became the dominant restraint as abduction increased with the humerus externally rotated [29]. Malicky and coworkers [30] included the effect of the rotator cuff muscle forces on the ability of the capsular regions to provide joint stability. They

found that the anterior and inferior capsular regions were most effective at stabilizing the joint in positions of external rotation.

Other studies have attempted to quantify the contribution of the capsuloligamentous regions to joint stability by examining the changes in their length between the origin and insertion. These elongation patterns were determined using radiographic markers, [5, 31] electromagnetic tracking devices, [32] Hall effect strain transducers, [33] mercury strain gauges [34], and simple mathematical models. [35] A stereoradiogrammetric technique was also utilized to determine the strain field in sites of the anterior band of the the inferior glenohumeral ligament and axillary pouch during joint subluxation [36]. Lead spheres were adhered to the surface of the specified capsular tissue in a grid pattern and measurements were taken during a "nominal" and "strained" state. Maximum principal strain fields were greater on the glenoid side compared to the humeral side. Non-recoverable strain regions were found to exist throughout the specified capsular tissue after joint subluxation. This was the first attempt to examine the capsular tissue multiaxially.

Although a great deal of research has examined the strain within each capsular region, the force and stress remains largely unknown, with our knowledge base coming predominantly from qualitative observation and palpation during cadaver dissections [37, 38]. The forces in the capsuloligamentous regions were measured indirectly [34] using mercury strain gauges mounted on the surface of the capsule. As direct measurement of these forces is experimentally challenging due to the complexity of the joint geometry, [39] it has been suggested by Lew and coworkers that a computational model or finite element analyses of the capsule be developed.

To date, few analytical models of the glenohumeral joint have been developed [40, 41]. These models have been used to predict joint kinematics and investigate the stabilizing effect of

the capsuloligamentous regions and articular contact. However, uniaxial springs that wrapped around the articular surface of the humeral head were utilized and most modeled only specific portions of the capsule, disregarding the interactions that occur between capsuloligamentous regions. [20] These computational models of the glenohumeral capsule did not consider the effect of all the capsular regions and the 3D nature of the tissue was neglected.

1.3 DEMOGRAPHICS

The glenohumeral joint is the most commonly dislocated major joint in the body with dislocations occurring most often when the arm in an abducted and externally rotated position. The majority of these dislocations (>80%) occur in the anterior direction [42, 43], resulting in injury to the anterior portion of the inferior glenohumeral ligament. [25, 44-48] Approximately 2% of the general population (~5.6 million in the United States) dislocates their glenohumeral joint between the ages of 18-70 years. [49, 50] Roughly 34,000 shoulder dislocations occur per year in the young adult population between the ages of 15 to 25 years. [50, 51] Moreover, the activity level of the general population has increased over the last two decades. This increased level of activity has resulted in an increase in the incidence of dislocation in this age range of the population. [52, 53]

1.4 CLINICAL TREATMENT

1.4.1 Diagnosis

Anterior shoulder dislocations can be diagnosed with radiographs, which illustrate an anteroinferior displacement of the humeral head in relation to the glenoid. However, once the joint has been reduced, there is often little or no radiographic evidence of the dislocation. While techniques, such as magnetic resonance imaging, may reveal avulsion of the capsule from the glenoid rim, cases with a lesser degree of instability, such as a small increase in subluxation, are far more difficult to ascertain.

In such cases, physicians can use clinical exams that have been developed to generally assess which capsular regions are injured. Typically, these exams are performed when the arm is positioned in an abducted and externally rotated position (Figure 1.2). Because most patients are apprehensive to put their joint in this position for fear of redislocation, this position has been named the apprehension position and often indicates an injury may have occurred to the glenohumeral capsule regions that stabilize the joint in this position. The physician can then compare the injured shoulder to the contralateral shoulder to determine the extent of injury. In addition to determining the region of injury, physicians may also use the results of these exams to create a surgical plan.

However, these clinical exams are quite subjective due to movement of skin and musculature around the shoulder. In addition, there are discrepancies as to how much external rotation and abduction to use when examining the joint. A better understanding of the normal function of the joint may increase the accuracy and reliability of these procedures.

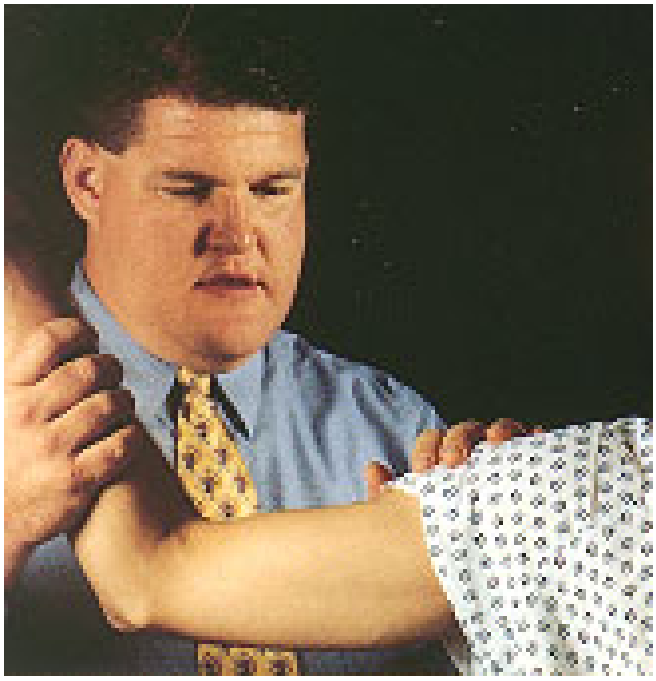

Figure 1.2: Clinical apprehension test with shoulder abducted and externally rotated [54]

1.4.2 Post-injury management

There are two basics types of protocols that can be used after shoulder dislocation. The first protocol is conservative with simple rehabilitation, in which a period of immobilization is allowed for soft tissue healing followed by exercises designed to increase the stability provided by the musculature that surrounds the joint. The second protocol that can be used is surgical repair, in which the physician will enter the joint space and attempt to repair the injury.

1.4.2.1 Conservative rehabilitation

Conservative treatment may include an initial immobilization period to allow soft tissue healing, followed by a rehabilitation program to strengthen and condition the shoulder muscles. These rehabilitation programs, however, have not been extremely successful as disability is common

after such treatments. Recurrence occurs in 60 to 94% of the patients under 25 years of age [44, 55-60], while in the elderly nearly 15% suffer weakness, pain, and loss of motion. [61] Therefore, patients typically require other forms of treatment, including surgical repair.

1.4.2.2 Surgical repair techniques

Given the outcomes of conservative treatment, surgical repair is often necessary. The most typical repair technique for anterior dislocations is known as the plicate and shift method, whereby the capsular tissue is both plicated and shifted in the medial-lateral and superior-inferior directions such that it can be reattached to the glenoid rim. [62, 63] This procedure involves first plicating the capsular tissue near either the glenoid or humeral head in the superior-inferior direction followed by another plication in the anterior-superior capsule in the medial-lateral direction. Finally, the created leaflets will be shifted and sutured to the either the glenoid or humeral head (Figure 1.3).

Unfortunately, surgical repair of the glenohumeral capsule is often ineffective at restoration of normal function. [62, 63] Redislocation rates are as high as 12 and 23% following open and arthroscopic surgical repairs, respectively, [64] and 20-25% of patients suffer from pain, chronic instability, rotator cuff injury, joint stiffness, and osteoarthritis.

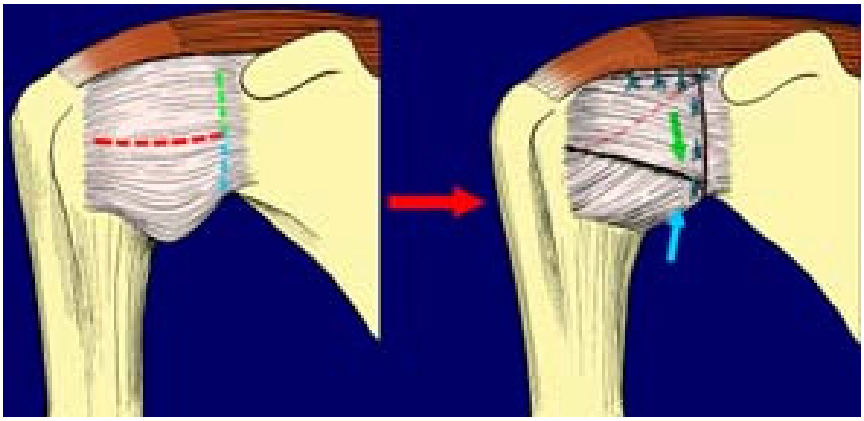

Figure 1.3: Plicate and shift surgical repair technique

These unsatisfactory clinical outcomes may be due to poor assessment of normal joint function pre- and post-operatively. Furthermore, these outcomes may be due to the fact that the surgical repairs may not restore the proper orientation of the collagen fibers throughout the capsule, greatly altering the function within and at the interface of the capsular regions. An inadequate understanding of the function of the regions of the normal glenohumeral capsule is likely to be part of the reason for the insufficient clinical planning and surgical repair techniques.

2.0 MOTIVATION: RESEARCH QUESTION AND HYPOTHESIS

The glenohumeral capsule is a complex sheet of tissue composed of several variably thick regions (superior glenohumeral ligament, middle glenohumeral ligament, anterior and posterior bands of the inferior glenohumeral ligament) that function collectively to stabilize the joint (Figure 1.1). [1, 2] Previously, these regions have been treated as discrete uniaxial ligaments, [5, 13, 30, 41] however, recent experimental data has suggested that the capsule functions more like a sheet of tissue, as their strain [36] and force [28] distributions are multiaxial and not aligned with the glenohumeral ligaments. For example, the capsule has a complex geometry as it wraps around the articular surface of the humeral head. This configuration presents many difficulties when evaluating the capsule's function experimentally. Computational approaches, such as the finite element method, can account for some of these complexities; however the proper constitutive model for this tissue is required. Inconclusive data regarding the collagen fiber architecture (aligned or random) [16, 20] and mechanical properties of the capsule (similar or different in perpendicular directions) [27, 65] has been presented in the literature, making it unclear which constitutive model is appropriate for the glenohumeral capsule.

2.1 MOTIVATION: SPECIFIC AIMS

The glenohumeral capsule functions to stabilize the glenohumeral joint in extreme ranges of motion. In particular, the axillary pouch stabilizes the joint in extreme positions of external rotation while the posterior region stabilizes the joint in extreme positions of internal rotation. [29] Even with both regions functioning to stabilize the joint, the axillary pouch is more often injured as the joint is dislocated more frequently in the position of external rotation, suggesting differences may exist between the mechanical properties of these regions.

Due to the complexity of the glenohumeral joint geometry as well as the multi-axial deformations of the tissue, it has been suggested by Lew and coworkers that a computational model or finite element analyses be developed. [58] However, when creating such a model, it is imperative that a constitutive model describing the stress-strain response of tissues be appropriate. While the capsuloligamentous regions have been evaluated extensively in the direction parallel to their longitudinal axes, [3, 6, 21, 22, 24, 26, 66] the mechanical response of the capsule in other directions remains largely unknown. Although there has been studies evaluating the mechanical properties in two perpendicular directions, [11, 62] dog-bone tissue samples were used, which may have removed important collagen fiber interactions, and large standard deviations in the mechanical properties were reported. Moreover, discrepancies exist regarding the collagen fiber organization of this tissue with some researchers finding a clear axis of collagen fiber alignment [74] while others have found a certain level of disorganization in capsuloligamentous regions. [17] In addition, these studies have primarily determined the mechanical response of the tissue in the linear region of the stress-strain curve, neglecting the toe region. Since during activities of daily living most soft tissues are only loaded into the toe region, this is an important region to characterize. Therefore, for the current work, there existed

a need to determine the appropriate constitutive model for the capsuloligamentous regions by using large sheets of tissue to minimize the removal of fiber interactions.

Due to the inconclusive data that has been presented in the literature regarding the collagen fiber architecture [16, 20] and mechanical properties [27, 65] of the capsule, it is unclear as to which constitutive model best represents its behavior. Therefore a protocol capable of characterizing both isotropic and anisotropic materials was essential. [67] Isotropic materials can be fully characterized by using simple tensile loading conditions in two perpendicular directions; however, anisotropic materials require additional loading conditions. Therefore, to allow for the possibility of an anisotropic material, tensile tests alone could not be used. Instead, a second loading condition was implemented to allow for the characterization of an anisotropic material. Since tensile loading is primarily used to characterize the contribution of the collagen fibers, finite simple shear loading was chosen as the second loading condition, allowing for the characterization of the fiber-fiber, fiber-matrix, and matrix-matrix interactions of an anisotropic material. [67] Unlike the infinitesimal strain theory, finite simple shear cannot be maintained by shear stress alone. [68] Normal stresses are needed to keep the normal strains minimized. In the absence of normal stresses, however, the tissue will undergo contraction through the thickness of the tissue as well as in the plane that the shear strains are applied. These contractions will create non-homogeneous strain fields that cannot be predicted without additional analyses. Two methods are capable of applying both tensile and finite simple shear elongations to sheets of tissue: planar bi-axial and bi-directional. [69] [70] Planar bi-axial methods apply elongations to tissue samples through hooks that are inserted along each edge of the tissue sample, while bi-directional methods utilize soft tissue clamps to apply elongations. These hooks can create stress concentrations in the tissue that are not easily predicted. However, because bi-directional testing

uses clamps instead of hooks to apply elongations to the tissue, they can be used in conjunction with computational methods, as described by Weiss, *et* al [69]. These computational analyses allow the non-homogeneous strains that occur during finite simple shear to be predicted. Therefore, because the material behavior of the glenohumeral capsule is unclear (isotropic versus transversely isotropic), and finite simple shear tests have been used in the past to characterize transversely isotropic materials such as ligaments [69], the method proposed by Weiss *et. al.* [69], which uses bi-directional methods, will be used. In addition, this method will characterize the entire stress-stretch curve, not just the linear region which has been reported in the past.

To ensure the appropriateness of the chosen constitutive model, it was required that it first be validated using experimental results. One such validation that can be used is the strains that are generated in the capsule during loading. To calculate these strains, a grid of small beads can be adhered to the surface of the tissue, and the motions of the beads can be tracked as the tissue deforms. Therefore, a method for tracking the deformation of beads that are on the surface of a tissue sample during loading was required. Another form of validation is to use optimized constitutive coefficients from one loading condition to predict the tissue's response for other loading conditions.

Once an appropriate constitutive model has been chosen and validated, differences in mechanical properties of the axillary pouch and posterior regions of the glenohumeral capsule can be assessed. This information will provide insight into which constitutive coefficients to use when developing finite element models. In addition to finite element modeling, understanding how each region functions will provide insight for physicians when surgically repairing the capsule. As discussed previously, a common surgical repair technique plicates and shifts the

capsule, however, due to the uncertainty of mechanical properties between regions this may alter the overall response of the capsule and thus not return the joint to its normal function.

2.2 RESEARCH QUESTIONS

Based on the inconclusive data that has been presented in the literature, the appropriate constitutive model for describing the behavior of the glenohumeral capsule remains unclear. In addition, because both the axillary pouch and posterior regions play a role in glenohumeral joint stability, yet the axillary pouch is more frequently injured; it is unclear if the mechanical properties of these regions differ. Recently, finite element models have been used to evaluate the function of the glenohumeral capsule. While a powerful tool, the finite element method must be properly applied with the appropriate constitutive models of the tissue of interest. This leads to the following research questions:

1. Is a hyperelastic isotropic constitutive model appropriate to describe the mechanical response of the glenohumeral capsule?

2. Are there differences in the mechanical properties of the axillary pouch and posterior regions of the capsule?

2.3 HYPOTHESES

Therefore, the following hypotheses were addressed by the current work:

Hypothesis #1 –Since the collagen fiber architecture is disorganized overall and there is evidence that there is no difference in certain mechanical properties in two perpendicular directions, a hyperelastic isotropic constitutive model will effectively describe the function of the glenohumeral capsule (R^2 of experimental and computational load-elongation curves > .9).

Hypothesis #2 – Because both the axillary pouch and posterior capsule function to stabilize the glenohumeral joint, there will be no significant differences in the mechanical properties between these regions.

2.4 SPECIFIC AIMS

These hypotheses were tested with the following specific aims:

Specific Aim #1 – Develop a multi-dimensional motion tracking system and evaluate the accuracy and repeatability in two testing environments

Specific Aim #2 – Evaluate the efficacy of using a hyperelastic isotropic constitutive model to represent the glenohumeral capsule by determining the constitutive parameters in response to tensile and finite simple shear elongations in two perpendicular directions

Specific Aim #3 –Compare the mechanical properties of the axillary pouch and posterior regions of the glenohumeral capsule

3.0 DEVELOPMENT OF MOTION TRACKING SYSTEM

3.1 INTRODUCTION

The purpose of developing a motion tracking system was to allow the motion of small beads on the glenohumeral capsule to be determined as loads are applied to the tissue, and then calculate the strain distribution on the surface of the tissue based on those motions. Many types of motion tracking systems have been reported in the literature, including stereoradiogrammetry [36, 71] and optical tracking systems [27, 36, 65, 69]. However, due to size limitations, stereoradiogrammetry would be unable to accomplish our goal. Therefore an optical motion tracking system was chosen.

Many different varieties of optical motion tracking systems exist in the literature to track the position of markers throughout time. [3, 27, 36, 69] To determine which system would be capable of accurately tracking motions of markers on the surface of the capsule in mechanical testing environments, multiple systems were analyzed.

3.1.1 Experimental environment

The primary use of this motion tracking system is to track the position of markers that have been placed on the surface of a tissue during loading. Two environments exist for which this system would be used - the mechanical testing environment, used in this thesis work, and a robotic

testing environment, which is used by others in our laboratory. In both cases, the system will be used to track the motion of markers, which will be used to calculate the surface strain of the tissue.

3.1.1.1 Mechanical testing environment

The mechanical testing environment (Figure 3.1a) is contained within an Enduratec ELF 3200 mechanical testing system and in general has an estimated working volume of 125 cm^3. A grid of nine (3 rows x 3 columns) markers will be applied to the tissue sample during mechanical testing, thus markers with a small diameter (1.6 mm) must be used. Because the assumption that minimal movement will occur out of the plan of the tissue, only a 2D camera configuration is required for this environment. Finally, marker motions during mechanical testing can range from 0 to 5 mm, thus an accuracy of at least 0.5% of the field of view is desired.

3.1.1.2 Robotic testing environment

The robotic testing environment (Figure 3.1b) is used during simulated clinical exams and is estimated at 1000 cm^3. A grid of 77 (7 rows x 11 columns) markers will be applied to the tissue during robotic tested, thus markers with a small diameter (1.6 mm) must be used. Because the capsule will wrap around the humeral head during these tests, a 3D camera configuration is required. Marker motions during robotic tests can range from 0 to 20 mm, thus an accuracy of at least 0.05% of the field of view is desired.

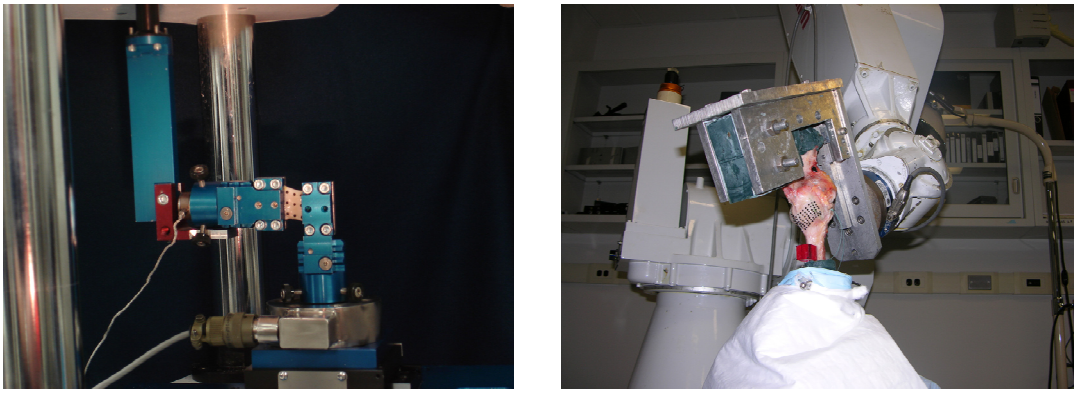

Figure 3.1: Mechanical testing (A) and robotic testing (B) environments

3.2 EXISTING OPTICAL TRACKING SYSTEMS

There are two general categories of optical tracking systems: active and passive. Active motion tracking systems have markers that are physically attached to the system via wires. These markers will then emit light, which can then be tracked by the camera system. Passive motion tracking systems have markers that have no connection to the system, and often reflect light that is emitted by the system or an outside source. Because active motion tracking systems are physically attached to the motion tracking system, it would be difficult to use such a system with either environment, due to interference between the wires and markers on the tissue, therefore only passive systems will be evaluated for the current work.

3.2.1 Vicon-Peak motion tracking system

A VICON 612 motion tracking system was evaluated for use with the current protocol. This system is designed to locate and track retroreflective markers moving in a calibrated measurement space. The system is designed primarily for use in biomechanics research and clinical medicine, in particular whole body kinematics. Marker trajectories are measured by

numerous 120Hz video cameras while the measurement space is illuminated by infra-red or visible-red strobe lights mounted on each camera. Illumination and video data collection is synchronized and controlled by the VICON 612 Datastation, which is in turn controlled by a Pentium-based PC running the Windows 2K operating system. From these files, the X, Y, and Z coordinates of each marker throughout time can be obtained.

3.2.2 Motion Analysis motion tracking system

Similar to Vicon, Motion Analysis systems are contrast based tracking systems that track the position of retroreflective markers throughout time. Motion Analysis, however, offers smaller camera systems that would be more flexible with our smaller working volume, and therefore was assessed for use with our protocol.

3.2.3 Spicatek motion analysis system

Unlike Vicon and Motion Analysis, Spicatek systems do not use retroreflective markers. Instead, Spicatek systems use live video feeds from high speed digital cameras, and then post-process the images based on contrast levels. Unlike Vicon and Motion Analysis, this system would provide a digital video record of each experiment, allowing the close inspection of the experiment if oddities arise in the experimental data as well as the ability to reprocess the data. Since this system is capable of outputting X, Y, and Z coordinates of markers throughout time, it was assessed for use with this protocol.

3.3 METHODS OF ASSESSMENT

3.3.1 Vicon motion tracking system

To assess the Vicon motion tracking system, a Vicon 612 system in the Human Movement and Balance Lab at the University of Pittsburgh was used. Because the actual experimental environments could not be used, simulations were created. The robotic environment was simulated first by creating a six degree of freedom device that modeled the approximate working volume. (Figure 3.2) The system was then calibrated using a custom made frame that was scaled to the original calibration frame provided by Vicon. A Sawbones model of the glenohumeral joint, with a sheet of rubber simulating the glenohumeral capsule was placed within the simulated robotic environment and a grid of 60 retroreflective markers (6 rows x 10 columns) were adhered to the rubber capsule. The joint was then placed in 90° of external rotation and 60° abduction, simulating a clinical exam. In this position, the 3D location of the markers was recorded and exported for post processing.

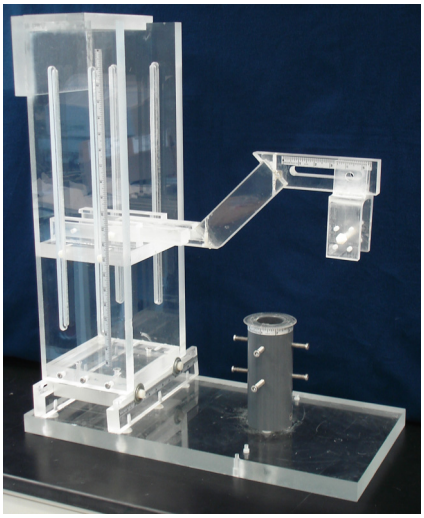

Figure 3.2: Simulated robotic testing environment

During post processing, it was noted that many of the markers were not visible due to the fact that only one camera was able to capture the location of those markers. For this system to track markers in 3D space, at least three cameras are required to locate a particular marker in space.

In addition to this simple test, another test, in which saline was sprayed onto the capsule and markers, was performed. Since the capsule is exposed to air for extended amounts of time during robotic tests, it is imperative to continuously moisten it with saline to prevent degradation and dehydration of the tissue. Therefore this test was used to identify any issues that the camera system may have with wet tissue and markers, in particular reflections that would be caused by the saline pooling on the tissue.

Once the markers were wet with saline, the camera system was no longer able to track the position of the markers because the retroreflectiveness of the markers was reduced. Therefore, under normal conditions the system had difficulty tracking the positions of some markers and became worse when the markers were covered by saline, this system was decidedly not capable of meeting our requirements.

3.3.2 Motion Analysis tracking system

Since the Motion Analysis system is similar to the Vicon system, in that it uses retroreflective markers, the first step of assessment was to determine whether the system was capable of tracking saline soaked markers. To assess this, a camera was positioned in front of a saline tank filled with saline. The field of view of the camera encompassed both the saline tank and the area above the tank. A marker was placed on the tip of a metal rod and translated in the field of view

of the camera, in and out of the saline tank. The camera system was successful in tracking the marker when it was above the tank, however, when the marker was placed in the saline tank; it disappeared from the camera's view. In addition, when the marker was removed from the tank and waived above the tank, the system was still unsuccessful at tracking the marker due to it absorbing the saline. Therefore, no additional analyses were performed with this system, as it was incapable of meeting this requirement of our protocol.

3.3.3 Spicatek motion analysis system

To assess the Spicatek system, like the Motion Analysis system, the first step was to verify its capabilities of tracking saline soaked markers. A camera was positioned in front of a saline tank filled with saline. The field of view of the camera encompassed both the saline tank and the area above the tank. A marker was placed on the tip of a metal rod and translated in the field of view of the camera, in and out of the saline tank. The camera system was successful in tracking the marker when it was above the tank, as well as when the marker was placed in the saline tank. In addition, when the marker was removed from the tank and waived above the tank, the system was still successful at tracking the marker while it was soaked with saline. Therefore, further analyses were performed with this system to assess parameters such as accuracy and repeatability.

3.3.3.1 System calibration

Calibrating a motion tracking system consists of outlining the working volume that will be used during testing by using specially designed calibration frames that contain markers at known

distances apart. Two camera configurations (1 camera for 2D, 2 or more cameras for 3D) were calibrated. For a 2D camera configuration, a black piece of acrylic with a perfectly planar face was covered by a 4x4 grid of white delrin markers (1.6 mm diameter – 10 mm apart). (Figure 3.3A) The choice of white and black was based on the requirement of contrasting colors, due to the system tracking markers based on contrast. A coordinate measuring machine (Brown & Sharpe, Gage 2000, accuracy – 0.005 mm) was then used to determine the exact positions of those markers with respect to each other, and those relationships were input into the Spicatek system software (DMAS6). The software then used embedded direct linear transforms to compare the coordinate measuring machines measured locations of the markers to the software's calculated position and determine the system's calibration.

For a 3D camera configuration, an aluminum calibration frame was used, and consisted of three separate tiers with black delrin markers (1.6mm diameter - ~40 mm apart) on each tier. (Figure 3.3B) The frame was painted white to increase the contrast between the frame and the markers. The choice of black markers on a white background for the 3D setup was due to the fact that the robotic environment is primarily white, therefore black markers served as a better contrasting color. A coordinate measuring machine (Brown and Sharpe, Global Image 998, accuracy – 0.0064 mm) was used to determine the location of the markers with respect to a specified corner of the frame.

With both setups, the calibration frame was positioned such that the specimen was centered within the working volume, and the markers were digitized using the Spicatek software.

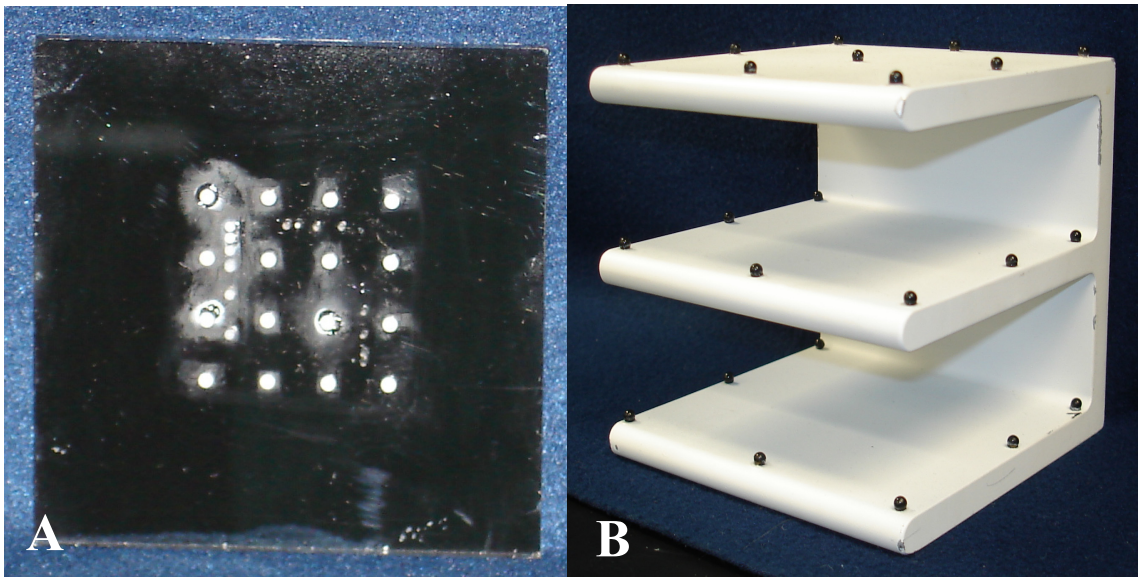

Figure 3.3: Calibration frame for 2-D (A) and 3-D (B) camera setups

3.3.3.2 Accuracy assessment

To determine the accuracy of both camera configurations, two markers were placed on a linear translation stage (accuracy: 24μm) and translated known distances while the camera tracked the position of those markers. The 2D camera configuration was tested by fixing one marker, and translating the other marker known distances of 0.25, 0.5, 1, 3, and 5 mm. The distance between those markers was then calculated based on the known translations of the linear stage, as well as the coordinates output by the camera system. The accuracy was then determined as the largest difference between the known translations and the measured translations.

The 3D camera configuration was tested in a similar manner; however since it is capable of tracking 3D positions, a third dimension was required. Therefore, the linear translation stage was rotated to an oblique angle from the cameras, meaning the markers would now translate in the X, Y, and Z directions, with respect to the camera's coordinate system. Again, a set of known distances (0.5, 1, 3, 5, 10mm) were used to compare the distance that was actually

applied to the distance that the camera system measured. The translations used in the 3D configuration were larger, based on the expected motion of markers while using this configuration. The accuracy was again determined as the largest difference between the known translations and the measured translations.

3.4 RESULTS

3.4.1 Calibration

Both 2D and 3D camera configurations were successfully calibrated using the custom-made calibration frames that were discussed in Section 3.3.3.1. The 2D camera configuration is capable of being calibrated to an accuracy of 0.005% of the field of view of the camera in both the X and Y directions. The field of view that is typically used for this configuration (mechanical testing) is approximately 20 cm in the X direction and 20 cm in the Y direction. This correlates to a calibrated accuracy of 0.01mm in both the X and Y directions, where the calibrated accuracy is the error when comparing the distance between markers determined by the camera system to the distance between markers that was input into the system (determined using a coordinate measuring machine, Section 3.3.3.1). The 3D camera configuration is capable of being calibrated to an accuracy of 0.03% of the field of view of each camera in the X, Y, and Z directions. The field of view that is typically used for this configuration (robotic testing) is approximately 1000 mm in all three directions, meaning that the 3D camera configuration can be calibrated to an accuracy of approximately 0.3 mm in the X, Y, and Z directions.

3.4.2 Accuracy

The 2D camera configuration was shown to have an overall accuracy of .008 mm. This was the largest difference between the known translations and the measured translations. (Table 3.1) The 3D camera configuration was shown to have an overall accuracy of 0.05 mm. (Table 3.2) Although much larger than that of the 2D camera configuration, it is important to note that this accuracy is well within the desired accuracy during robotic testing, where marker translations can be as large as 20 mm.

Table 3.1: Accuracy assessment of the 2D camera configuration

Prescribed motion(mm)	0.25	0.5	1	3	5
Measured motion (mm)	0.2499	0.4997	0.9992	2.9969	4.9918
Abs. Error (mm)	**0.0001**	**0.0003**	**0.0008**	**0.0031**	**0.0082**
% Error	**0.0267**	**0.0576**	**0.0799**	**0.1034**	**0.1634**

Table 3.2: Accuracy assessment of the 3D camera configuration

Prescribed motion(mm)	0.5	1	3	5	10
Measured motion (mm)	0.47	0.96	2.95	4.96	9.95
Abs. Error (mm)	**0.03**	**0.04**	**0.05**	**0.04**	**0.05**
% Error	**6**	**4**	**1.68**	**0.8**	**0.5**

3.5 CONCLUSIONS

All design criteria have been met with the current motion tracking system. The desired accuracy for both the 2D camera configuration (mechanical testing environment) and the 3D camera configuration (robotic testing environment) has been achieved. Therefore, this system can be used with confidence to track the motion of markers and allow the calculation of the strain distribution on the surface of the capsule as loads are applied. In addition, the camera system can be used to determine accurate tissue sample geometries during mechanical testing protocols.

4.0 CHARACTERIZATION OF THE GLENOHUMERAL CAPSULE

4.1 INTRODUCTION

Summarizing the combined experimental and computational methodology described by Weiss, *et al* [67], a total of four non-destructive loading conditions were applied to each tissue sample of the axillary pouch and posterior regions. Specifically, two perpendicular tensile and finite simple shear (parallel to the long axis of the AB-IGHL – longitudinal, perpendicular to the long axis of the AB-IGHL – transverse) conditions were used; again, allowing for the characterization of both isotropic and transversely isotropic materials.

Tensile elongations were applied to the tissue samples in the vertical direction, corresponding to the axis of motion of the materials testing system, while the clamp reaction force was measured by a load cell that was mounted to the bottom clamp. (Figure 4.1A) While the tissue was elongated, markers on the surface of the tissue were tracked using the motion tracking system developed in Section 3.0, allowing for the calculation of the Green-Lagrange principal strain of the tissue samples.

The clamp setup for shear elongations was more complex, and had two load cells. (Figure 4.1B) A load cell was mounted in the horizontal direction (perpendicular to applied elongations) to allow for the application of a horizontal pre-load. Once the pre-load was established, this load cell was not used for experimentation. Instead, the load cell mounted vertically (same load cell used for tensile elongations) was used to record the clamp reaction

force during experimentation. Again, elongations were applied in the vertical direction, which corresponded to the axis of motion of the materials testing system.

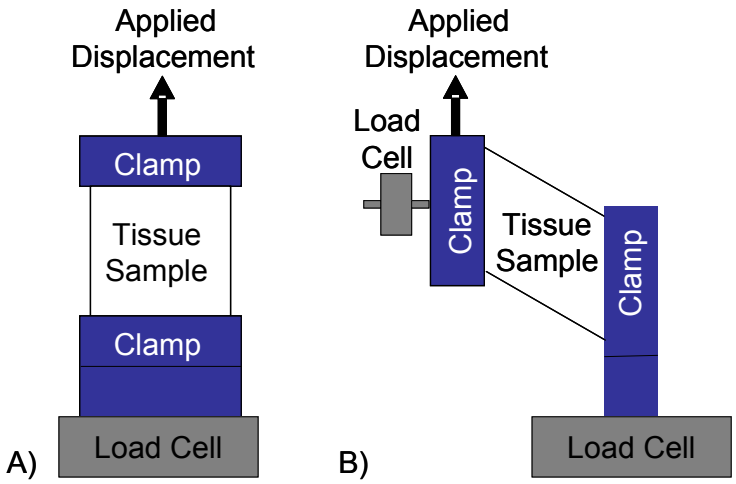

Figure 4.1: Tensile (A) and finite simple shear (B) clamp setups

The tissue sample geometry from each experimental loading condition was then used to create finite element meshes. These meshes, along with the applied elongation, were input into an inverse finite element routine generating a simulated load-elongation curve. This simulated load-elongation curve was then compared to the experimental load-elongation curve using an objective function, and the coefficients of the constitutive model were iteratively improved until the objective function was minimized, generating optimized coefficients. (Figure 4.2)

To assess the appropriateness of the isotropic constitutive model, optimized coefficients from one loading direction (longitudinal) were compared to optimized coefficients from the other loading direction (transverse), for both shear and tensile loading conditions. In addition, to assess the difference in the mechanical properties between the axillary pouch and posterior region of the capsule, the optimized coefficients from each loading condition were directly

compared to the same loading condition of the opposite region (i.e. tensile longitudinal of the axillary pouch was compared to tensile longitudinal of the posterior region).

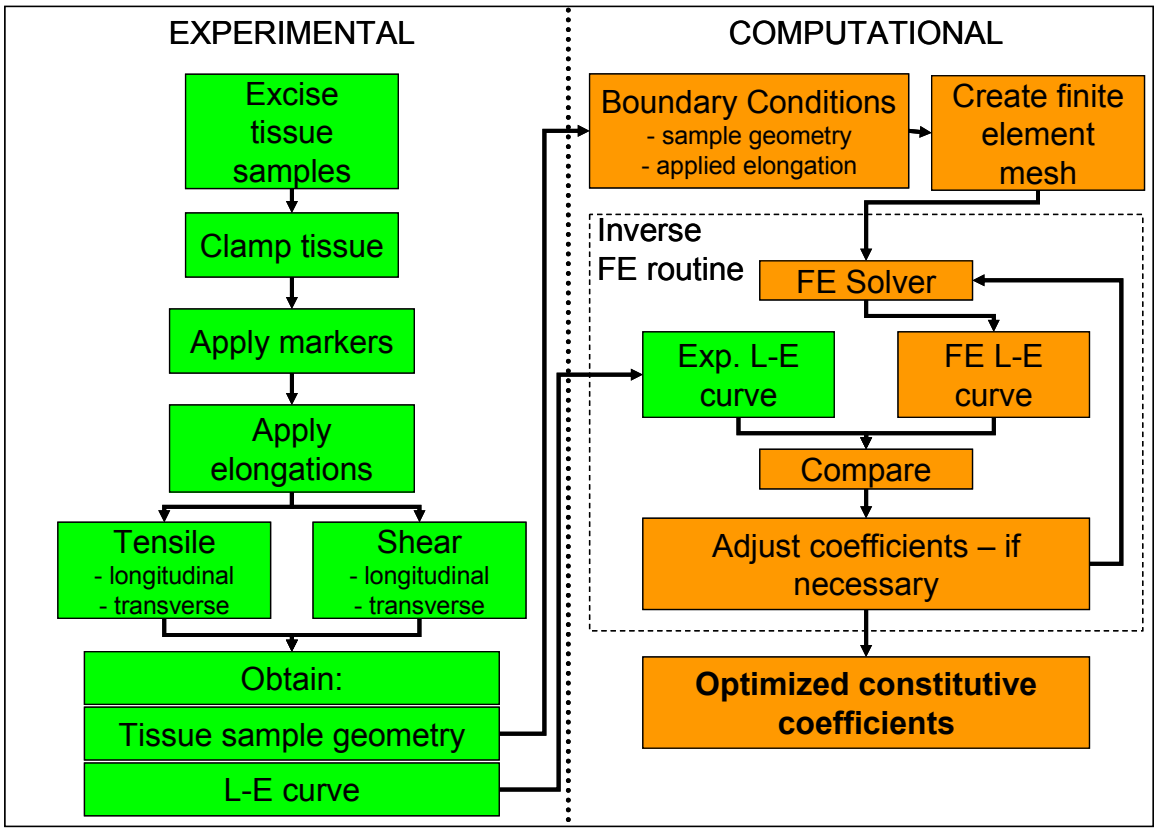

Figure 4.2: Flow-chart of combined experimental-computational methodology

4.2 MECHANICAL TESTING PROTOCOLS

Prior to the use of the methodology described by Weiss, *et al*, [69] a series of preliminary studies were performed to determine the appropriate conditions for the glenohumeral capsule, including both experimental and computational parameters. The following sections will provide a detailed explanation of the methodology, including all preliminary studies that have been performed.

4.2.1 Tissue Sample Procurement

Tissue samples were obtained from the axillary pouch and posterior regions of the glenohumeral capsule of fresh-frozen cadaveric shoulders. The superior margin of the AB-IGHL is an easily identifiable landmark in most capsules and has been highly characterized. [1, 17] In addition, it is often used as a consistent reference clinically and experimentally. Therefore, the superior margin of the AB-IHGL was chosen as a reference for the transverse (perpendicular to the longitudinal axis of the AB-IGHL) and longitudinal (parallel to the longitudinal axis of the AB-IGHL) loading directions during mechanical testing.

The two regions of interest (axillary pouch and posterior capsule) were defined by the borders of two common landmarks in the glenohumeral capsule, the anterior and posterior bands of the inferior glenohumeral ligament. (Figure 4.3) To locate these landmarks, the joint was abducted, distracted, and internally rotated (posterior band) or externally rotated (anterior band). Once the borders of each band were identified, incisions along each border were created. The posterior capsule was then identified by the region above the posterior band of the inferior glenohumeral ligament and below the insertion site of the infraspinatus muscle. The axillary pouch was identified as the region located between the anterior and posterior bands of the inferior glenohumeral ligament. After identification of each region, they were excised from the joint by removing their attachments into the labrum and humerus. Once removed from the joint, each tissue sample was cut again, creating a 25mm x 25mm square sheet of tissue. The tissue was then placed in a set of custom clamps with complimentary grooved surfaces that have been used to test soft tissues in the past [69], and a grid of nine (3 x 3) black delrin beads was placed on the surface of the capsule using cyanoacrylate.

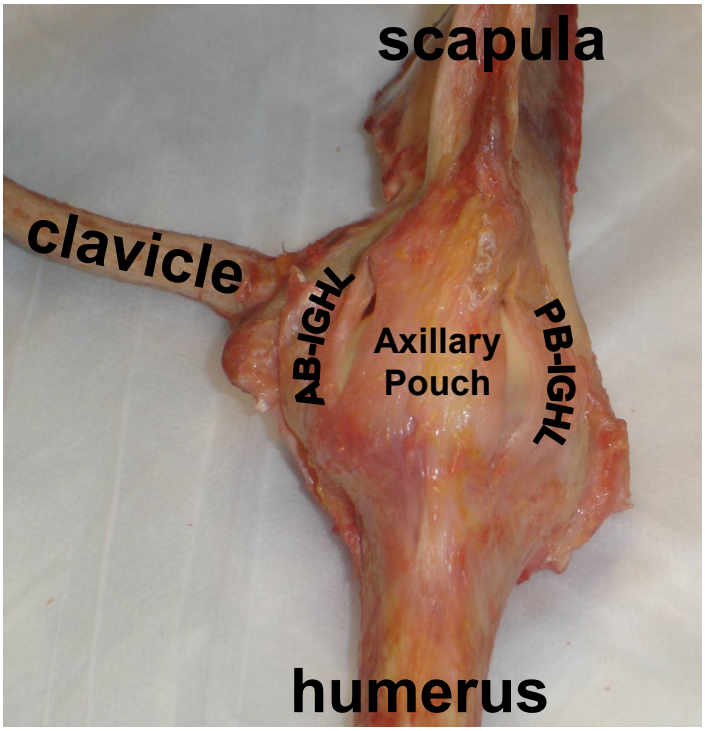

Figure 4.3: Identification of capsular regions

4.2.1.1 Observations of capsular structure

Several observations during dissection of specimens are worth noting. The posterior capsule was typically the thinnest region of the capsule, with thicknesses ranging from 0.5mm to 1.5 mm. In addition, specimens with larger muscle mass typically had thinner posterior capsules; sometimes even transparent. The axillary pouch was typically the thickest of the regions, with thicknesses ranging from 1 mm to 4 mm. The axillary pouch also had noticeable layers through the thickness of the tissue. Because of these layers it was difficult to obtain a clean incision, as shifting of the layers was common. In addition to difficulties with cutting the tissue, there were also difficulties with clamping the axillary pouch. In capsules with thicker axillary pouches, it was not uncommon for the layers to shift over one another when tightening the clamps on the tissue. (Figure 4.4)

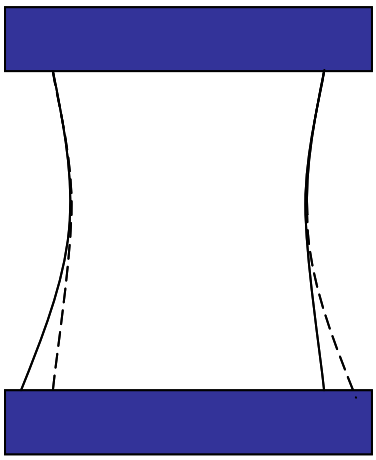

Figure 4.4: Schematic of axillary pouch layers shifting during clamping (solid lines – top layer, dashed lines – bottom layer)

4.2.2 Experimental protocol

Tissue samples from the glenohumeral capsule of ten cadaveric shoulders (51 ± 8 years) were obtained to characterize the mechanical properties of the tissue. The superior margin of the AB-IGHL was utilized as a reference for the transverse (perpendicular to the longitudinal axis of the AB-IGHL) and longitudinal (parallel to the longitudinal axis of the AB-IGHL) loading directions during mechanical testing.

A total of four non-destructive loading conditions were used in this protocol: 1) tensile elongations applied in the direction parallel to the longitudinal axes of the AB-IGHL – tensile longitudinal; 2) shear elongations applied in the direction perpendicular to the longitudinal axes of the AB-IGHL – shear transverse; 3) tensile elongations applied in the direction perpendicular to the longitudinal axes of the AB-IGHL – tensile transverse; and 4) shear elongations applied in the direction parallel to the longitudinal axes of the AB-IGHL – shear longitudinal. Thus, for

each specimen, a total of eight loading conditions were performed: axillary pouch tensile longitudinal (APTL), axillary pouch tensile transverse (APTT), axillary pouch shear longitudinal (APSL), axillary pouch shear transverse (APST), posterior tensile longitudinal (PTL), posterior tensile transverse (PTT), posterior shear longitudinal (PSL) and posterior shear transverse (PST). The order in which each tissue sample was tested was randomized. (Figure 4.5) Based on the design of the clamp setup, it was possible to perform a tensile test in the longitudinal direction and a shear test in the transverse direction (Option A) without the transaction of any material. Another option was to perform a tensile test in the transverse direction followed by a shear test in the longitudinal direction (Option B). Once either option was performed, however, it was required that the tissue that was previously clamped be transected. It is important to note that the tissue samples were continuously hydrated using a saline spray throughout the duration of this protocol.

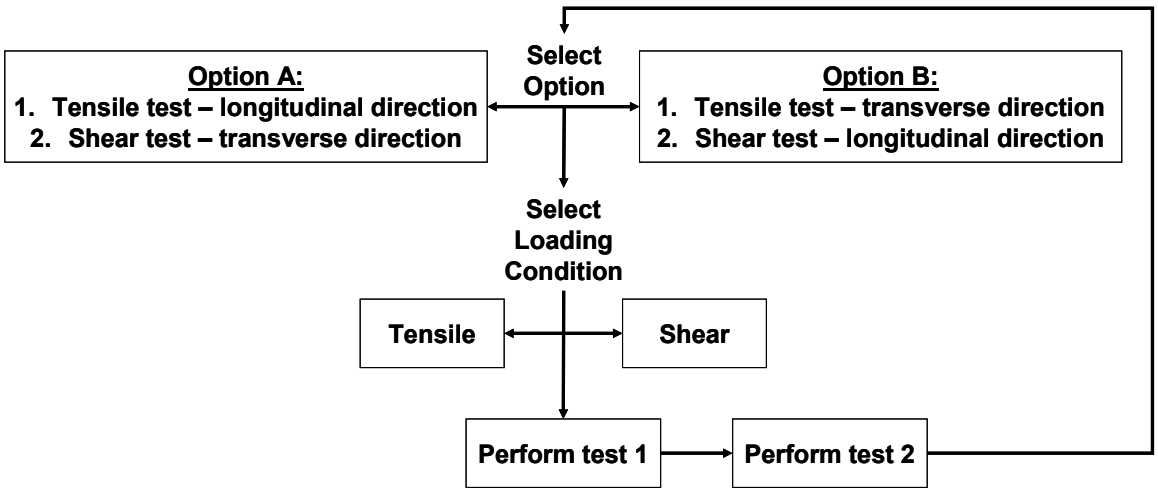

Figure 4.5: Randomization of experimental testing order

For tensile tests of the tissue, pre-loads of 0.5 N were applied. The purpose of applying a pre-load to the tissue sample before loading is to remove slack from the system, while not deforming the tissue. In addition, it serves as a consistent starting point across all tissue samples being tested.

To determine the proper pre-load for each region, the tissue samples were clamped using a custom set of soft tissue clamps and a small load was applied while using visual inspection to determine when the slack in the system was removed. Once this was achieved, the tissue was loaded until failure. To verify the proper value for the pre-load the load-elongation curve was visually inspected. If the pre-load was too low, the load-elongation curve would remain zero while the elongation increased. (Figure 4.6A) If the pre-load was too high, the load-elongation curve would immediately become linear from the start of elongation. (Figure 4.6C) If the pre-load was appropriate, however, the load would slowly begin to rise as elongation is applied until a linear region is finally obtained. (Figure 4.6B)

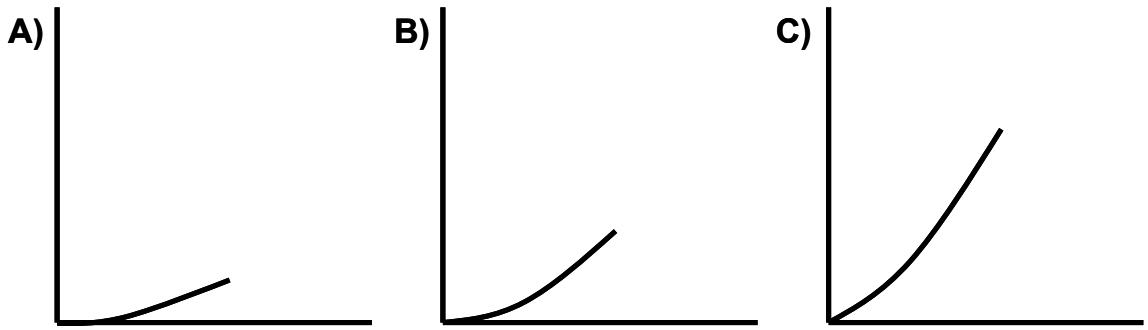

Figure 4.6: Load-elongation curves when too little (A), appropriate (B) and too large (C) of pre-loads are applied

This same methodology was used to determine the proper pre-loads for the shear loading configuration. As the tissue is elongated in the shear loading configuration, only the vertical degree of freedom (corresponding to the direction of the applied elongation) was free to translate. All other degrees of freedom (including the horizontal, or direction perpendicular to the applied elongation) were held rigid. Because the shear loading configuration has two load cells, two pre-loads were required. As in the case of the tensile loading configuration, the appropriate pre-loads were those which removed visible slack from the system yet did not deform the tissue, and achieved a load-elongation curve as shown in Figure 4.6B. Again, if either pre-load was too high, a load-elongation curve that is depicted in Figure 4.6A would have been observed and if either pre-load were too low, the load-elongation curve depicted in Figure 4.6C would have been observed.

The proper pre-load for the tensile loading conditions was chosen such that the criteria discussed above were met. For both the axillary pouch and posterior regions, the appropriate pre-load was determined to be 0.5 N. The appropriate pre-loads for the shear loading conditions were the same for both the axillary pouch and the posterior regions, and were 0.03 N in the horizontal direction (perpendicular to loading axis) and 0.1 N in the vertical direction (parallel to loading axis).

Once the tissue was pre-loaded, the initial width, length, and thickness of the tissue samples were determined as the average of three measurements obtained using digital calipers and a ruler. (Figure 4.7) The tissue sample was then preconditioned via 10 cycles of cyclic elongation between 0-1.5 mm at a rate of 10mm/min. Similar to the pre-load values, a preliminary experiment was performed to determine the proper number of cycles of preconditioning as well as preconditioning elongations.

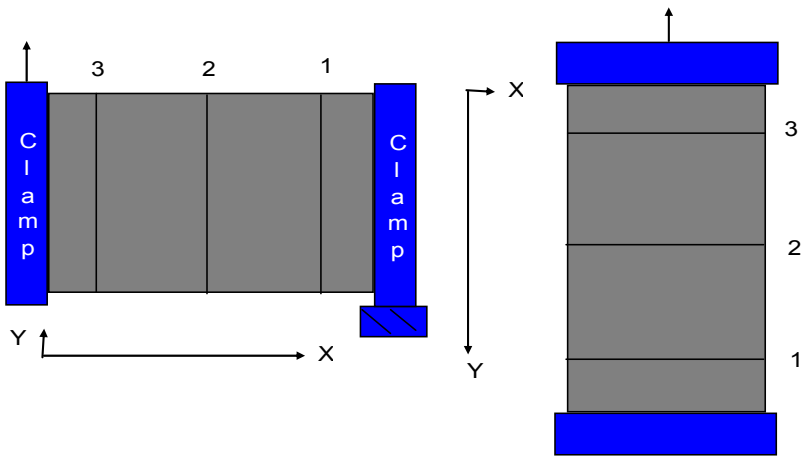

Figure 4.7: Locations of tissue sample measurements

To determine the appropriate preconditioning values for both tensile and shear loading conditions, the ultimate load-elongation curves obtained above were again utilized. In both cases the appropriate preconditioning elongation would load the tissue into the upper portion of the toe region, allowing the tissue to settle in the clamps. This reduces the likelihood of slippage of the tissue during the final cycle of elongation. To determine the number of cycles required for appropriate preconditioning, the tissue was cyclically loaded until the difference in load-elongation curves between two consecutive loading cycles was minimized ($R^2 > 0.99$).

The proper preconditioning levels for the axillary pouch and posterior capsule were 1.5 mm for tensile loading conditions and 2 mm for shear loading conditions, because these levels elongate the tissue into the upper portion of the toe region of the load-elongation curve.

The proper number of cycles for preconditioning was determined to be 10 cycles for all loading conditions and both regions of the capsule. This was chosen based on the fact that the ninth and tenth loading curves were nearly identical ($R^2 = 1$), as shown in a representative

loading condition in Figure 4.8, as well as the hysteresis between the loading and unloading phases of the curves being minimized.

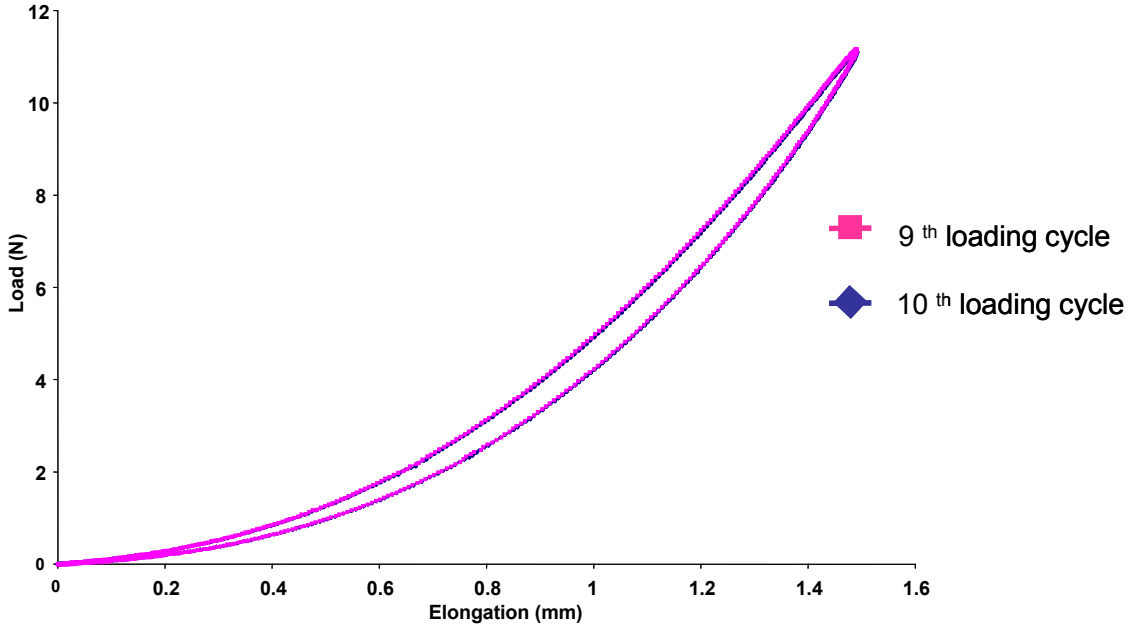

Figure 4.8: Loading and unloading phase of the ninth and tenth cycle of preconditioning

Directly following the preconditioning, a displacement of 2.25 mm was applied at a rate of 10mm/min, corresponding to ~20% of the average failure load of the tissue. Again, a preliminary experiment was performed to determine this value.

Since non-destructive elongations are being used in this protocol, it was imperative to verify the elongations that were being applied were not damaging the tissue samples. To do this, the ultimate load-elongation curves were obtained. A tissue sample was clamped, pre-loaded,

and finally elongated until failure at a rate of 10 mm/min, while the clamp reaction force and cross-head displacement was recorded.

The axillary pouch and posterior capsule behaved similarly during tensile load to failure tests, and therefore the same elongations of 2.25 mm were chosen for these two regions, which elongates the tissue well into the linear region yet far from the yield point of the tissue(indicated by repeatable curves following the application of this elongation). The axillary pouch and posterior capsule behaved similarly during shear loading as well, and thus an elongation corresponding to a shear $\kappa=\tan(\theta)$ of 0.4, where θ is the angle between the top edge of the tissue sample and the x-axis (Figure 4.9), was chosen for both of these regions, as it could consistently be applied to the tissue without causing damage (indicated by repeatable curves following the application of this elongation). [69]

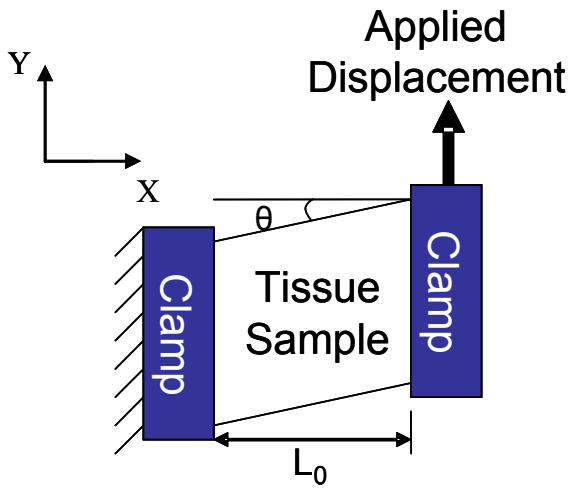

Figure 4.9: Shear angle θ

The clamp reaction force was determined and used along with the known applied elongation to estimate the coefficients of the constitutive model. The tissue samples were then allowed to recover for a 30 minute period. This length of time was chosen based on a preliminary experiment.

Due to viscoelastic properties, soft tissues exhibit a strain history whereby a tissue that is loaded and is then immediately reloaded using the same loading condition will exhibit a different response. Therefore, a time of recovery between loading conditions is necessary to ensure all effects of strain history are minimal. Since multiple loads are being applied to each tissue sample in the current protocol, it is necessary to allow the tissue samples to recover to their undeformed state. Little has been reported about the recovery period of large sheets of the glenohumeral capsule, as being used in this protocol. Therefore it was necessary to determine the appropriate recovery time that allowed the tissue to fully recover to its original state.

Thus, a non-destructive elongation was applied to each tissue sample and the tissue sample was allowed to recover for varying times. Based on reported times in literature, 15 minutes, 30 minutes, and 45 minutes were used to test recovery times. [67] Following these recovery times, the tissue was loaded in the exact same manner and the loading curves were compared. An appropriate recovery time was one in which those loading curves matched with an R^2 value of at least 0.95 and required the least amount of time.

The recovery time for a sheet of the axillary pouch and posterior regions of the glenohumeral capsule was determined to be 30 minutes. Thirty minutes was chosen based on how well it reproduced the original loading curve ($R^2 = 1$), as well as being the shortest amount of time necessary to reproduce that loading curve. A representative loading curve showing the

reference, or initial loading curve and the load-elongation curve following a 15, 30, and 45 minute recovery period is depicted in Figure 4.10.

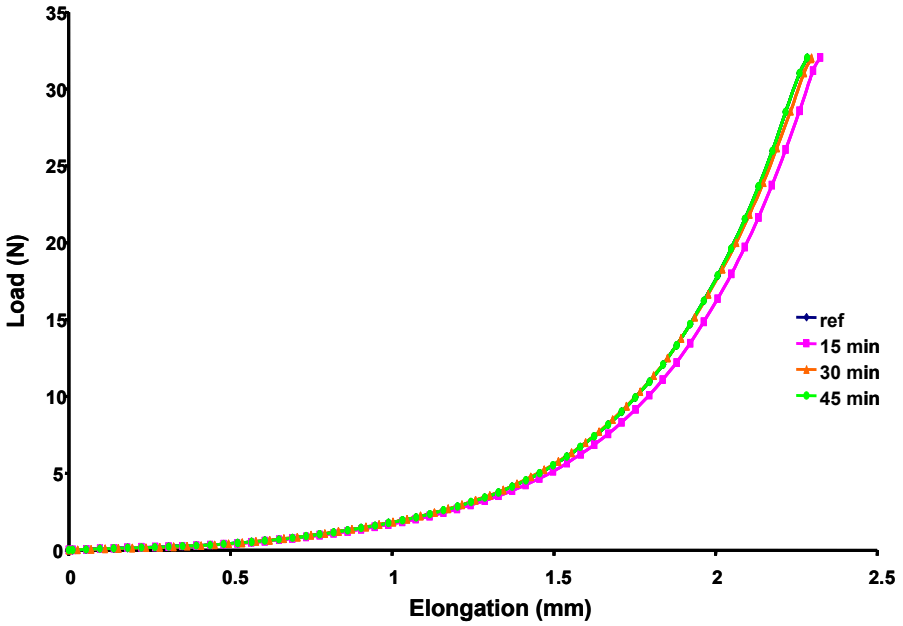

Figure 4.10: Load-elongation graph of initial cycle and following different recovery periods

Following the recovery period, the tissue sample was removed from one clamp and reclamped using a custom shear clamp, corresponding to the opposite direction; i.e. if the tensile elongation was applied in the longitudinal direction, the following shear elongation was applied in the transverse direction. A preliminary experiment was performed to ensure the reclamping of the tissue did not alter the response of the tissue.

A tissue sample was tested in tension by applying a 2.25 mm elongation and was then allowed to recover for 30 minutes. Following complete recovery, the tissue sample was removed from the clamps completely, and then inserted back into the clamps being sure the grooves of the

clamps aligned with the grooves on the tissue. The clamps and tissue sample were then re-positioned within the testing setup and the experimental protocol was repeated. The load-elongation curves from each of these tests were then compared.

The results showed that removing the tissue from the clamps and then reclamping it has no effect on the load-elongation curve of the ensuing test. As shown in Figure 4.11, the two curves had a correlation coefficient of 1, meaning they were nearly identical.

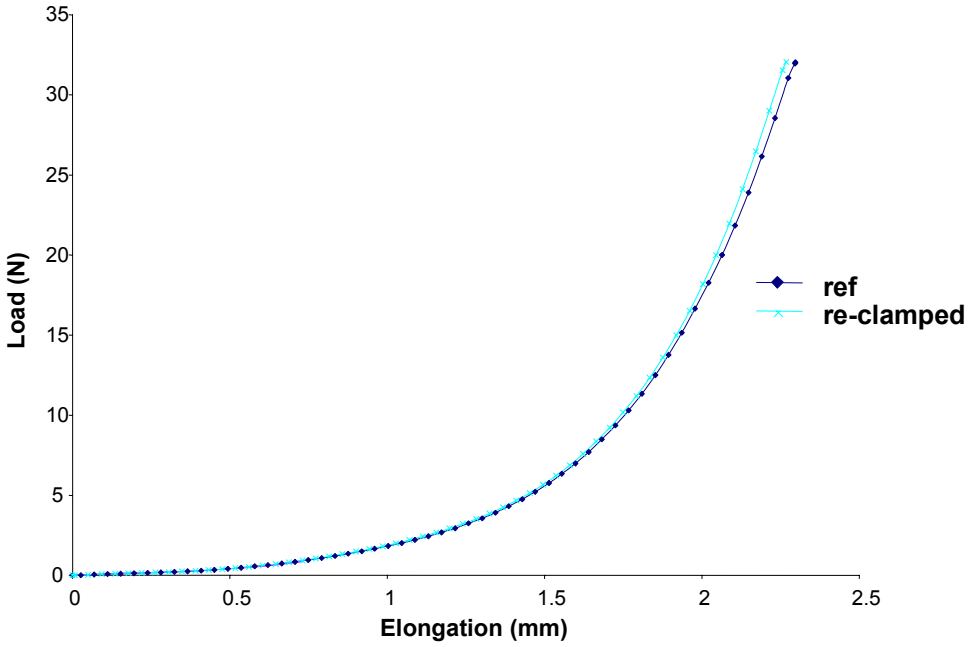

Figure 4.11: Effects of reclamping on ensuing load-elongation curves

Once reclamped, the tissue sample was repositioned in the materials testing system and pre-loads of 0.03N and 0.1N were applied in the perpendicular and parallel directions (with respect to the axis of loading), respectively. Following the application of pre-loads, the initial

width, length, and thickness of the tissue samples were determined as the average of three measurements obtained using digital calipers and a ruler. Each tissue sample was then preconditioned by cyclically applying a displacement of 0-2mm (x10). Immediately following preconditioning, the pre-loads were reestablished and a displacement corresponding to a shear $\kappa=\tan(\theta)$ of 0.4 (Figure 4.9) was applied at a shear strain rate of 10mm/min based on the measured width of each specimen. This displacement was chosen based on previous work that has been performed on the MCL [69] as well as it loaded the tissue into the linear region of the load-elongation curve but did not damage the tissue, indicated by reproducible load-elongation curves when this displacement was applied. The clamp reaction force was measured using the load cell parallel to loading (Sensotec, Columbus, OH: range 0-223N, accuracy 0.1 N, resolution 0.05 N). Following cyclic testing, the tissue samples were again allowed to recover for 30 minutes.

The tissue sample was then released from the custom clamps and the tissue that was previously held within the clamps was excised from the tissue sample via careful scalpel transection. The opposite edges of the tissue sample were wrapped in gauze, soaked in saline, and placed in the custom clamps. The tensile and shear tests were then reproduced for the perpendicular loading conditions of the tissue sample. It should be noted that the order in which the loading configurations are applied to the tissue samples was randomized.

4.2.2.1 Issues with clamp movement

During preliminary testing it was noted that for the shear clamp setup undesired motions of the clamps were occurring. The clamps were originally designed to apply shear loads to the medial collateral ligament along the length of the ligament (thus along length of collagen fibers), however, because the glenohumeral capsule has a collagen fiber architecture such that fibers run

in all directions, the forces being exerted on the clamps were much greater. Both the horizontal and vertical clamps had a moment being applied to them, causing them to rotate. (Figure 4.12)

This violated the assumptions that were made during the computational simulations of each experiment. For each simulation, it was assumed that a finite simple shear elongation was being applied to the tissue sample, meaning the clamps were only translating in the vertical direction (parallel to direction of applied elongation) and that all other displacements were fixed. In addition, because the clamps were not moving consistently between tissue samples, the same elongations were not being applied to different tissue samples.

To alleviate this problem, a redesign of the clamps was necessary. The redesign had to account for the larger loads that were being applied to the clamps and minimize displacements and rotations in all directions other than the direction corresponding to the applied elongation.

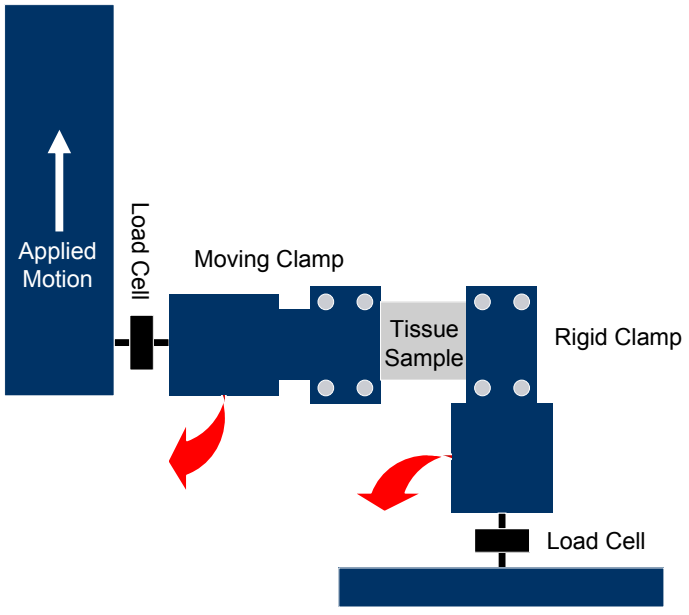

Figure 4.12: Original shear clamp setup showing clamp rotations

Clamp movement as large as 3 mm was noticed during shear loading of the axillary pouch and posterior capsule. The new clamp setup (Figure 4.13) included a brace that was positioned below the horizontal load cell, and allowed for free motion when no vertical load was applied allowing for a horizontal pre-load to be applied. Once a vertical load was applied, however, the motion of the horizontal load cell was restricted by the brace. In addition to the brace, a new pancake style load cell was used, replacing the original load cell which had two small posts on either side. This new load cell allowed the clamps to be securely tightened, preventing any kind of rocking motion during loading. With this new clamp setup, clamp motions were reduced to less than 0.1 mm for all shear loading conditions.

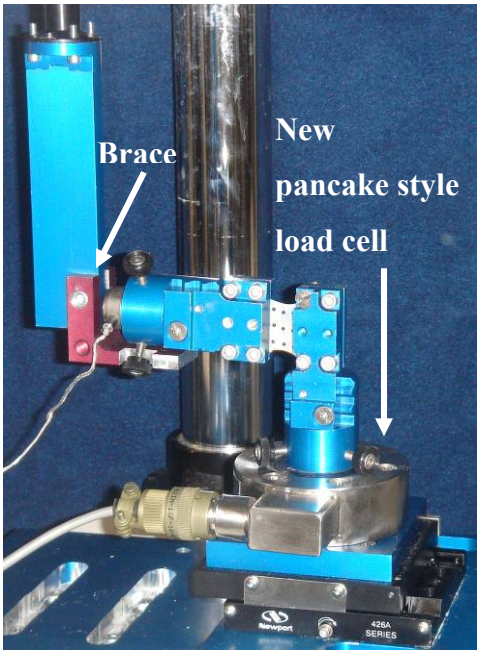

Figure 4.13: New clamp setup

4.2.2.2 Data obtained / analysis

The clamp reaction force obtained from the vertical load cell was used along with the known applied displacement to generate load-elongations curves for each loading condition. These load-elongation curves were then used in the inverse finite element routine to generate the optimized constitutive coefficients. In addition, tissue sample dimensions (width, thickness, height) were obtained for all loading conditions applied to each tissue sample and were used to generate the finite element meshes for the inverse finite element routine. Finally, the displacements of the markers on the surface of the tissue were used in conjunction with a finite element solver (ABAQUS v6.4.2, Providence, RI) to calculate the Green-Lagrange maximum principal strain (tensile loading conditions) or the Green-Lagrange maximum shear strain (shear loading conditions), where the position of the markers at time step zero were used as the strain free configuration, and the position of the markers at the final time step were used as the strained configuration.

4.2.3 Computational protocol

The clamp reaction forces, tissue elongations, and tissue sample dimensions from each experimental loading condition were used as boundary conditions to determine optimal constitutive coefficients for the hyperelastic isotropic strain energy (Equation 4.1) via an inverse finite element optimization technique [67]. (Figure 4.14)

$$W = C_1(e^{C_2(\tilde{I}_1-3)} - 1) - \frac{C_1 C_2}{2}(\tilde{I}_2 - 3) + U(J) \qquad \textbf{(4.1)}$$

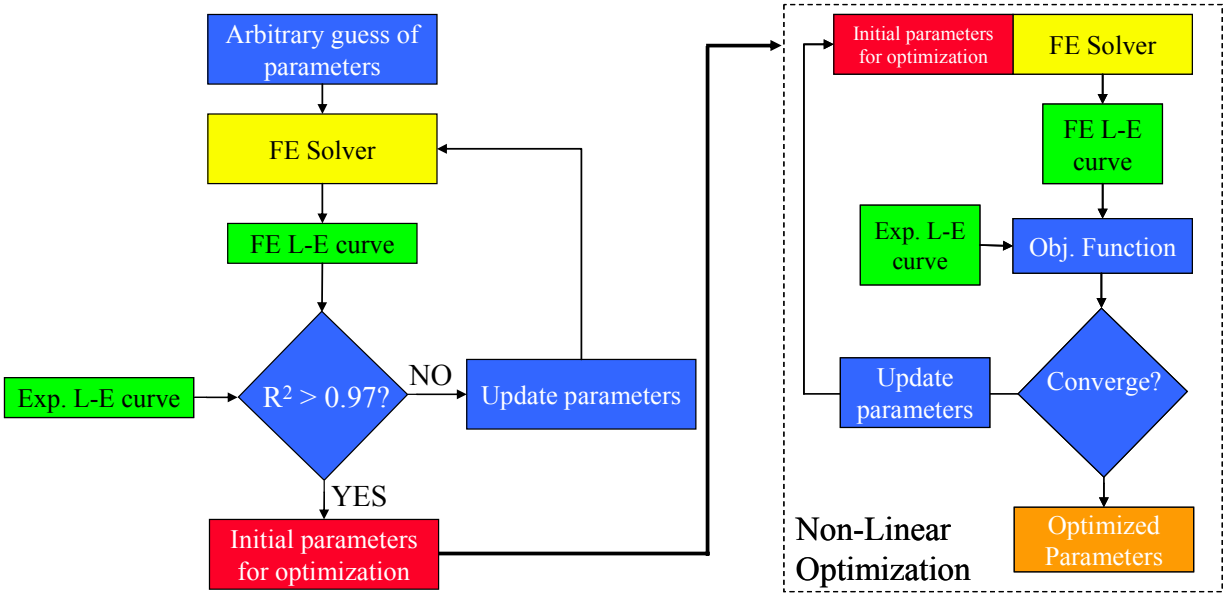

Figure 4.14: Flowchart of computational material parameter optimization technique

The hyperelastic strain energy that was used in this protocol (Equation 4.1)[72] uncoupled the dilatational and deviatoric behavior of the tissue. An uncoupled deviatoric/dilatational constitutive formulation has numerical advantages for simulating nearly incompressible material behavior with the FE method [72], and the formulation is identical to the fully coupled strain energy in the limit of incompressibility or for an isochoric deformation (J = 1 for both cases). [67] This function represents the tissue matrix strain energy, where I_1 and I_2 are the deviatoric invariants of the right deformation tensor. U(J) governs the dilatational response of the tissue, where J is the volume ration and K represents effective bulk modulus of the material. Finally, C_1 and C_2 are the constitutive coefficients that will be determined using the inverse finite element optimization routine, where C_1 scales the magnitude of the stress-strain curve and C_2 governs the magnitude and linearity of the stress-strain curve. This particular form of the strain energy was originally developed be Veronda and Westmann [73] to model feline skin and then later expanded by Weiss, *et. al* [67] to model the human MCL. Further, this strain

energy is convex and exhibits physically reasonable behavior under tension, compression, and shear.

An image from each loading condition was used to create a finite element mesh by adjusting integration points of the mesh until they were aligned with the edges of the tissue samples. (Figure 4.15) That mesh was then assigned material properties according to the hyperelastic isotropic constitutive model [72], creating a finite element model. This method of mesh development was chosen based on preliminary experiments.

Originally, finite element meshes were created using a custom program wrote by Steve Maas, a member of Dr. Jeffrey Weiss' laboratory in Utah. This program allowed for the input of the geometry of each tissue sample, specifically three sample thicknesses taken across the length of the tissue sample (tensile) or width of the sample (shear), and then generated a finite element mesh. In addition, the corners of each tissue sample were obtained from the camera system and input into the meshing program. Because of the phenomenon in which the tissue squeezes from the clamps as they are tightened, however, the exact geometry of the tissue samples was not being accurately defined. Therefore, another program was developed by Mr. Maas which allowed for the implementation of the exact sample widths across the entire tissue sample. An image of each tissue sample was input into the software, and integration points of the mesh were allowed to be manually manipulated to match the geometry of the tissue sample. (Figure 4.15)

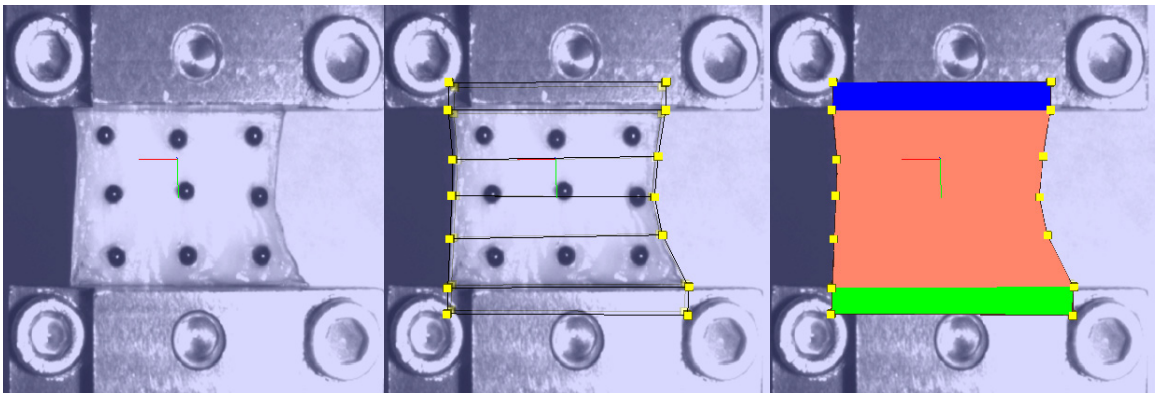

Figure 4.15: Mesh generation accounting for tissue sample geometry

Using the initial meshing program, a total of three cases were unable to converge to a solution during the finite element simulations. The new program, however, better represented the tissue sample geometry, allowing those cases to reach a solution. In addition, because the optimized constitutive coefficients were significantly different between the two meshing programs, the new program, which more accurately represented the tissue sample geometry, was used for all optimizations. With the appropriate geometry of the mesh defined, the next decision was to define the density of the mesh. Since few studies using a combined experimental and computational approach with the glenohumeral capsule have been performed, it was important to perform a parametric analysis of the mesh density of the finite element meshes.

A mesh with too few elements would average most of the tissue response over large areas, and therefore reduce the reliability of the obtained coefficients. A large number of elements would increase the accuracy of the obtained coefficients; however, this would also increase the computational time drastically. An appropriate mesh density would be one that accurately describes the tissue response without an excessive number of elements.

A total of five mesh densities were used in this parametric analysis: 6, 600, 1200, 1944, and 2400 elements, and were applied to four random loading conditions of one specimen (two tensile, two shear). These numbers were chosen based on the method of creating the mesh described previously. As depicted in Figure 4.15, five integration points exist along each edge of the tissue sample. The program allows the user to input a certain number of elements between each set of integration points in the X, Y, and Z directions. A consistent number (four) of elements was used for the Z direction (thickness), based on previous work [67] that modeled the MCL.

The differences in the optimized constitutive coefficients were found between mesh densities of 600, 1200, and 1944 elements. In both cases of shear loading for the 2400 element mesh density, the finite element simulations encountered inverting elements, and therefore tensile loading conditions were not optimized since it was obvious that this density would not be sufficient for the capsule. In addition, one shear loading condition also had inverting elements with the 1944 element mesh density. The optimized constitutive coefficients for each density and loading condition are shown in Table 4.1.

Since there was no difference between the optimized coefficients for the 600, 1200, and 1944 mesh densities, it was determined that the optimal mesh density was 1200 elements. This allowed the mesh density to be adjusted by increasing or decreasing in cases where finite element simulations encountered errors. It should be noted that only shear loading conditions caused errors during finite element simulation, thus only meshes of shear loading conditions would require an increase or decrease in mesh density to complete a full optimization.

Table 4.1: Optimized coefficients with differing mesh densities

	APSL		APTT		PST		PTL	
Elements in mesh	C_1	C_2	C_1	C_2	C_1	C_2	C_1	C_2
6	0.078	9.815	0.422	7.855	0.130	6.566	0.189	8.001
600	0.069	10.589	0.322	11.153	0.118	6.479	0.125	12.445
1200	0.069	10.677	0.320	11.243	0.112	6.590	0.125	12.512
1944	0.069	10.724	0.316	11.341	NA	NA	0.100	12.690

APSL – axillary pouch shear longitudinal
APTT – axillary pouch tensile transverse
PST – posterior shear transverse
PTL – posterior tensile longitudinal

After creating the finite element mesh, it was necessary to define the material properties of the tissue sample. A starting value of 0.1MPa and 10 for C_1 and C_2, respectively, was consistently used as an initial guess for the model. These values were then updated by running the finite element models and comparing the simulated load-elongation curves to the experimental curves until the correlation coefficient between them was at least 0.97. These coefficients were then used to create an input file for the inverse finite element model optimization routine.

The inverse finite element optimization routine iteratively improved the values of C_1 and C_2 using a sequential quadratic programming method in the NAG Fortran77 Library routine E04UNF (Numerical Algorithms Group, Oxford, England). The NAG routine minimized a smooth objective function (Equation 4.2) subject to a set of constraints on the variables (in this case, the constraint is that both constitutive coefficients are greater than 0 but less than 5 MPa (C_1) or 50 (C_2) to ensure physically reasonable behavior and strong ellipticity) [74].

$$F(x) = \frac{1}{2}\sum_{i=1}^{m}\{y_i - f_i(x)\}^2 \quad \textbf{(4.2)}$$

Here, F(x) is the objective function that is to be minimized, where y is the experimental forces, f(x) is the computational simulated forces, *i* represents a particular clamp displacement level and *m* is the number of discrete clamp displacement levels (11 for this optimization routine, based on previous work performed on the MCL [69]). This function essentially solves the non-linear least squares problem. The output of the overall parameter estimation procedure was the optimal set of constitutive coefficients (C_1 and C_2) that minimized the objective function when comparing the experimental and simulated forces.

4.2.3.1 Uniqueness of optimized coefficients

The uniqueness of these coefficients was evaluated using several methods. First, the initial guess for the coefficients of the MCL was altered, and the effect on the corresponding optimized coefficients was determined. Using three different initial guesses for C1 and C2, the optimization routine was capable of calculating the optimized coefficients within a standard deviation of 24.7 Pa and 0.09 for C_1 and C_2, respectively. [69] Although the deviation for C_1 appears to be large, it is important to note that the typical optimized values for C_1 were two orders of magnitude greater than this value.

The same method was performed by Mr. Maas for the glenohumeral capsule; however two loading conditions were evaluated: tensile longitudinal and shear transverse. For the first loading condition, five values of C_1 and C_2 were examined and ranged from 0.03 to 0.08 MPa and 10 to 40, respectively. (Table 4.2) The optimized coefficients from all five cases were identical. For the second loading condition, five values of C1 and C2 were used again; however

they ranged from 0.02 to 0.5 MPa and 2 to 10, respectively. (Table 4.3) The optimized coefficients for all five cases were once again identical.

Table 4.2: Effects of initial guess on optimized coefficients (tensile longitudinal)

Initial guess		optimized	
C_1	C_2	C_1	C_2
0.05	20	0.05	20.0
0.03	40	0.05	20.0
0.08	40	0.05	20.0
0.03	10	0.05	20.0
0.08	10	0.05	20.0

Table 4.3: Effects of initial guess on optimized coefficients (shear transverse)

Initial guess		optimized	
C_1	C_2	C_1	C_2
0.1	5	0.10	5.0
0.02	10	0.10	5.0
0.5	10	0.10	5.0
0.02	2	0.10	5.0
0.5	2	0.10	5.0

Finally, the uniqueness of the optimized coefficients was evaluated by defining C_1 and C_2 for a random tissue sample, for tensile transverse and shear longitudinal loading conditions. Specifically, C_1 and C_2 were defined to be 0.1 MPa and 10 for both loading conditions. These values were then used to generate a finite element simulated load-elongation curve, based on the geometry of that specific tissue sample. Those load-elongation values were then input into the inverse finite element optimization routine as the experimental values, and the optimization routine was started. Ideally, if the optimized coefficients are unique, they would be the same as the coefficients that were originally defined. In addition, because it was assumed that the tissue

was isotropic, it was expected that the optimized coefficients for tensile and shear loading conditions would be similar. The resulting optimized coefficients were identical to the initially defined coefficients for both loading conditions. In addition, the tensile and shear optimized coefficients were also identical, suggesting the tissue is isotropic. (Figure 4.16)

Tensile Transverse

initial declaration of coefficents	
C1	C2
0.1	10

FE predicted values	
displacement	force
0.000	0.000
0.600	1.233
1.200	2.576
1.800	4.133
2.400	5.999
3.000	8.331
3.600	11.253
4.200	14.944
4.800	19.632
5.400	25.610
6.000	33.258

optimized coefficents	
C1	C2
0.1000	9.9993

Shear Longitudinal

initial declaration of coefficents	
C1	C2
0.1	10

FE predicted values	
displacement	force
0.000	0.000
0.225	0.652
0.450	1.446
0.675	2.506
0.900	3.995
1.125	6.126
1.350	9.242
1.575	13.857
1.800	20.777
2.025	31.296
2.250	47.459

optimized coefficents	
C1	C2
0.0999	10.0030

Figure 4.16: Test of uniqueness of optimized coefficients

4.2.3.2 Sensitivity of simulated load-elongation curves to constitutive coefficients

In order to determine the significance of differing constitutive coefficients, it was necessary to determine the effect of changing the constitutive coefficients on the overall structural behavior of the entire tissue sample, thus the simulated load-elongation curves. Therefore, random sample geometry and boundary conditions were chosen and the constitutive coefficients were altered. For the first condition, the constitutive coefficient C1 was held constant while C2 was changed in

a range of 1 to 10, in increments of 1. The second condition, C2 was held constant while C1 was ranged from 0.1 to 1 MPa, in increments of 0.1 MPa. These values were chosen based on values reported for the optimized constitutive coefficients of the MCL. [69]

The effect of changing the constitutive parameter C_1 on the simulated load-elongation curve is shown in Figure 4.17. As shown, by increasing the value of C_1, the magnitude of the curve is increased and by decreasing the value of C_1, the magnitude of the curve is decreased. The effect of changing constitutive parameter C_2 on the simulated load-elongation curve is shown in Figure 4.18. As shown in this figure, C_2 affects the curve in two ways. First, by increasing and decreasing the value of C_2 the magnitude of the curve is increased and decreased, respectively. Secondly, by increasing and decreasing the value of C_2, the linearity of the curve is decreased and increased, respectively. It is important to note, however, that for the curves with a C_2 value of 8, 9, and 10, the curves have been cutoff in order to allow for comparison of the curves with lower magnitudes.

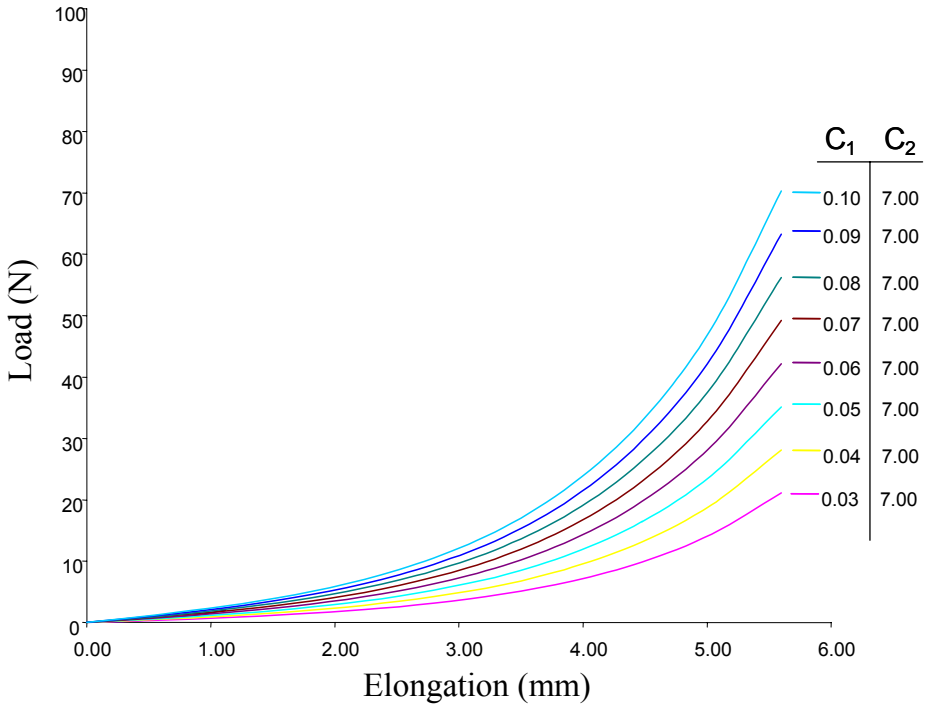

Figure 4.17: Effects of changing C1 on the simulated load-elongation curve

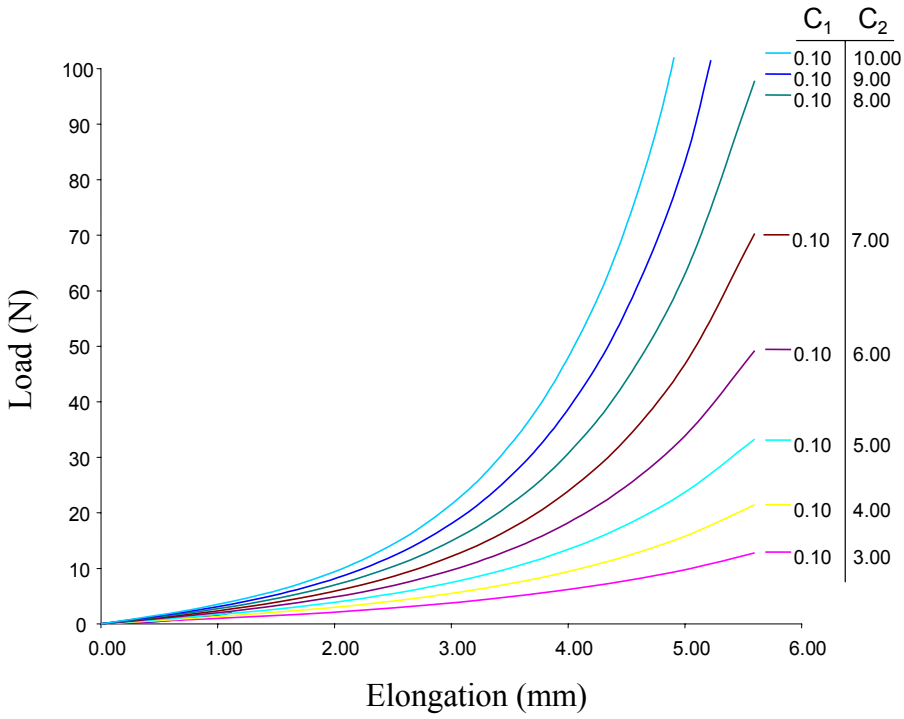

Figure 4.18: Effects of changing C2 on the simulated load-elongation curve

4.2.3.3 Sensitivity of stress-stretch curves to constitutive coefficients

Much like the importance of knowing the effect of the constitutive coefficients on the overall structural behavior of the tissue, it is also important to know the effect on the stress-stretch relationship of the material. Because of the differences in the deformation gradients for tensile (Equation 4.3) and simple shear loading (Equation 4.4); different relationships were developed, with the assumption of an isochoric deformation.

$$F = \begin{bmatrix} 1 & \lambda & 0 \\ 0 & 1 & 0 \\ 0 & 0 & 1 \end{bmatrix} \tag{4.3}$$

$$F = \begin{bmatrix} \lambda & 0 & 0 \\ 0 & \frac{1}{\sqrt{\lambda}} & 0 \\ 0 & 0 & \frac{1}{\sqrt{\lambda}} \end{bmatrix} \tag{4.4}$$

Next, the left Cauchy-Green deformation tensor (B) for tension (Equation 4.6) and shear (Equation 4.7) was calculated by multiplying the deformation gradient (F) by its transpose (F^T). (Equation 4.5)

$$B = F \cdot F^T \tag{4.5}$$

$$B = \begin{bmatrix} 1+\lambda^2 & \lambda & 0 \\ \lambda & 1 & 0 \\ 0 & 0 & 1 \end{bmatrix} \tag{4.6}$$

$$B = \begin{bmatrix} \lambda^2 & 0 & 0 \\ 0 & \frac{1}{\lambda} & 0 \\ 0 & 0 & \frac{1}{\lambda} \end{bmatrix} \tag{4.7}$$

The next step was to calculate the invariants I_1 and I_2 for both cases. The same equation was used to determine each invariant of shear and tensile deformations (Equation 4.8 – solving for I_1, Equation 4.9 – solving for I_2), where tr(B) represents the trace of B.

$$I_1 = tr(B) \tag{4.8}$$

$$I_2 = \frac{1}{2}\left[I_1^{\,2} - tr(B^2)\right] \tag{4.9}$$

$$I_1 = I_2 = 3 + \lambda^2 \tag{4.10}$$

$$I_1 = \frac{\lambda^3 + 2}{\lambda} \tag{4.11}$$

$$I_2 = \frac{2\lambda^3 + 1}{\lambda^2} \tag{4.12}$$

Finally, to determine the stress-stretch relationship for each case, the partial derivative of the strain energy function (Equation 4.1) was taken with respect to I_1 and I_2 to obtain W_1 and W_2, respectively. (Equations 4.13 and 4.14, respectively)

$$W_1 = C_1 C_2 e^{C_2(I_1-3)} \tag{4.13}$$

$$W_2 = -\frac{1}{2} C_1 C_2 \tag{4.14}$$

With these values known, the Cauchy stresses were calculated using Equation 4.15.

$$T = 2\left[\left(W_1 + I_1 W_2\right)\cdot B - W_2 B^2\right] \tag{4.15}$$

Finally, the stress-stretch relationships for simple finite shear (Equation 4.16) and pure tensile (Equation 4.17) deformations were determined.

$$T_{12} = \lambda_{12} C_1 C_2 (2e^{C_2 \lambda_{12}^{\ 2}} - 1) \tag{4.16}$$

$$T_{11} = \frac{C_1 C_2 (\lambda_{11} - 1)(\lambda_{11}^{\ 2} + \lambda_{11} + 1)(2\lambda_{11} e^{\frac{C_2(\lambda_{11}+2)(\lambda_{11}-1)^2}{\lambda_{11}}})}{\lambda_{11}^{\ 2}} \tag{4.17}$$

Because the constitutive coefficients govern the stress-stretch relationship of the tissue, stress-stretch curves are more representative of the mechanical properties of the tissue sample, rather than the structural response that is provided by the load-elongation curves. It is important to note, however, that these stress-stretch curves are not representative of what was induced in

the tissue sample during the experiment. Instead, they represent either pure tensile elongations, or pure simple finite shear elongations. Because the aspect ratio used in this work was so poor (~1:1), pure tension assumptions are valid.

For both tensile and shear loading conditions, the value of C_1 was ranged from 0.001 to 1 MPa while C_2 was held constant at three different levels: 8, 10, and 12. Again, for both tensile and shear loading conditions, the value of C_2 was ranged from 1 to 20 while the value of C_1 was held constant at 0.08, 0.10, and 0.12 MPa. Again, these ranges were chosen based on values that have been reported for the MCL. [69] A stretch value of 0.15 and 0.4 was used for tensile and shear loading conditions, respectively. These values were chosen as an estimate of the stretch values that were applied to the tissue samples experimentally.

The effect of changing the constitutive coefficients on the stress-stretch curve has a similar effect as changing constitutive coefficients on the load-elongation curve. Increasing the value of C_1 increases the magnitude of the stress-stretch curve for both tensile and shear loading, while decreasing the value of C_1 decreases the magnitude of the curve. The effect, though, is magnified as the value of C_2 is increased from 8 to 12. (Figures 4.19-4.24 ** Note different scales) Increasing the value of C_2 increases both the magnitude and the non-linearity of the stress-stretch curve for both tensile and shear loading, while decreasing the value of C_2 decreases the magnitude and non-linearity of the curve. Again, the effect is magnified as the value of C_1 was increased from 0.08 to 0.12 MPa. (Figures 4.25 – 4.30 ** Note different scales) For instance, a value of zero for C_2 would correspond to a perfectly linear stress-stretch curve. This information becomes useful when comparing the constitutive coefficients, in that a change in C_1 of less than 0.3 MPa and a change in C_2 of less than 3 will not drastically change the stress-stretch relationship. Therefore, when the coefficients of two different tissue samples differ by

less that 0.3 MPa for C_1 and 3 for C_2 the mechanical properties of those tissue samples can be considered similar.

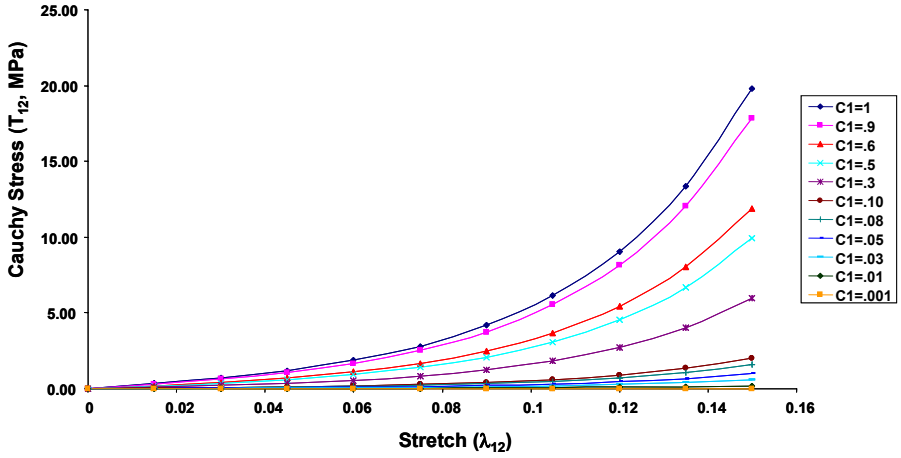

Figure 4.19: Effect of changing C1 on stress-stretch curve (C2 = 8)

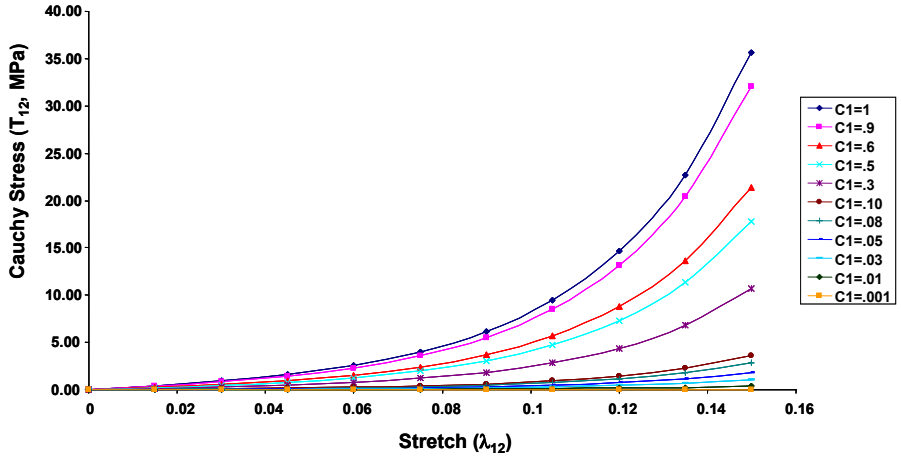

Figure 4.20: Effect of changing C1 on stress-stretch curve (C2 = 10)

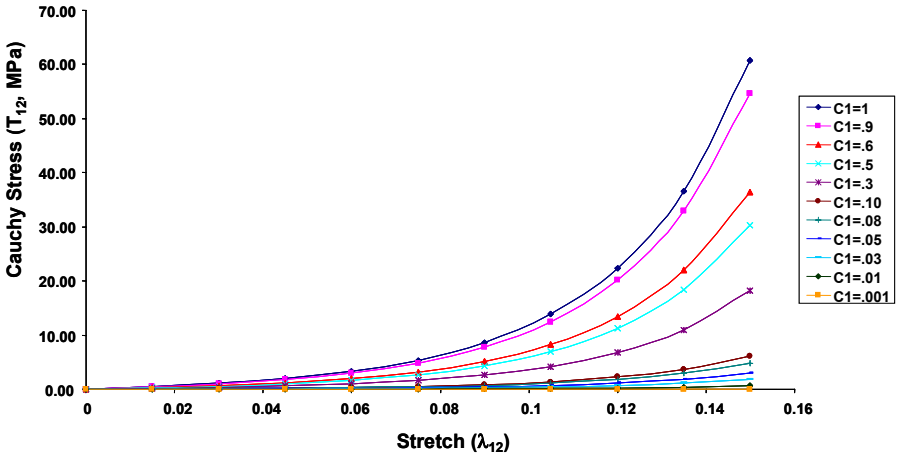

Figure 4.21: Effect of changing C1 on stress-stretch curve (C2 = 12)

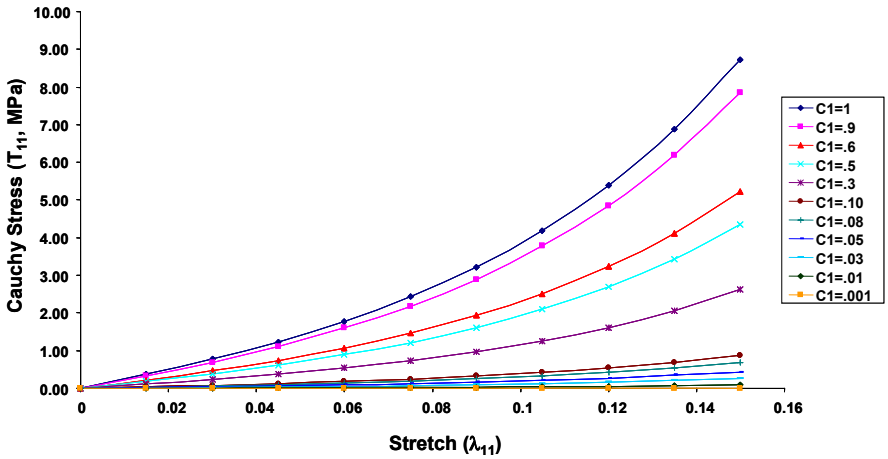

Figure 4.22: Effect of changing C1 on stress-stretch curve (C2 = 8)

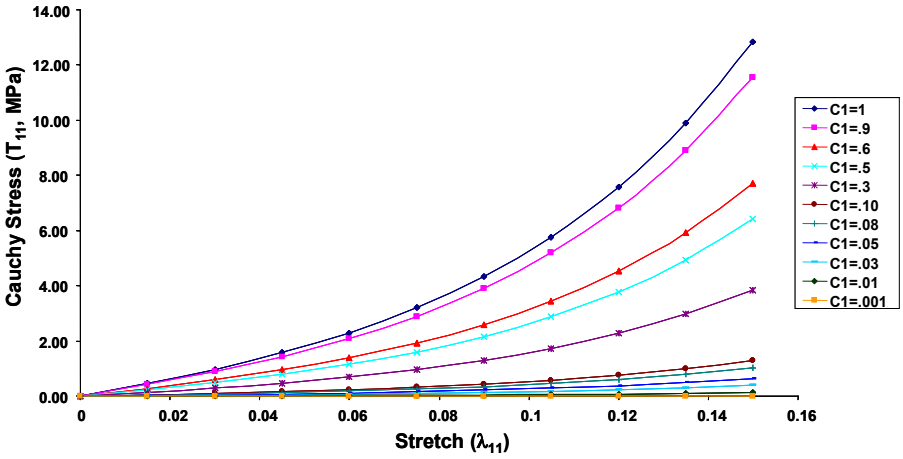

Figure 4.23: Effect of changing C1 on stress-stretch curve (C2 = 10)

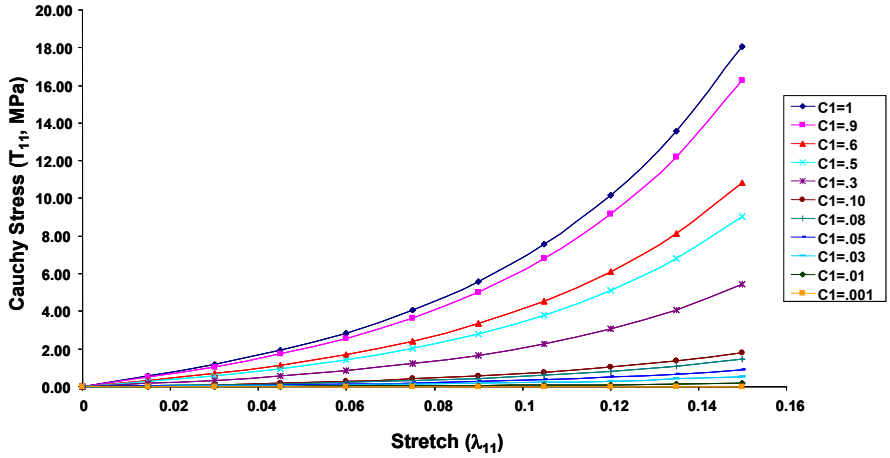

Figure 4.24: Effect of changing C1 on stress-stretch curve (C2 = 12)

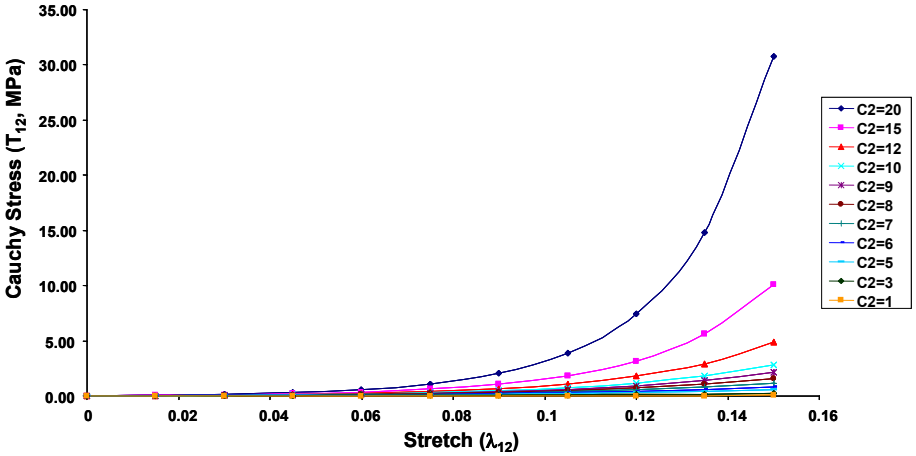

Figure 4.25: Effect of changing C2 on stress-stretch curve (C1 = 0.08 MPa)

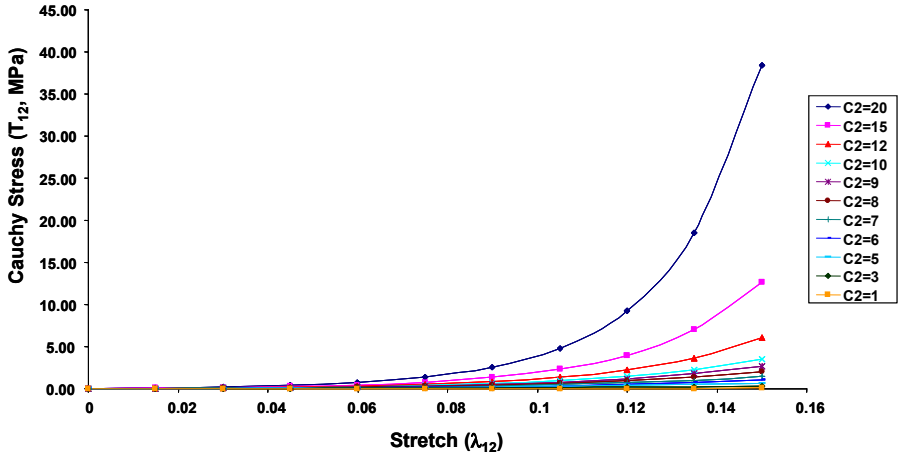

Figure 4.26: Effect of changing C2 on stress-stretch curve (C1 = 0.10 MPa)

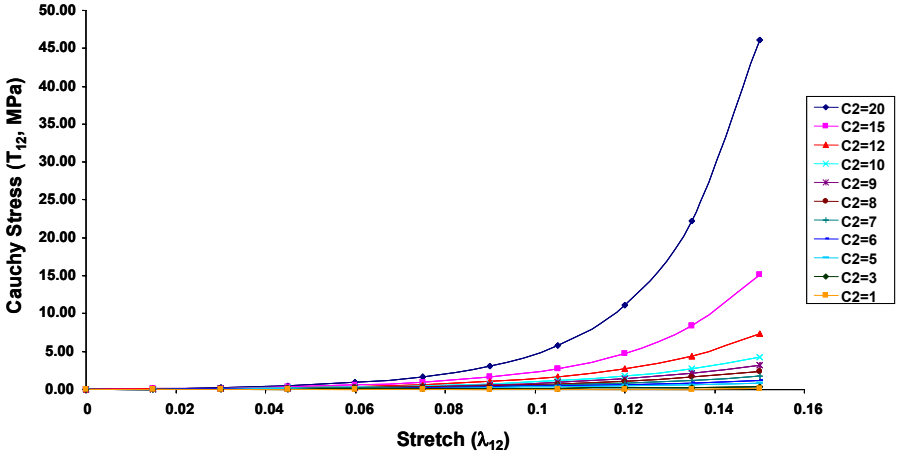

Figure 4.27: Effect of changing C2 on stress-stretch curve (C1 = 0.12 MPa)

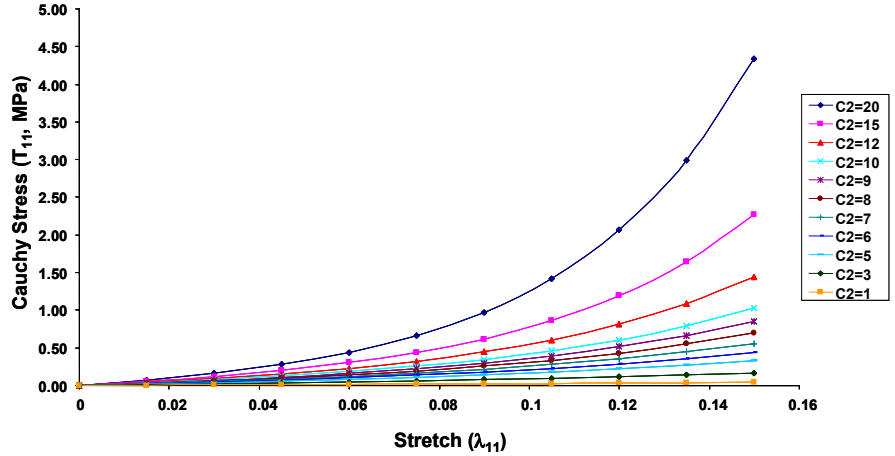

Figure 4.28: Effect of changing C2 on stress-stretch curve (C1 = 0.08 MPa)

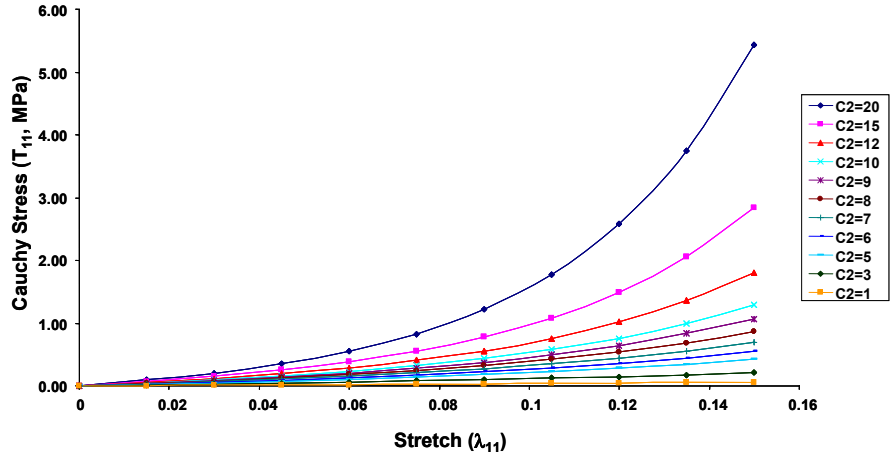

Figure 4.29: Effect of changing C2 on stress-stretch curve (C1 = 0.10 MPa)

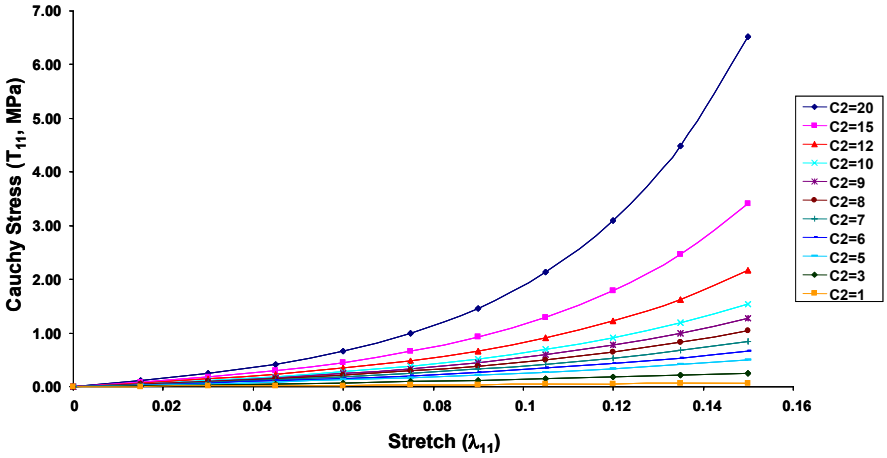

Figure 4.30: Effect of changing C2 on stress-stretch curve (C1 = 0.12 MPa)

4.2.3.4 Stress-stretch curve generation

Stress-stretch curves were generated for pure tensile and finite simple shear deformations of every tissue sample using the optimized constitutive coefficients. Again, because tensile and shear loading configurations have different stress-stretch relationships, the appropriate equations were used to generate the corresponding stress-stretch curves. Stretch values of 0.15 and 0.40 were used for tensile and shear configurations, respectively, to estimate the amount of stretch applied to the tissue sample during experimentation.

4.2.3.5 Generating average constitutive coefficients

In order to make comparisons between the axillary pouch and posterior regions of the capsule, average coefficients were determined. Simply taking the average of the optimized coefficients, however, would not be representative of the response of each tissue sample because of the non-linearity in the stress-stretch curves. Instead, the stress-stretch curves were divided into ten increments and the stresses for each step were averaged between specimens. These averaged

stresses were then used to generate an average stress-stretch curve for pure tensile and finite simple shear elongations in both the longitudinal and transverse direction. To obtain an average set of constitutive coefficients, the Cauchy stress equations for pure tensile and finite simple shear deformations were fit to the average stress-stretch curves using the least squares method, where the error between the curves was minimized using the non-linear Levenberg-Marquardt algorithm with a tolerance of 0.001. (Appendix A)

4.2.3.6 Non-converging finite element meshes

In some cases the finite element simulations were unable to converge to a solution due to inverting elements in the mesh. This was mostly evident during shear loading conditions of the posterior capsule, because the posterior capsule was the thinnest of the regions. For thin samples and as a final effort to make the models converge, a constraint of zero strain in the direction corresponding to the thickness of the tissue was applied, with the assumption that if the tissue is thin, minimal stress and strain occurred through the thickness. This was completed by replacing the "0" following the node number in the node control deck with a "3". (Appendix B)

4.2.3.7 Constitutive model validation

There are two aspects to validating the constitutive model – determination of the ability of the constitutive model to describe the experimentally measured forces and determination of the ability of the constitutive model to predict these quantities.

To evaluate the ability of the constitutive model to describe each of the four experimental datasets, we used standard measures of goodness-of-fit including R^2 values. We assessed the ability of the hyperelastic isotropic constitutive model to predict experimental data by comparing the coefficients of one loading direction to the coefficients of the perpendicular loading direction.

4.2.3.8 Data obtained / analysis

For each loading condition, a set of optimized C1 and C2 were obtained. These values were then used to generate stress-stretch curves for either pure tension (tensile loading conditions) or simple finite shear (shear loading conditions).

Several comparisons were made to determine the appropriateness of the isotropic constitutive model and difference between the axillary pouch and posterior region. Specifically, when determining the appropriateness of the constitutive model, the stresses of longitudinal and transverse loading directions (i.e. tensile longitudinal compared to tensile transverse and shear longitudinal compared to shear transverse) were compared at 11 points along the curve using a correlation coefficient as well as maximum (max) and average (avg) differences. In addition, the average stress-stretch curves were fit to the stress-stretch relationship described in Equations 4.16 (shear) and 4.17 (tensile) and an averaged set of coefficients were obtained for each loading configuration. These coefficients could then be compared, and based on the sensitivity analysis performed in Section 4.2.3.3 a difference greater then 0.3 MPa for C_1 or 3 for C_2 was considered significant.

To determine the differences between the two regions, the stress-stretch curves from the same loading condition (i.e. tensile longitudinal of the axillary pouch was compared to tensile longitudinal of the posterior region) were compared at 11 points along each curve. The average coefficients were also compared between regions, where differences greater then 0.3 MPa for C_1 or 3 for C_2 were considered significant.

4.3 RESULTS

4.3.1 Bi-directional Mechanical Tests - experimental

4.3.1.1 Tissue sample geometries

Overall, the posterior capsule was the thinnest region of the capsule, with an average thickness of 1.23 ± 0.43 mm. (Tables 4.4 – 4.13, where the loading conditions are as follows: apsl – axillary pouch shear longitudinal, apst – axillary pouch shear transverse, aptl – axillary pouch tensile longitudinal, aptt – axillary pouch tensile transverse, psl – posterior shear longitudinal, pst – posterior shear transverse, ptl – posterior tensile longitudinal, and ptt – posterior tensile transverse) The axillary pouch was the thickest region of the capsule with an average thickness of 2.61 ± 3.18 mm. In addition, a great deal of variability was noticed not only between specimens, but also across tissue samples themselves. For example, the thickness of one tissue sample ranged from 1.49 mm to 3.68 mm across its length.

Table 4.4: Tissue sample geometries (mm) of specimen ID: 05-10072L

	APSL	APST	APTL	APTT
Clamp to Clamp	14.00	14.00	15.00	15.00
Width (avg)	16.00	25.67	26.33	15.67
Thickness (avg)	2.72	2.87	2.64	2.06
Cross Sectional Area	43.52	73.75	69.52	32.22

	PSL	PST	PTL	PTT
Clamp to Clamp	14.00	15.00	15.00	15.00
Width (avg)	16.00	26.67	27.00	17.00
Thickness (avg)	1.22	1.19	1.31	1.45
Cross Sectional Area	19.47	31.64	35.37	24.71

Table 4.5: Tissue sample geometries (mm) of specimen ID: 05-08016R

	APSL	APST	APTL	APTT
Clamp to Clamp	15.00	15.00	15.00	15.00
Width (avg)	20.00	17.33	16.67	19.67
Thickness (avg)	2.16	1.81	1.28	2.33
Cross Sectional Area	43.13	31.32	21.33	45.76

	PSL	PST	PTL	PTT
Clamp to Clamp	16.00	15.00	14.00	16.00
Width (avg)	14.33	23.33	22.67	14.33
Thickness (avg)	0.82	0.83	0.83	0.86
Cross Sectional Area	11.71	19.44	18.89	12.28

Table 4.6: Tissue sample geometries (mm) of specimen ID: 05-10043R

	APSL	APST	APTL	APTT
Clamp to Clamp	17.00	14.00	15.00	16.00
Width (avg)	17.33	24.33	23.67	17.67
Thickness (avg)	1.99	2.52	2.21	2.27
Cross Sectional Area	34.55	61.24	52.22	40.04

	PSL	PST	PTL	PTT
Clamp to Clamp	14.00	14.00	15.00	15.00
Width (avg)	13.33	23.00	23.00	13.67
Thickness (avg)	1.41	1.22	1.30	1.40
Cross Sectional Area	18.84	28.14	29.98	19.18

Table 4.7: Tissue sample geometries (mm) of specimen ID: 05-11007R

	APSL	APST	APTL	APTT
Clamp to Clamp	14.00	15.00	16.00	15.00
Width (avg)	22.00	16.00	14.67	2.17
Thickness (avg)	2.96	2.47	3.34	22.00
Cross Sectional Area	65.19	39.57	48.99	47.81

	PSL	PST	PTL	PTT
Clamp to Clamp	14.00	15.00	16.00	15.00
Width (avg)	20.67	15.00	15.33	22.67
Thickness (avg)	1.07	0.98	0.62	1.01
Cross Sectional Area	22.18	14.75	9.56	22.89

Table 4.8: Tissue sample geometries (mm) of specimen ID: 05-08038L

	APSL	APST	APTL	APTT
Clamp to Clamp	15.00	15.00	14.00	15.00
Width (avg)	14.33	22.00	22.67	14.33
Thickness (avg)	2.27	2.62	2.24	2.32
Cross Sectional Area	32.49	57.71	50.77	33.25

	PSL	PST	PTL	PTT
Clamp to Clamp	14.00	15.00	15.00	14.00
Width (avg)	18.67	16.67	15.33	20.33
Thickness (avg)	0.90	1.26	1.18	0.79
Cross Sectional Area	16.80	21.06	18.04	16.00

Table 4.9: Tissue sample geometries (mm) of specimen ID: 05-08022L

	APSL	APST	APTL	APTT
Clamp to Clamp	16.00	13.00	13.00	15.00
Width (avg)	15.00	14.67	14.33	19.33
Thickness (avg)	2.17	1.83	1.51	2.07
Cross Sectional Area	32.50	26.84	21.64	40.02

	PSL	PST	PTL	PTT
Clamp to Clamp	17.00	15.00	15.00	17.00
Width (avg)	16.33	22.33	23.00	15.33
Thickness (avg)	2.35	1.86	0.81	1.99
Cross Sectional Area	38.44	41.61	18.63	30.51

Table 4.10: Tissue sample geometries (mm) of specimen ID: 05-08013L

	APSL	APST	APTL	APTT
Clamp to Clamp	16.00	14.00	15.00	15.00
Width (avg)	13.00	21.00	21.33	14.67
Thickness (avg)	1.66	1.51	1.60	1.80
Cross Sectional Area	21.54	31.78	34.20	26.45

	PSL	PST	PTL	PTT
Clamp to Clamp	18.00	13.00	14.00	18.00
Width (avg)	12.67	20.33	20.33	13.00
Thickness (avg)	0.78	1.26	1.16	0.92
Cross Sectional Area	9.84	25.62	23.59	11.92

Table 4.11: Tissue sample geometries (mm) of specimen ID: 05-08041L

	APSL	APST	APTL	APTT
Clamp to Clamp	15.00	13.00	15.00	16.00
Width (avg)	13.00	21.33	23.00	13.67
Thickness (avg)	1.56	1.51	0.89	1.72
Cross Sectional Area	20.24	32.14	20.55	23.55

	PSL	PST	PTL	PTT
Clamp to Clamp	14.00	14.00	15.00	16.00
Width (avg)	13.67	18.00	18.33	12.00
Thickness (avg)	1.69	1.83	1.97	1.89
Cross Sectional Area	23.14	32.88	36.06	22.72

Table 4.12: Tissue sample geometries (mm) of specimen ID: 05-08048L

	APSL	APST	APTL	APTT
Clamp to Clamp	13.00	13.00	16.00	13.00
Width (avg)	14.67	20.67	20.67	14.33
Thickness (avg)	2.70	2.11	1.77	2.75
Cross Sectional Area	39.55	43.61	36.51	39.42

	PSL	PST	PTL	PTT
Clamp to Clamp	15.00	16.00	15.00	16.00
Width (avg)	20.67	16.33	16.00	20.00
Thickness (avg)	1.44	0.86	1.10	0.59
Cross Sectional Area	29.76	14.05	17.55	11.73

Table 4.13: Tissue sample geometries (mm) of specimen ID: 05-10071R

	APSL	APST	APTL	APTT
Clamp to Clamp	16.00	17.00	16.00	17.00
Width (avg)	18.67	21.00	21.67	18.00
Thickness (avg)	2.28	1.61	1.97	2.13
Cross Sectional Area	42.50	33.88	42.68	38.34

	PSL	PST	PTL	PTT
Clamp to Clamp	14.00	15.00	16.00	16.00
Width (avg)	17.33	15.67	15.67	18.67
Thickness (avg)	0.99	0.71	0.58	0.71
Cross Sectional Area	17.10	11.18	9.03	13.25

4.3.1.2 Load-elongation curves

All load-elongation curves exhibited the typical non-linear toe region that progressed into a linear region that is expected with soft tissues. (Figures 4.35 – 4.54) In addition to the experimental load-elongation curves, the simulated load-elongation curves are also plotted to show the comparison for each loading condition. The average R^2 value between the experimental and simulated load-elongation curve was 0.993, with a range from 0.98 to 0.99. However, in several cases (PSL for specimen ID 05-10072L, PSL for specimen ID 05-08016R,

and PST for specimen ID 05-11007R) the fit between the curves showed a visible difference. These cases only occurred for the shear loading conditions of the posterior capsule, and may be attributed to the minimal thickness of the tissue samples.

4.3.1.3 Surface strain distributions for shear loading conditions

The strain distributions of the Green-Lagrange maximum principal strains during shear loading conditions (ε_{12}, Figures 4.31 and 4.32) were homogeneous across the entire tissue sample ranging from 17% strain in the top right corner of the tissue sample to 21% strain in the bottom left portion of the tissue sample, while tensile loading conditions (ε_{11}, Figures 4.33 and 4.34) exhibited more of a heterogeneous distribution, and ranged from 7% strain in the top left and bottom right corners of the tissue sample to 18% strain in the top right and bottom left corners of the tissue sample. An image of the tissue sample in the reference strain configuration (Ref) and the strained configuration (Strained) has been provided for both loading conditions to show actual deformation of the markers during the applied elongation.

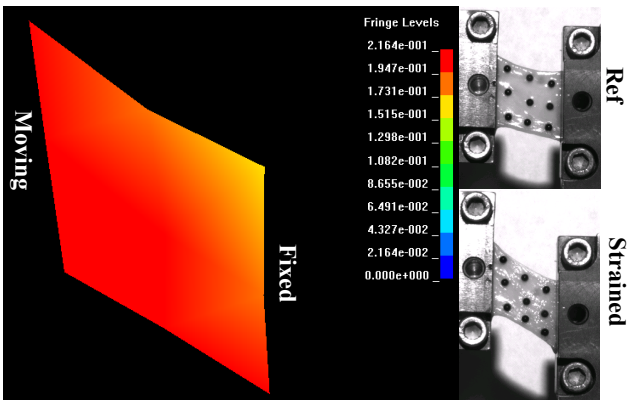

Figure 4.31: Green-Lagrange principal strain during the application of a shear elongation in the longitudinal direction with an image of the tissue in the reference (Ref) and strained (Strained) configuration (Specimen ID: 05-10071R)

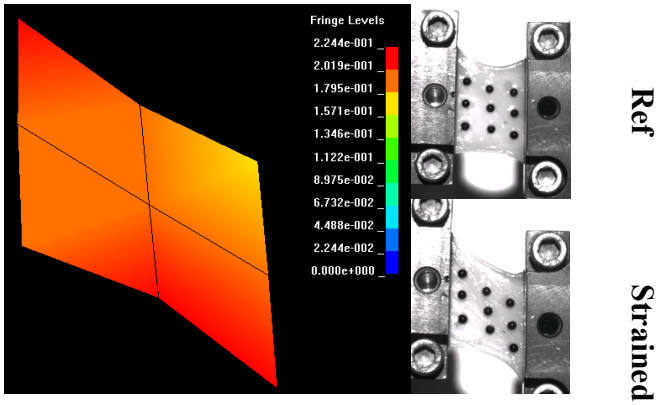

Figure 4.32: Green-Lagrange principal strain during the application of a shear elongation in the transverse direction with an image of the tissue in the reference (Ref) and strained (Strained) configuration (Specimen ID: 05-10071R)

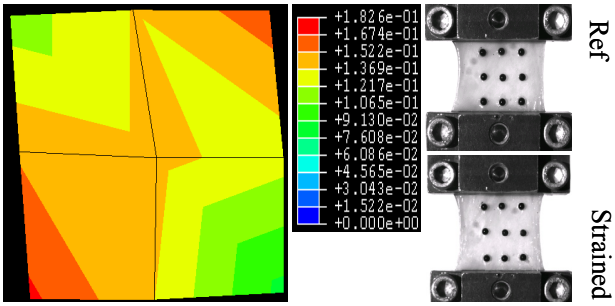

Figure 4.33: Green-Lagrange principal strain during the application of a tensile elongation in the longitudinal direction with an image of the tissue in the reference (Ref) and strained (Strained) configuration (Specimen ID: 05-10072L)

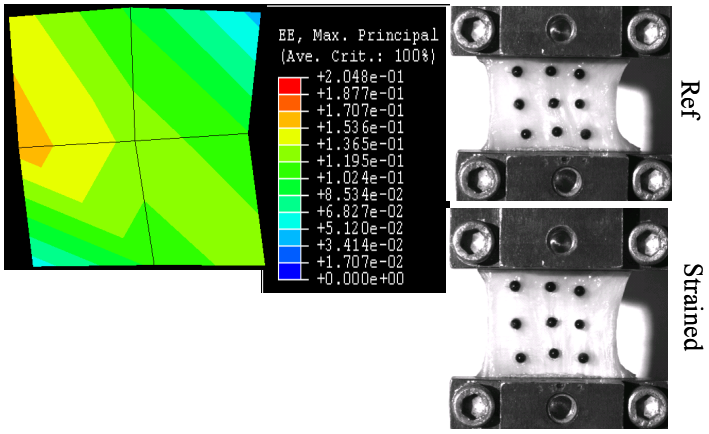

Figure 4.34: Green-Lagrange principal strain during the application of a tensile elongation in the transverse direction with an image of the tissue in the reference (Ref) and strained (Strained) configuration (Specimen ID: 05-10072L)

4.3.2 Bi-directional mechanical properties – computational

4.3.2.1 Constitutive coefficients

The optimized constitutive coefficients for each loading condition of all specimens used in this study are presented in Table 4.14, where the loading conditions are as follows: APSL – axillary pouch shear longitudinal, APST – axillary pouch shear transverse, APTL – axillary pouch tensile longitudinal, APTT – axillary pouch tensile transverse, PSL – posterior shear longitudinal, PST – posterior shear transverse, PTL – posterior tensile longitudinal, and PTT – posterior tensile transverse.

Minimal differences were found when comparing the longitudinal loading direction to the transverse loading direction for tensile and shear elongations. For example, the C_1 coefficient ranged from 0.05 to 1.08 MPa across all shear longitudinal loading conditions of the axillary pouch, with an average of 0.30 ± 0.37 MPa; while the C_1 coefficient ranged from 0.07 to 1.78 MPa across all shear transverse loading conditions of the axillary pouch, with an average of 0.47 ± 0.51 MPa. Additionally, the C_2 coefficient for all shear longitudinal loading conditions of the axillary pouch ranged from 2.1 to 11.0 with and average of 6.8 ± 3.6; while the C_2 coefficient for all shear transverse loading conditions of the axillary pouch ranged from 1.9 to 11.5 with and average of 6.0 ± 2.9. Because the C1 and C2 coefficients differed by less than 0.3 MPa and 3, respectively, the differences between loading directions were considered non-significant.

The C_1 coefficient ranged from 0.03 to 1.88 MPa across all loading conditions for the posterior region, with an average of 0.41 ± 0.40 MPa. The C_2 coefficient for all loading conditions of the posterior region ranged from 1.2 to 20.7 with and average of 8.5 ± 4.1. Comparing the C_1 and C_2 coefficients between the longitudinal and transverse directions, specifically tensile longitudinal to tensile transverse and shear longitudinal to shear transverse for

both the axillary pouch and posterior regions, minimal differences were found. Again, because the differences between the regions was less than 0.3 MPa and 3 for C_1 and C_2, respectively, the differences were considered to be non-significant.

Table 4.14: Optimized constitutive coefficients for all specimens

Specimen ID	05-10072L		05-08016R		05-10043R		05-11007R		05-10071R	
	C_1	C_2	C_1	C_2	C_1	C_2	C_1	C_2	C_1	C_2
APSL	0.06	10.3	0.83	2.2	0.17	8.4	0.48	3.7	0.09	3.6
APST	0.51	3.8	1.78	1.9	0.07	9.5	0.42	3.8	0.20	4.0
APTL	0.49	8.3	0.52	9.3	0.13	11.7	0.39	5.5	0.06	15.6
APTT	0.30	11.3	0.13	6.5	0.24	7.1	0.16	10.3	0.09	11.1
PSL	0.77	3.3	0.37	2.7	0.14	7.2	0.13	10.1	1.88	1.2
PST	0.11	7.4	0.94	3.2	0.20	6.0	0.30	10.0	0.46	2.7
PTL	0.19	13.7	0.49	5.6	0.03	20.7	0.45	11.9	1.24	7.0
PTT	0.10	13.4	0.78	5.0	0.43	5.3	0.41	5.0	0.22	8.7

Specimen ID	05-08038L		05-08022L		05-08013L		05-08041R		05-08048L	
	C_1	C_2	C_1	C_2	C_1	C_2	C_1	C_2	C_1	C_2
APSL	0.07	9.1	0.06	10.1	0.05	11.0	0.10	9.3	1.08	2.1
APST	0.28	5.6	0.25	5.3	0.11	11.5	0.81	6.3	0.28	7.9
APTL	0.11	14.5	0.31	8.1	0.12	13.4	0.22	11.8	0.13	17.7
APTT	0.12	8.1	0.15	8.8	0.06	8.4	0.13	8.3	0.14	17.2
PSL	0.20	9.3	0.16	5.3	0.30	5.8	0.09	11.7	0.16	7.3
PST	0.07	15.0	0.17	8.8	0.10	12.3	0.05	16.9	1.00	7.9
PTL	0.59	9.1	0.21	10.3	0.33	8.1	0.18	12.2	0.38	7.9
PTT	0.69	6.5	0.21	6.2	0.54	7.0	0.15	10.3	1.35	11.7

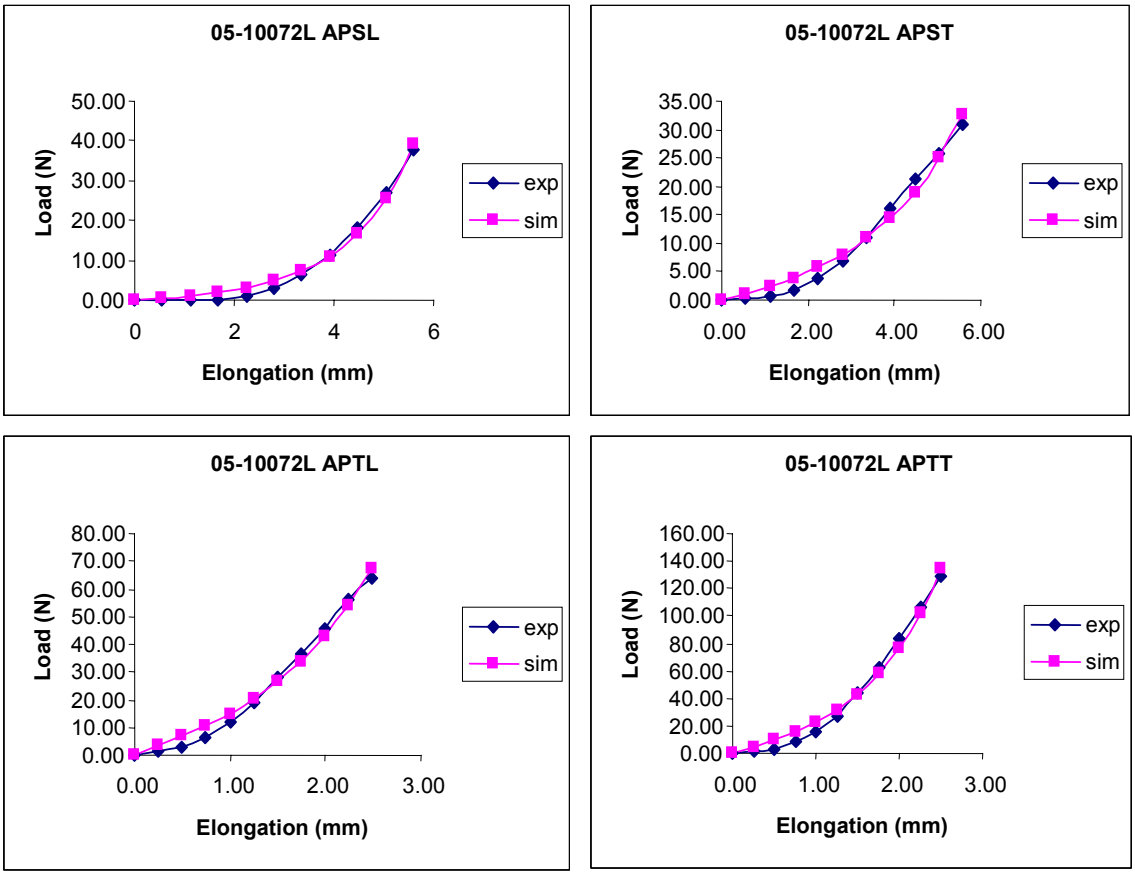

Figure 4.35: Experimental and computational load-elongation curves for specimen ID: 05-10072L – axillary pouch

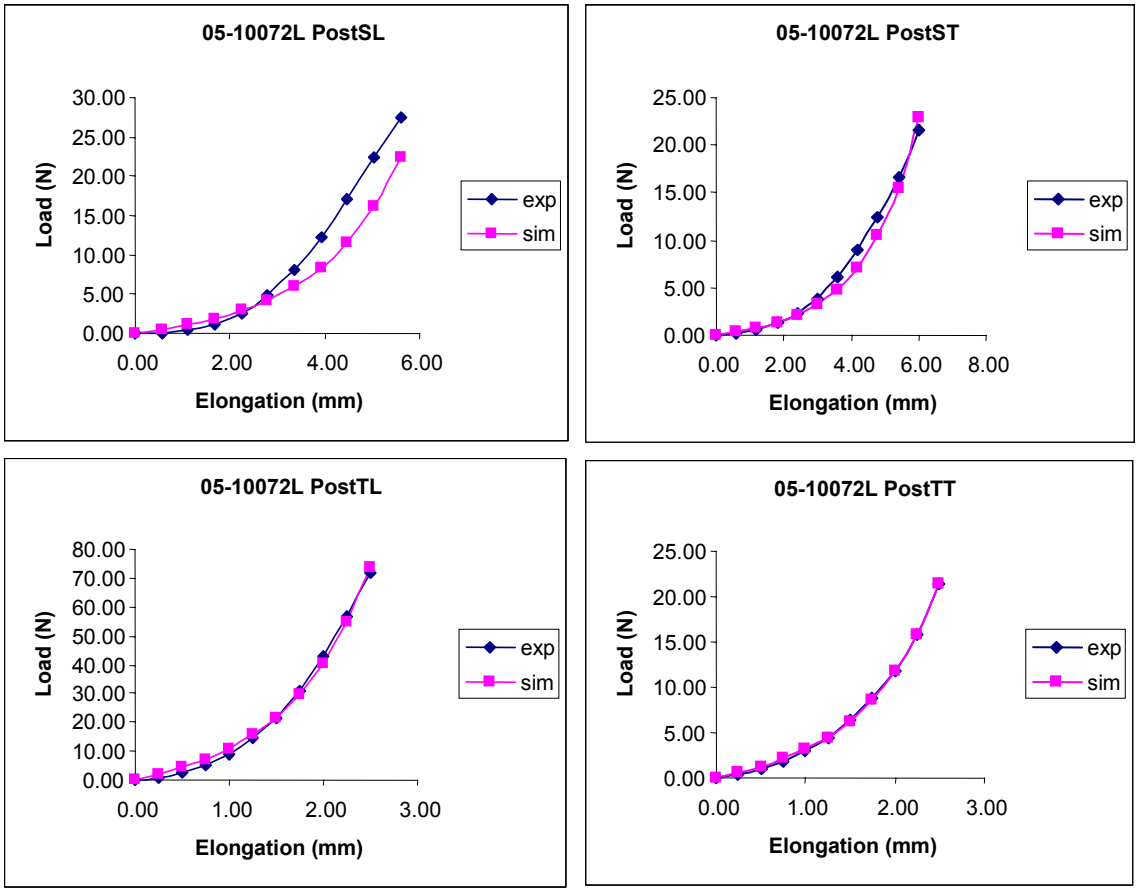

Figure 4.36: Experimental and computational load-elongation curves for specimen ID: 05-10072L – posterior region

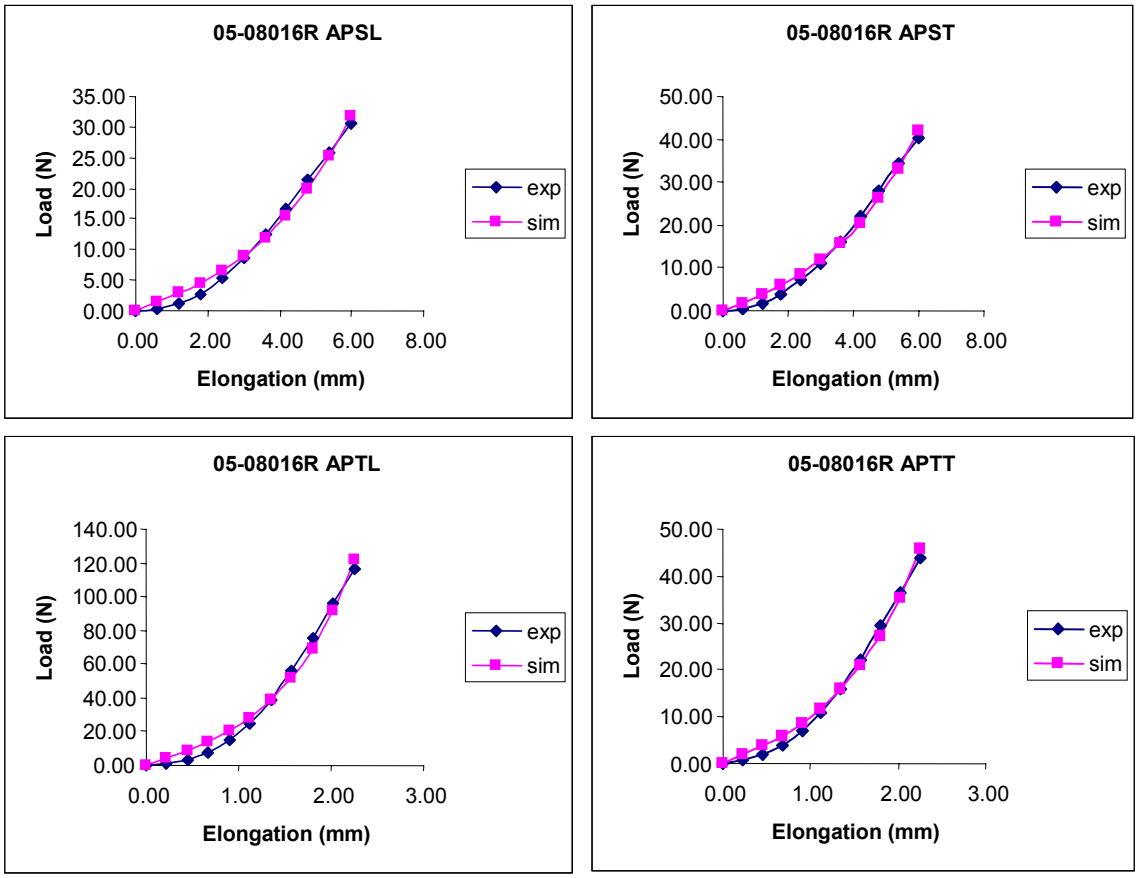

Figure 4.37: Experimental and computational load-elongation curves for specimen ID: 05-08016R – axillary pouch

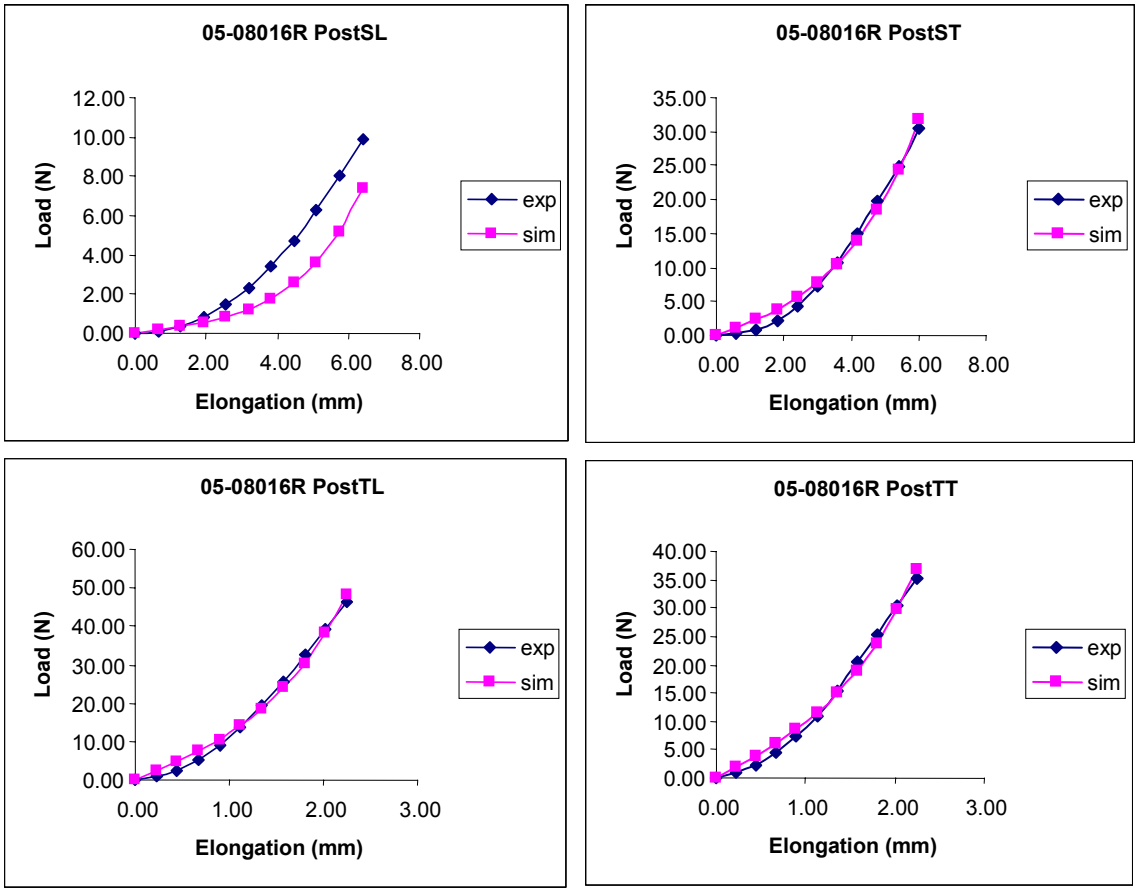

Figure 4.38: Experimental and computational load-elongation curves for specimen ID: 05-08016R – posterior region

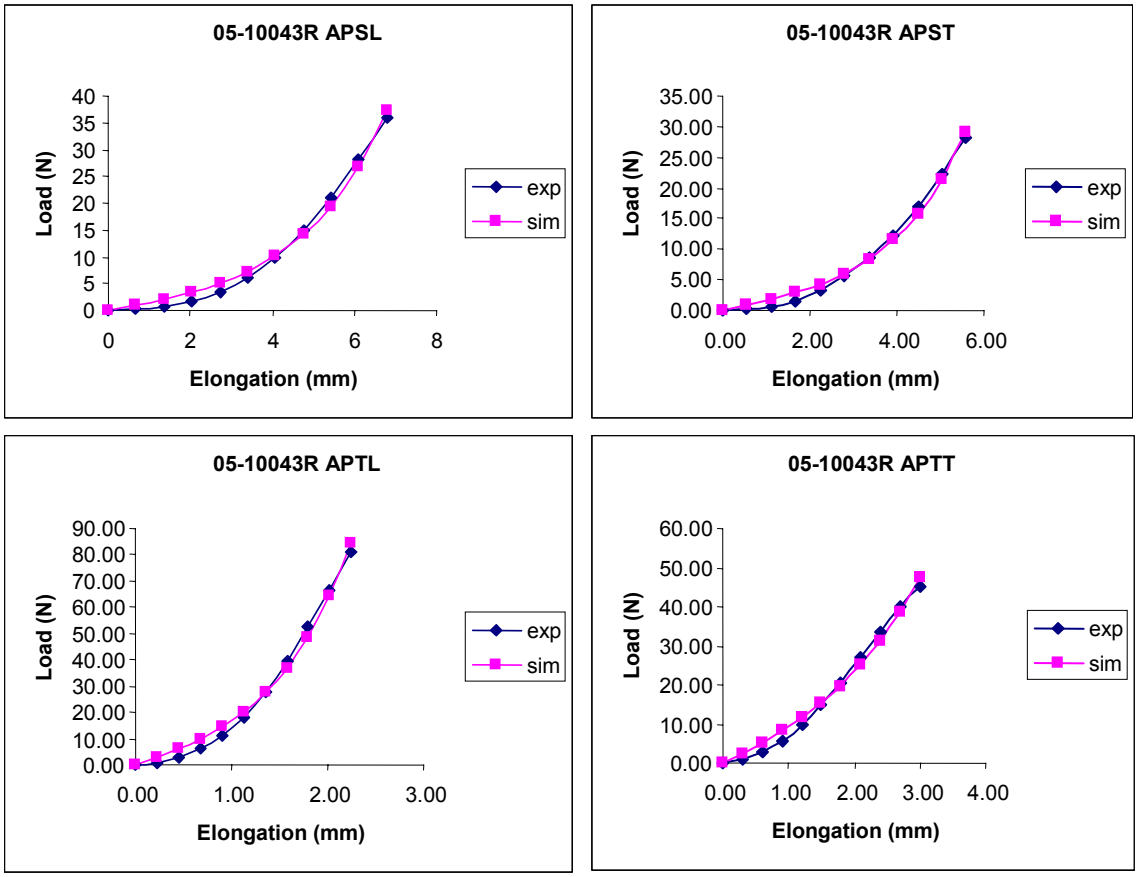

Figure 4.39: Experimental and computational load-elongation curves for specimen ID: 05-10043R – axillary pouch

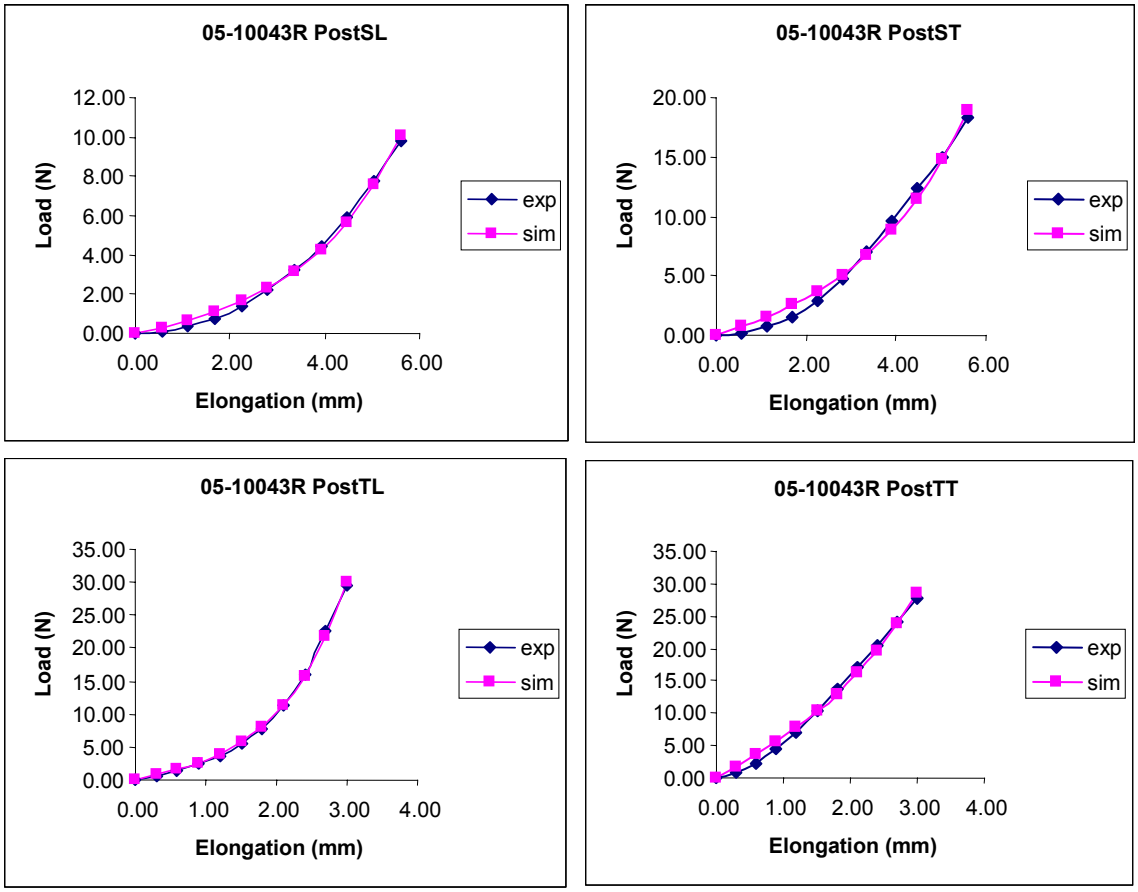

Figure 4.40: Experimental and computational load-elongation curves for specimen ID: 05-10043R – posterior region

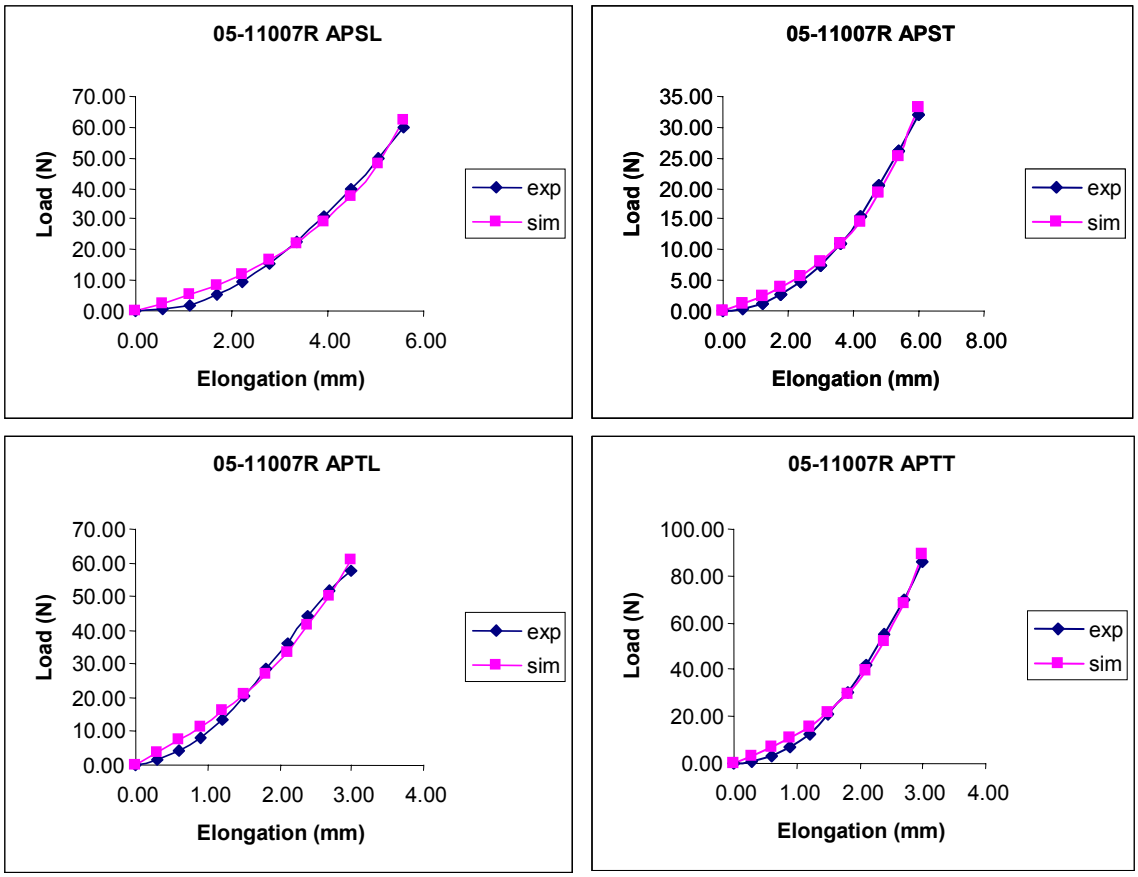

Figure 4.41: Experimental and computational load-elongation curves for specimen ID: 05-11007R – axillary pouch

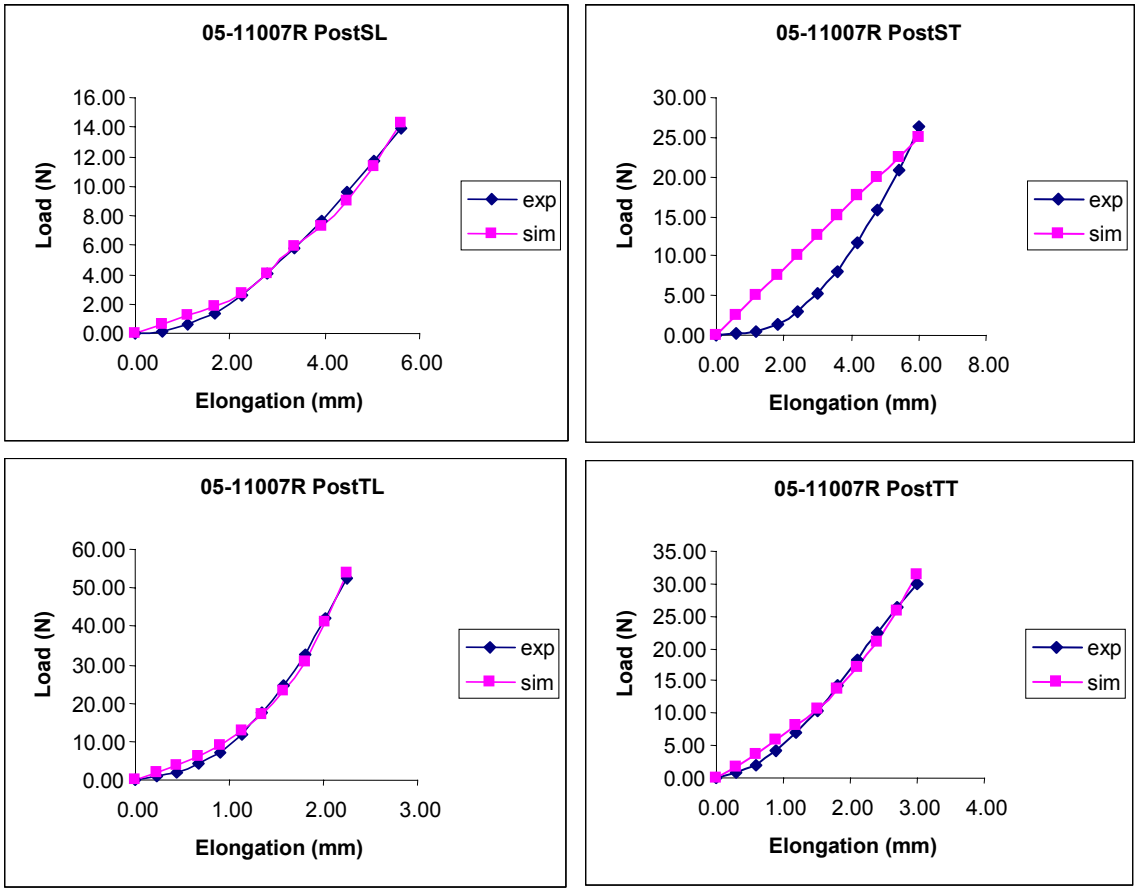

Figure 4.42: Experimental and computational load-elongation curves for specimen ID: 05-11007R –posterior region

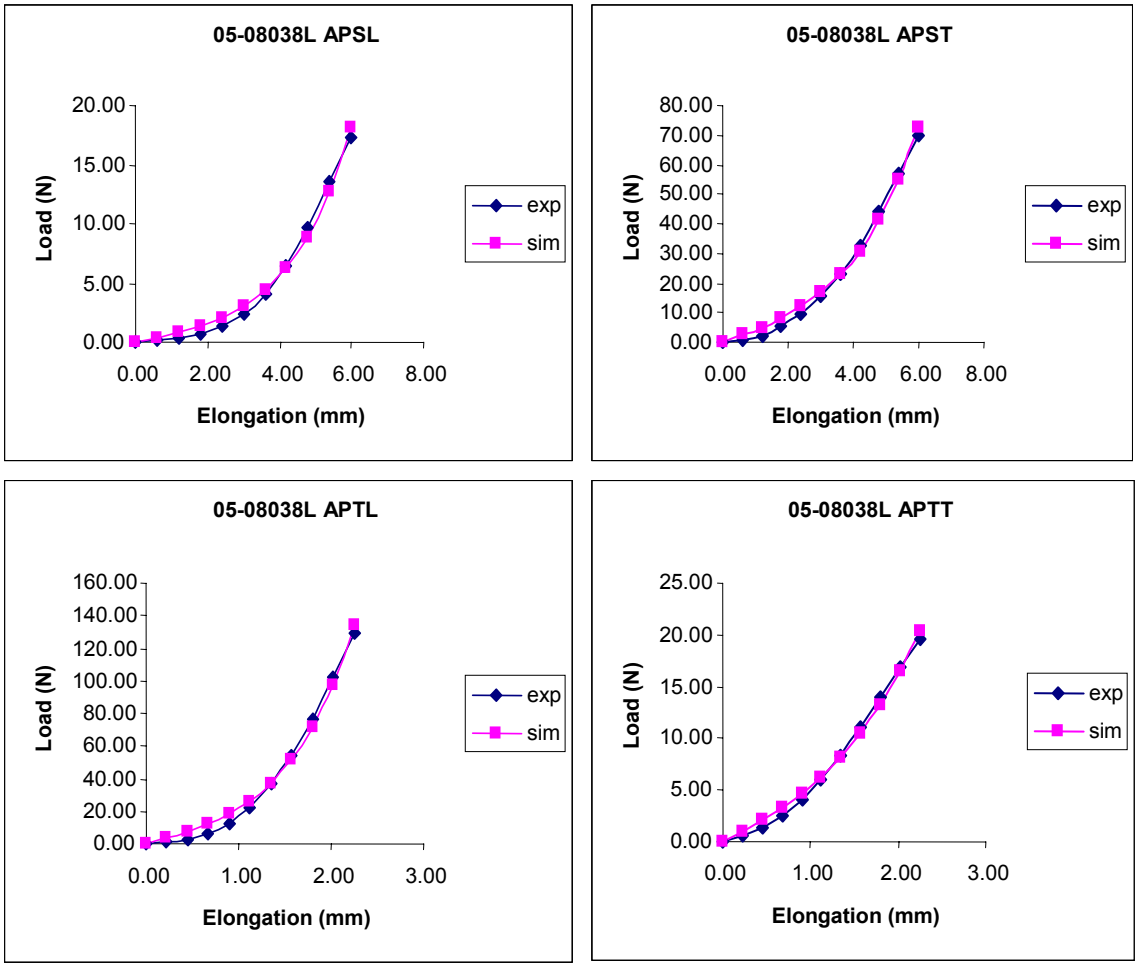

Figure 4.43: Experimental and computational load-elongation curves for specimen ID: 05-08038L – axillary pouch

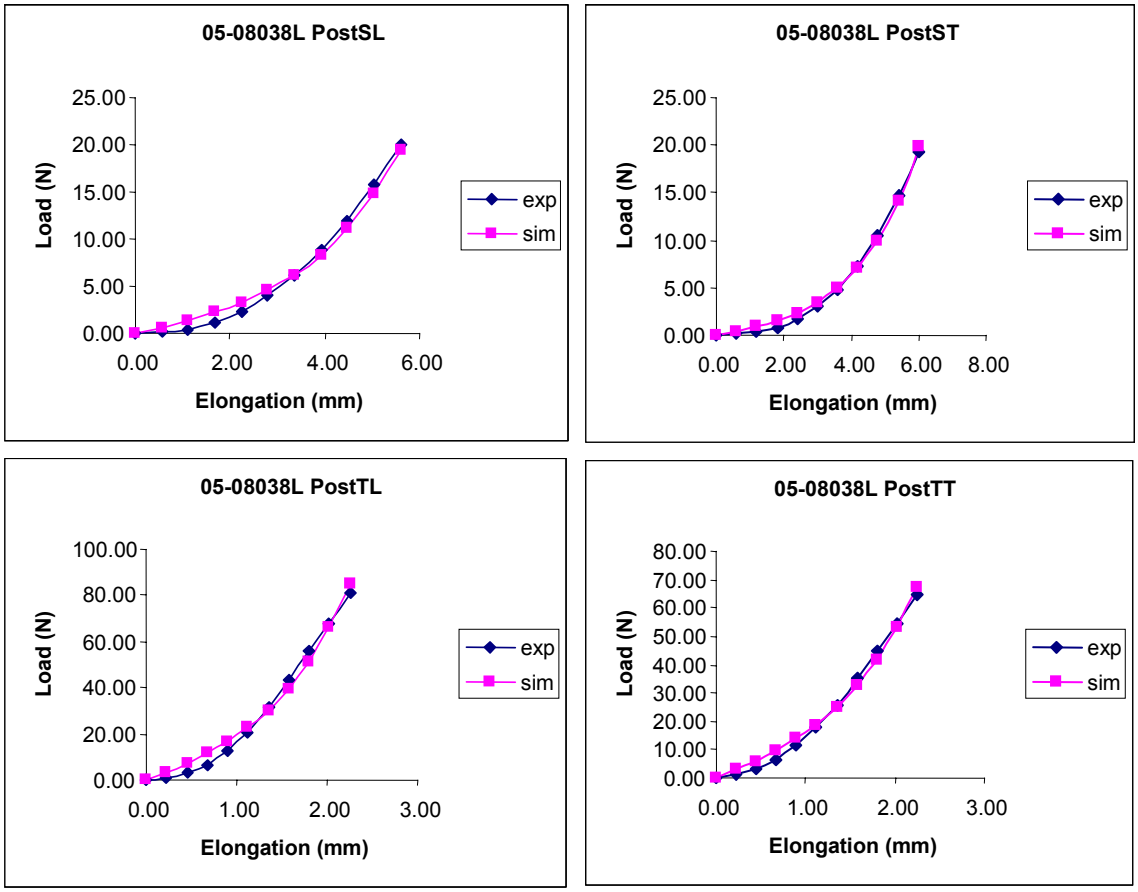

Figure 4.44: Experimental and computational load-elongation curves for specimen ID: 05-08038L – posterior region

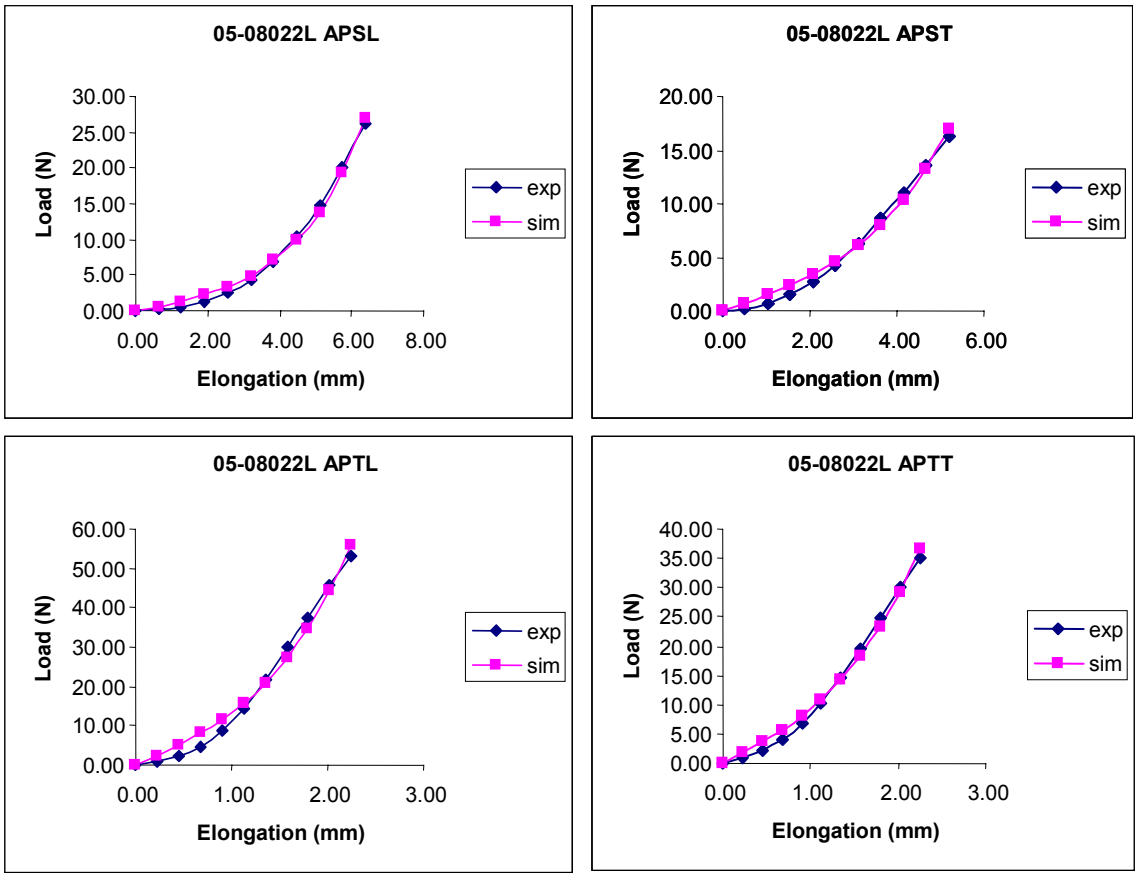

Figure 4.45: Experimental and computational load-elongation curves for specimen ID: 05-08022L – axillary pouch

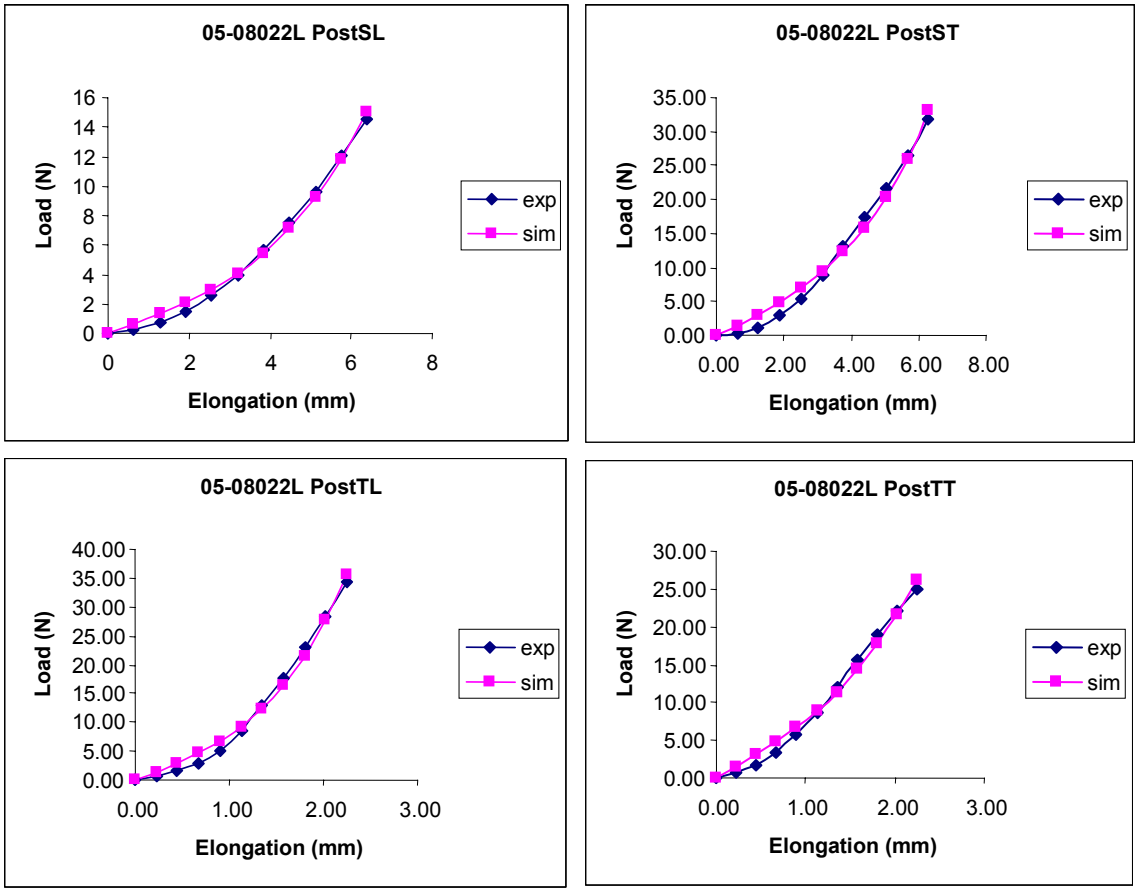

Figure 4.46: Experimental and computational load-elongation curves for specimen ID: 05-08022L – posterior region

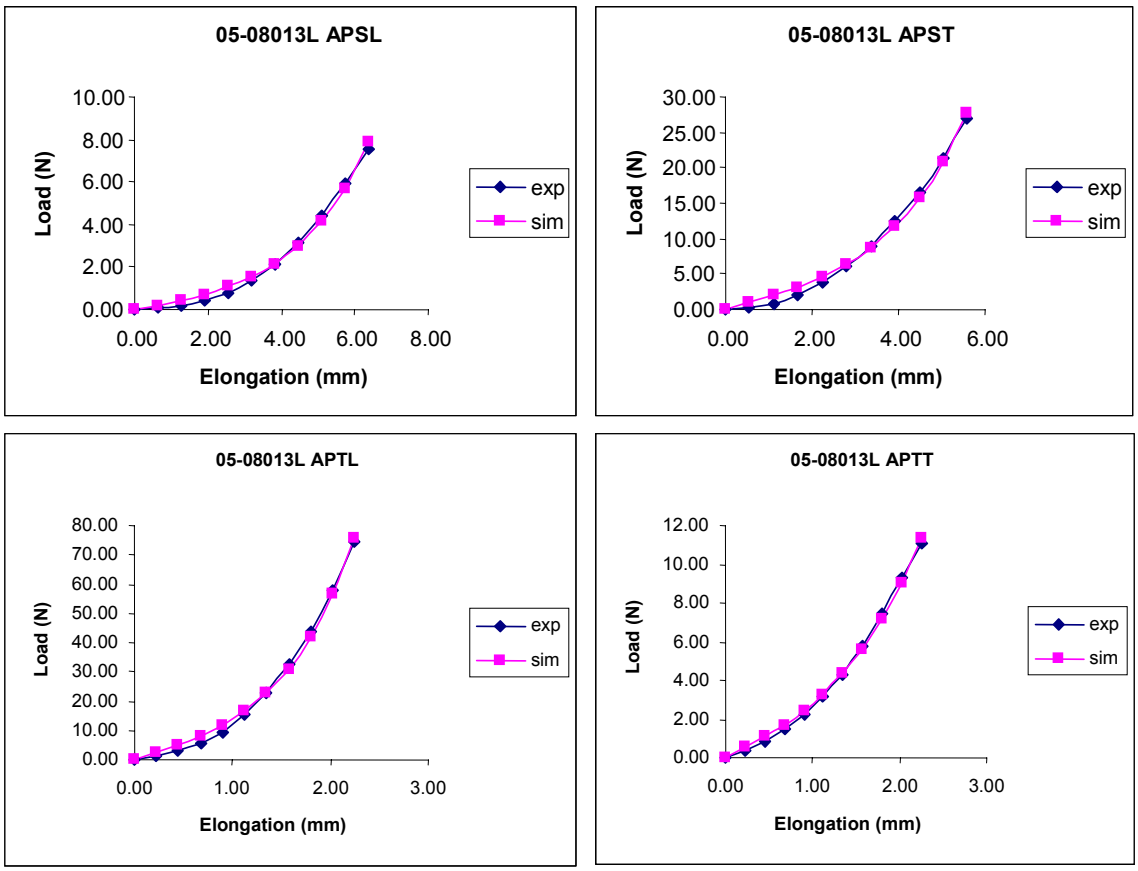

Figure 4.47: Experimental and computational load-elongation curves for specimen ID: 05-08013L – axillary pouch

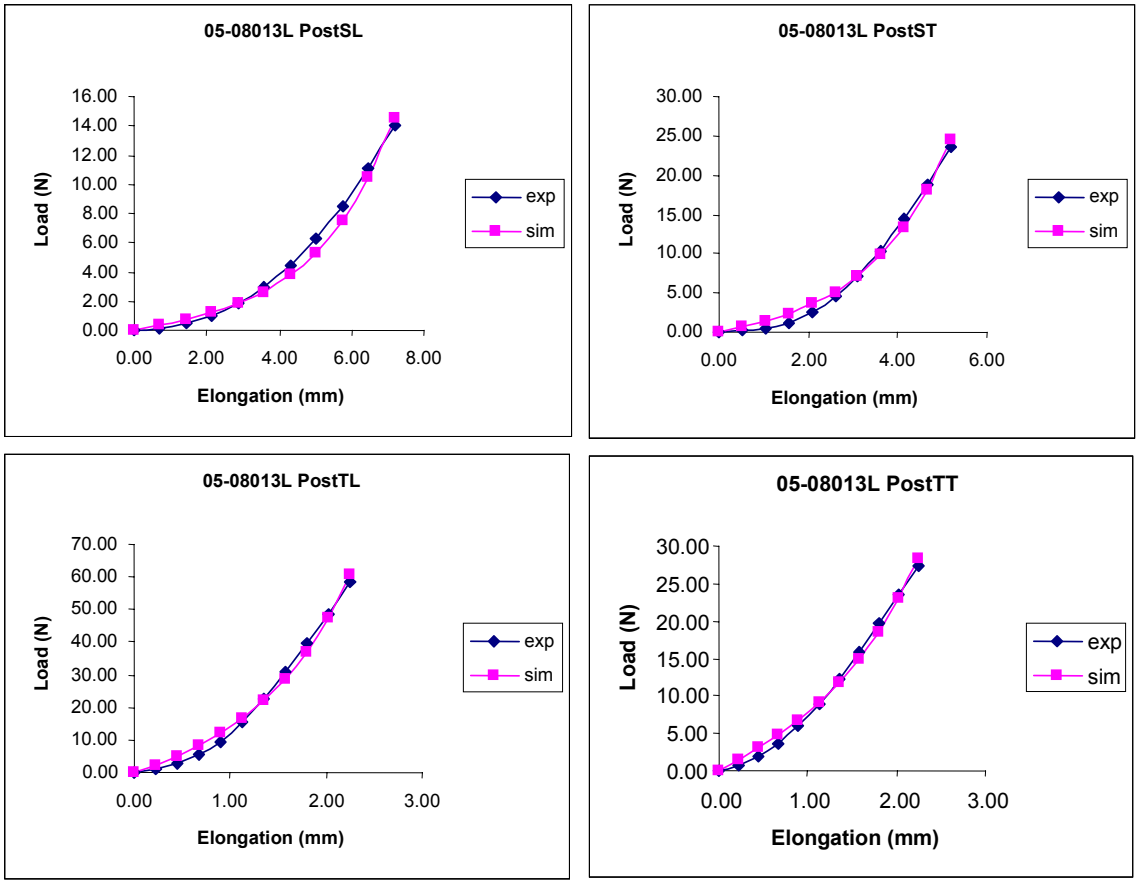

Figure 4.48: Experimental and computational load-elongation curves for specimen ID: 05-08013L – posterior region

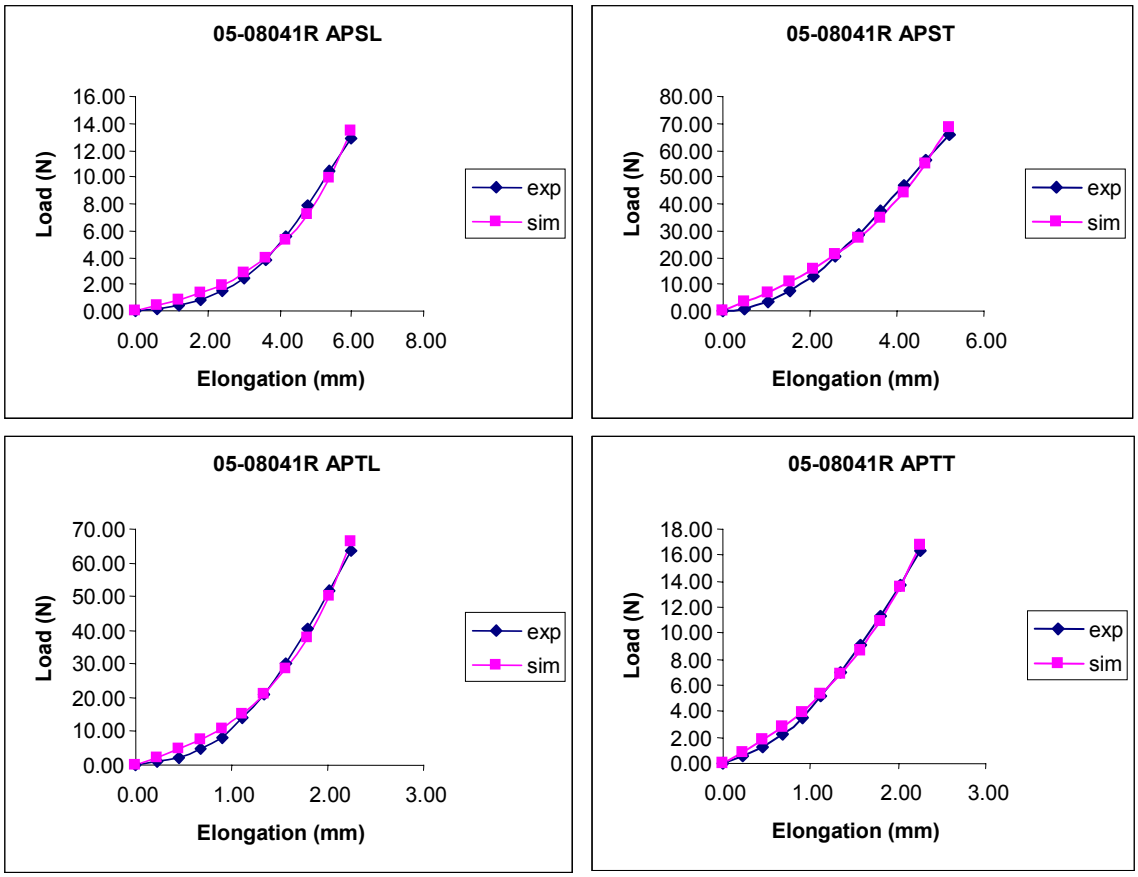

Figure 4.49: Experimental and computational load-elongation curves for specimen ID: 05-08041L – axillary pouch

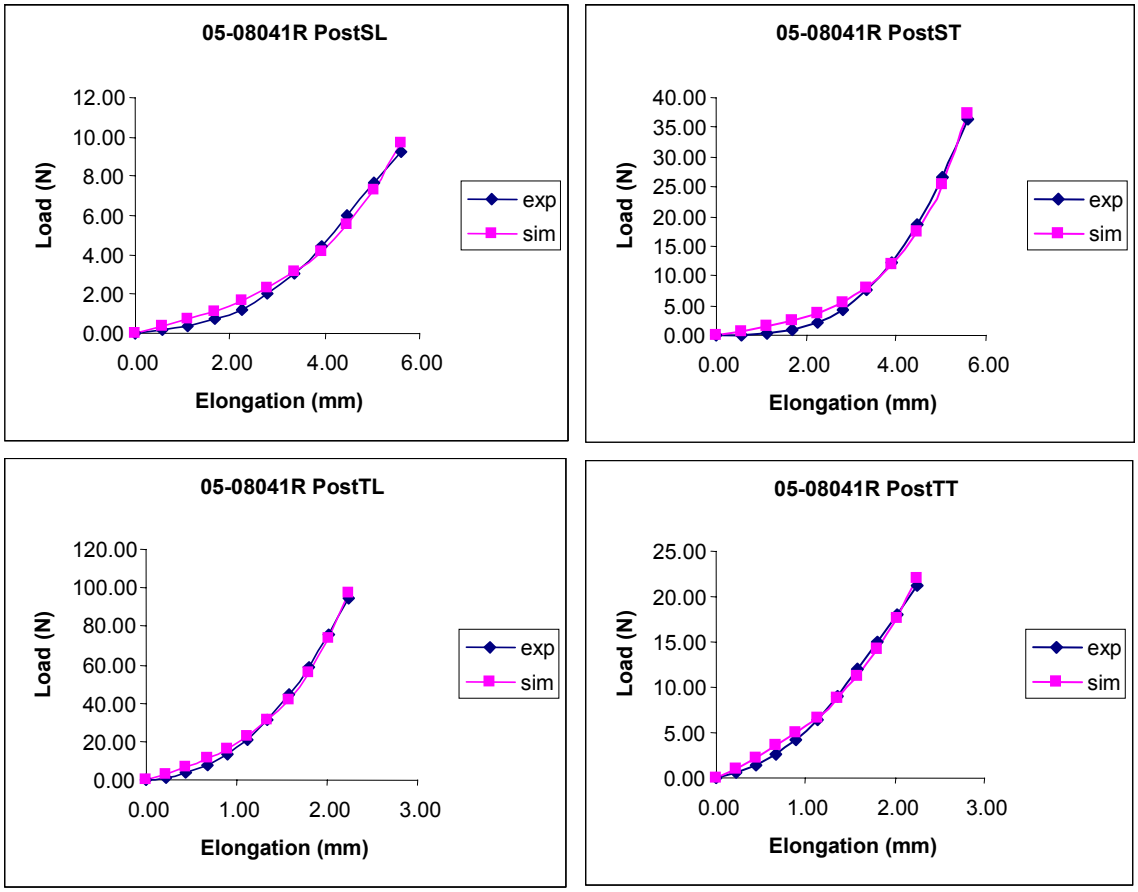

Figure 4.50: Experimental and computational load-elongation curves for specimen ID: 05-08041L – posterior region

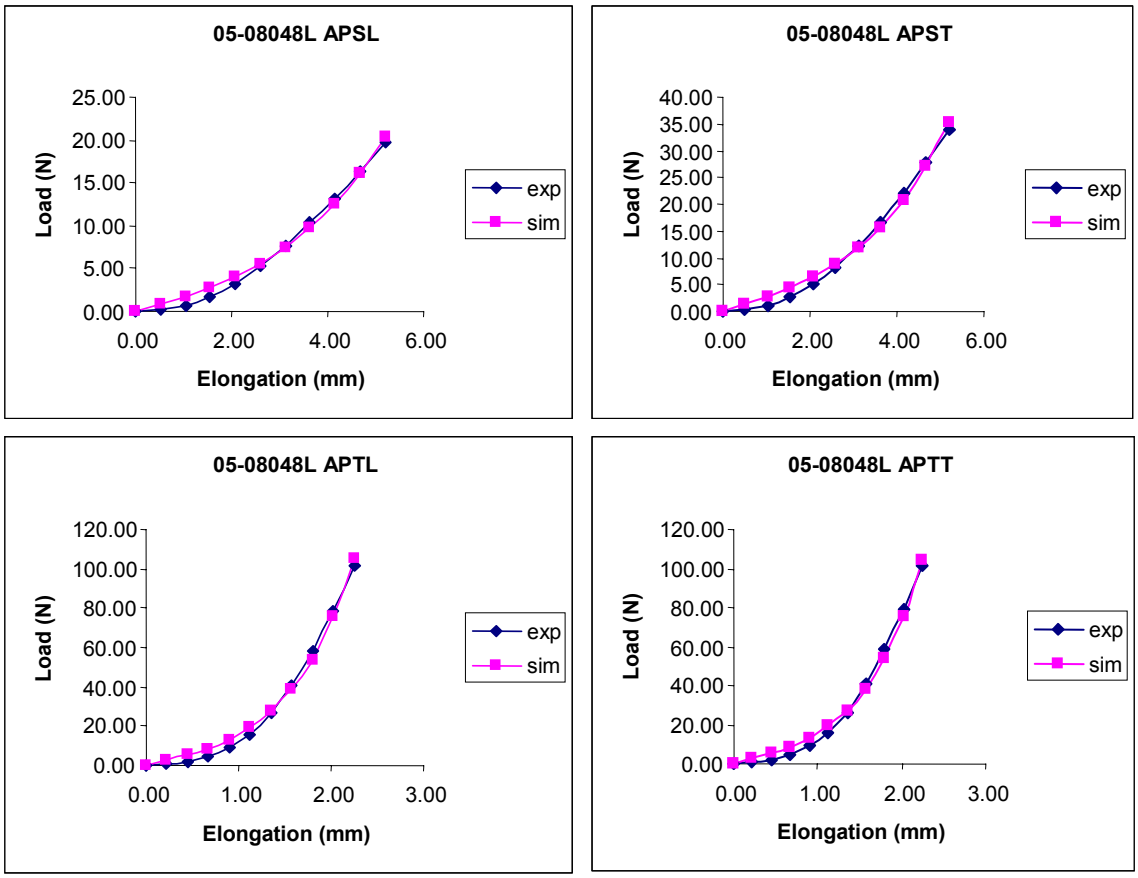

Figure 4.51: Experimental and computational load-elongation curves for specimen ID: 05-08048L – axillary pouch

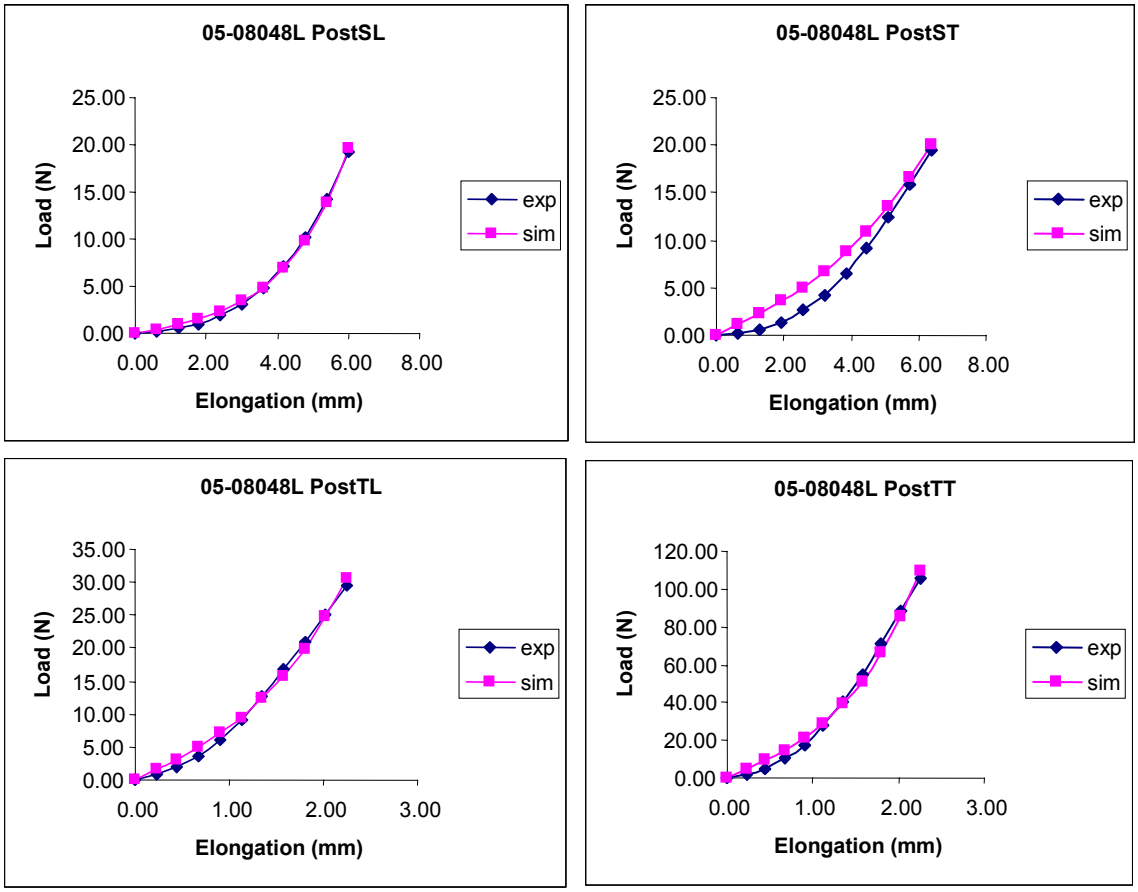

Figure 4.52: Experimental and computational load-elongation curves for specimen ID: 05-08048L – posterior region

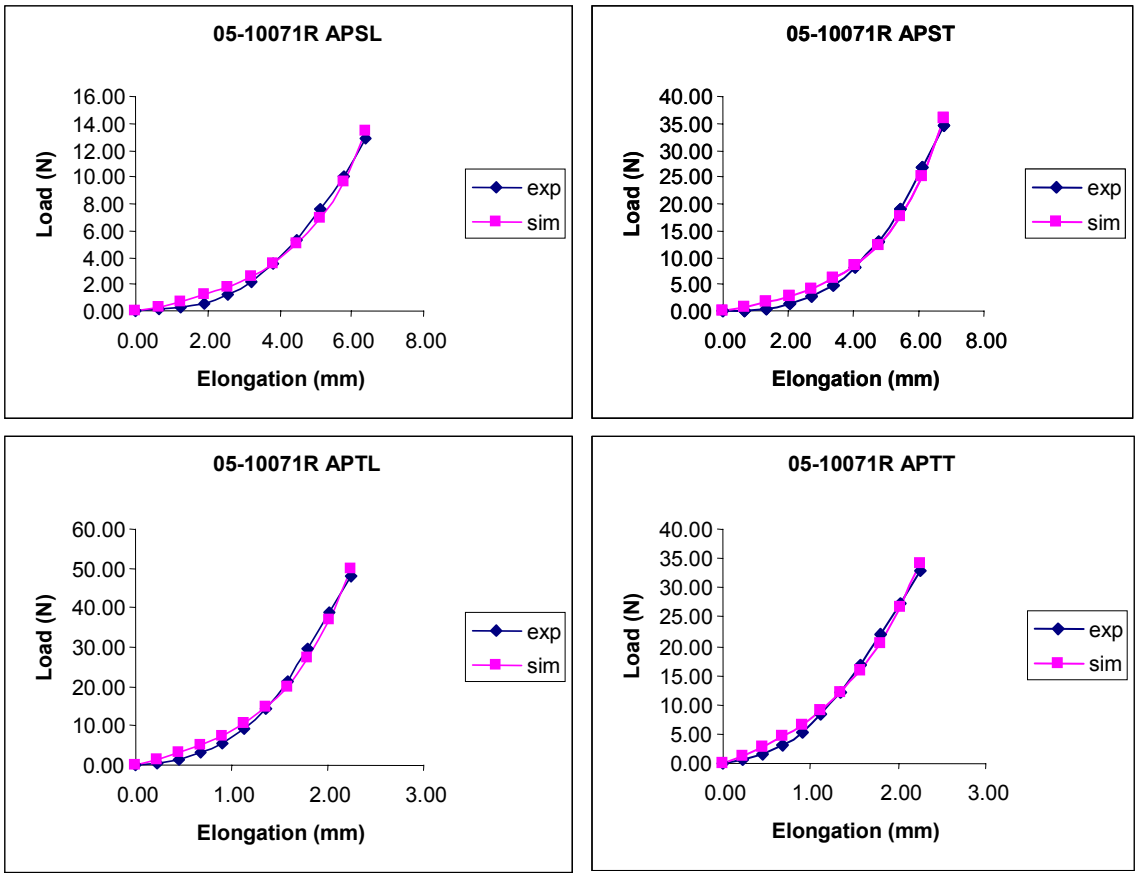

Figure 4.53: Experimental and computational load-elongation curves for specimen ID: 05-10071R – axillary pouch

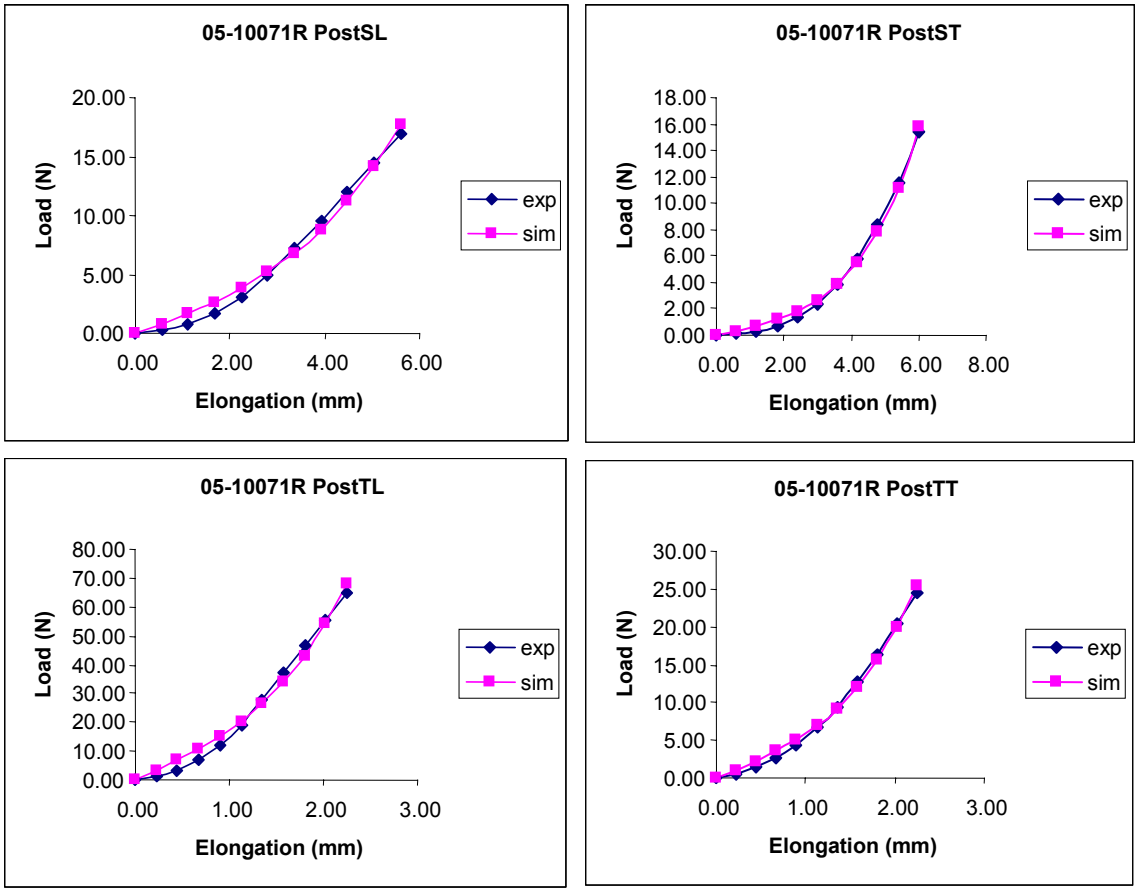

Figure 4.54: Experimental and computational load-elongation curves for specimen ID: 05-10071R – posterior region

4.3.2.2 Stress-stretch results

All stress-stretch curves exhibited the typical soft-tissue non-linear toe region that progressed into a linear region. (Figures 4.55-4.74) The average difference of stress between pure tension in the longitudinal and transverse loading directions of the axillary pouch across all specimens was only 0.46 ± 0.53 MPa, and only 0.54 ± 0.58 MPa when comparing shear longitudinal to shear transverse loading directions. The average difference of stress between pure tension in the longitudinal and transverse direction of the posterior region across all specimens was 1.42 ± 1.95 MPa, and 0.99 ± 1.31 MPa when comparing simple finite shear in the longitudinal direction to simple finite shear in the transverse direction. (Tables 4.15 – 4.24) For all cases, the correlation coefficient between the stress-stretch curves in the longitudinal and transverse loading directions exceeded 0.97.

In addition, when comparing one loading configuration of the axillary pouch to the same loading configuration of the posterior region (i.e. comparing APTL to PTL) the average differences were 0.40 ± 0.24, 0.90 ± 1.20, 0.84 ± 0.90, and 1.14 ± 1.82 MPa for shear longitudinal, shear transverse, tensile longitudinal and tensile transverse loading configurations, respectively.

After averaging all stress-stretch curves for each loading configuration to obtain one curve per loading configuration (Figures 4.75 and 4.76), the maximum differences in stress between the tensile loading conditions for the axillary pouch and posterior region were 1.36 and 0.25 MPa, respectively. The maximum differences in stress between the shear loading conditions for the axillary pouch and posterior region were 1.31 and 3.73 MPa, respectively. Based on the preliminary work that determined the sensitivity of the stress-stretch curves to the

constitutive coefficients (Section 4.2.3.3), these minimal differences between the curves correspond to the mechanical properties of the tissue samples being similar.

Table 4.15: Stress-stretch data for specimen ID: 05-10072L

Shear					Tensile				
stretch	stress (MPa)				stress (MPa)				stretch
	APSL	APST	PSL	PST	APTL	APTT	PTL	PTT	
0.00	0.00	0.00	0.00	0.00	0.00	0.00	0.00	0.00	0.00
0.04	0.02	0.08	0.10	0.03	0.19	0.15	0.12	0.06	0.02
0.08	0.05	0.16	0.21	0.07	0.39	0.33	0.26	0.13	0.03
0.12	0.09	0.26	0.34	0.12	0.63	0.53	0.43	0.21	0.05
0.16	0.15	0.37	0.48	0.19	0.91	0.79	0.64	0.32	0.06
0.20	0.24	0.51	0.66	0.28	1.25	1.11	0.92	0.45	0.08
0.24	0.37	0.69	0.87	0.40	1.66	1.52	1.28	0.63	0.09
0.28	0.57	0.92	1.14	0.59	2.17	2.04	1.77	0.87	0.11
0.32	0.89	1.20	1.48	0.85	2.80	2.72	2.42	1.18	0.12
0.36	1.39	1.58	1.91	1.24	3.58	3.61	3.29	1.60	0.14
0.40	2.20	2.06	2.45	1.81	4.55	4.76	4.45	2.16	0.15

max diff	0.34	0.67	0.21	2.29
avg diff	0.19	0.37	0.09	0.72
correlation	0.976	0.987	0.999	1.000

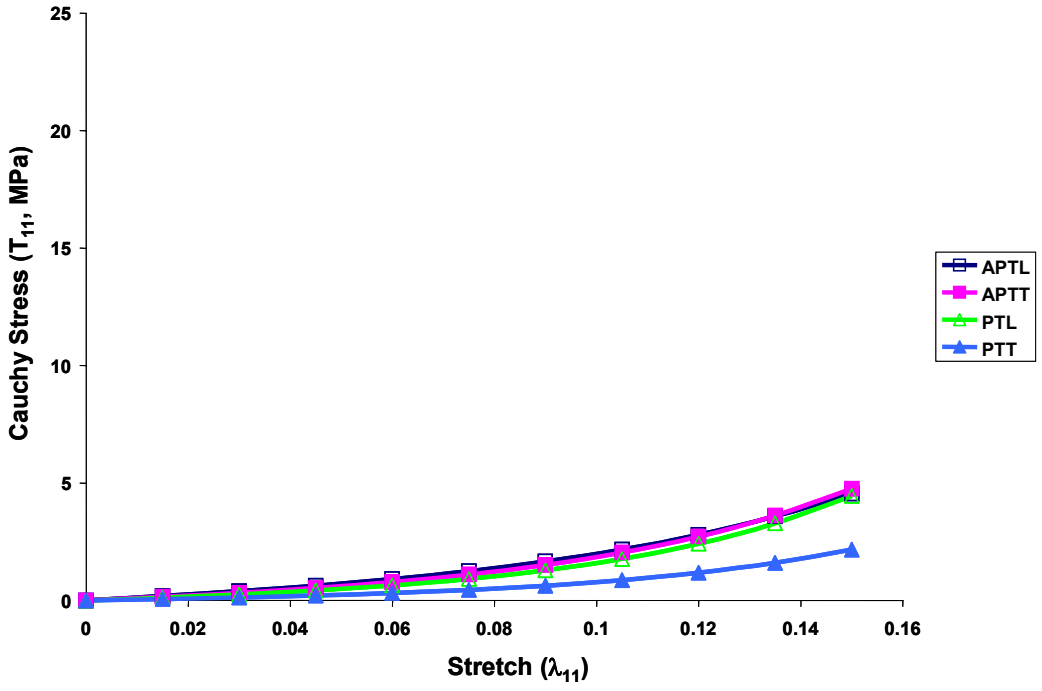

Figure 4.55: Stress-stretch curves for pure tension of specimen ID: 05-10072L

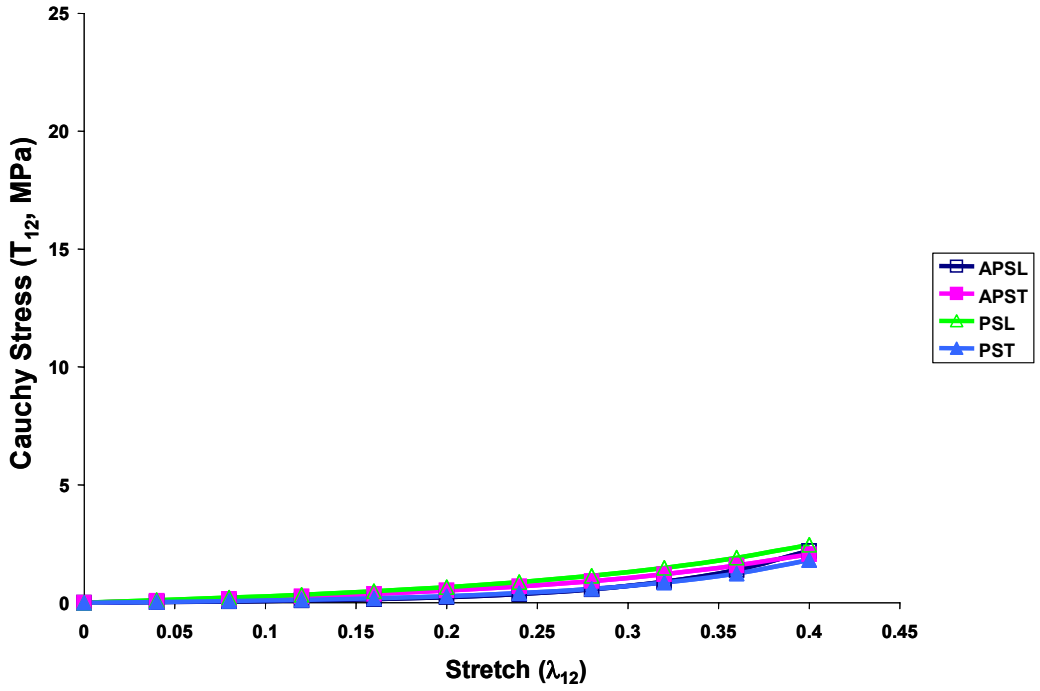

Figure 4.56: Stress-stretch curves for simple finite shear of specimen ID: 05-10072L

Table 4.16: Stress-stretch data for specimen ID: 05-08016R

Shear					Tensile				
stretch	stress (MPa)				stress (MPa)				stretch
	APSL	APST	PSL	PST	APTL	APTT	PTL	PTT	
0.00	0.00	0.00	0.00	0.00	0.00	0.00	0.00	0.00	0.00
0.04	0.07	0.14	0.04	0.12	0.22	0.04	0.13	0.18	0.02
0.08	0.15	0.28	0.08	0.25	0.47	0.08	0.26	0.37	0.03
0.12	0.23	0.44	0.13	0.39	0.75	0.13	0.41	0.57	0.05
0.16	0.33	0.61	0.18	0.56	1.09	0.19	0.58	0.81	0.06
0.20	0.43	0.80	0.24	0.76	1.51	0.25	0.78	1.07	0.08
0.24	0.56	1.02	0.31	1.01	2.03	0.33	1.01	1.38	0.09
0.28	0.70	1.28	0.40	1.32	2.69	0.42	1.28	1.74	0.11
0.32	0.88	1.58	0.51	1.70	3.51	0.53	1.60	2.16	0.12
0.36	1.09	1.94	0.65	2.19	4.54	0.66	1.98	2.65	0.14
0.40	1.35	2.37	0.81	2.80	5.85	0.82	2.43	3.22	0.15

max diff	1.03	1.99	5.03	0.79
avg diff	0.42	0.70	1.75	0.33
correlation	1.000	0.999	0.998	1.000

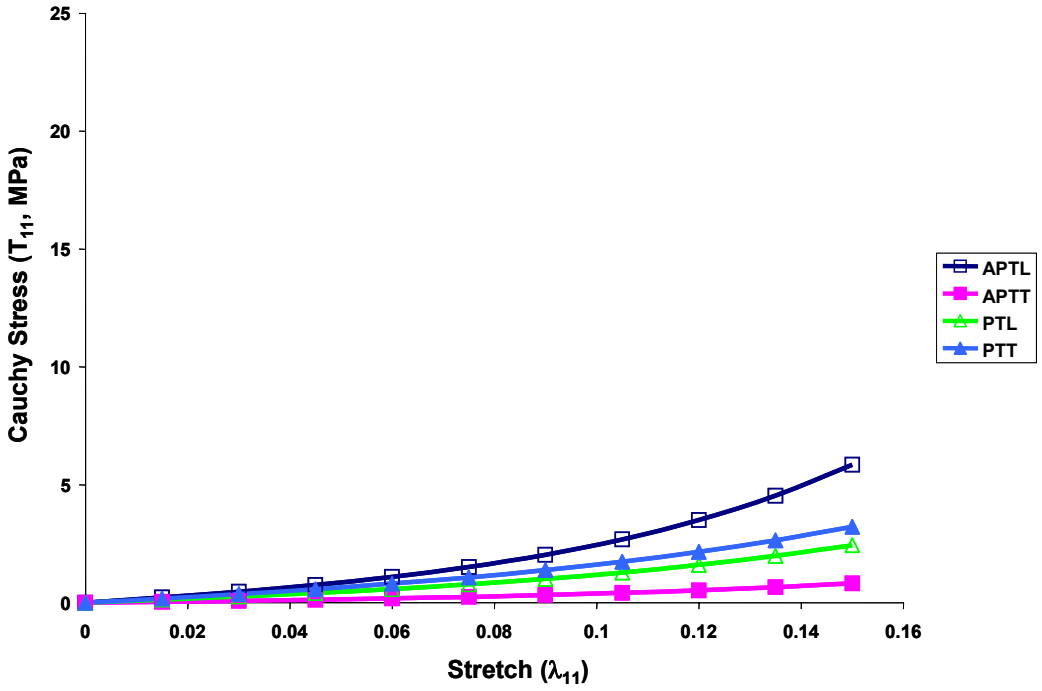

Figure 4.57: Stress-stretch curves for pure tension of specimen ID: 05-08016R

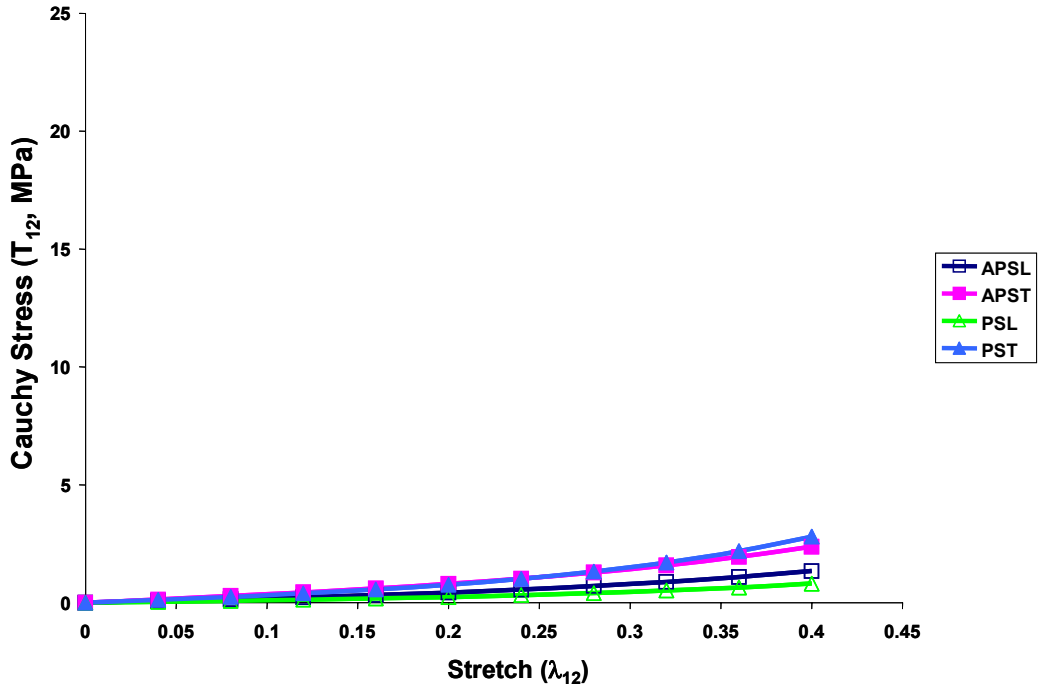

Figure 4.58: Stress-stretch curves for simple finite shear of specimen ID: 05-08016R

Table 4.17: Stress-stretch data for specimen ID: 05-10043R

Shear					Tensile				
stretch	stress (MPa)				stress (MPa)				stretch
	APSL	APST	PSL	PST	APTL	APTT	PTL	PTT	
0.00	0.00	0.00	0.00	0.00	0.00	0.00	0.00	0.00	0.00
0.04	0.06	0.03	0.04	0.05	0.07	0.08	0.03	0.10	0.02
0.08	0.12	0.06	0.09	0.11	0.15	0.16	0.06	0.22	0.03
0.12	0.21	0.10	0.15	0.17	0.24	0.26	0.11	0.34	0.05
0.16	0.33	0.15	0.23	0.26	0.36	0.36	0.17	0.48	0.06
0.20	0.50	0.24	0.34	0.38	0.50	0.49	0.25	0.64	0.08
0.24	0.75	0.37	0.49	0.54	0.69	0.65	0.37	0.82	0.09
0.28	1.12	0.56	0.71	0.76	0.94	0.84	0.55	1.04	0.11
0.32	1.67	0.85	1.02	1.06	1.25	1.07	0.80	1.30	0.12
0.36	2.48	1.31	1.48	1.48	1.67	1.35	1.17	1.60	0.14
0.40	3.72	2.02	2.14	2.08	2.21	1.69	1.70	1.96	0.15

max diff	1.70	0.06	0.53	0.50
avg diff	0.48	0.03	0.11	0.30
correlation	1.000	0.999	0.996	0.970

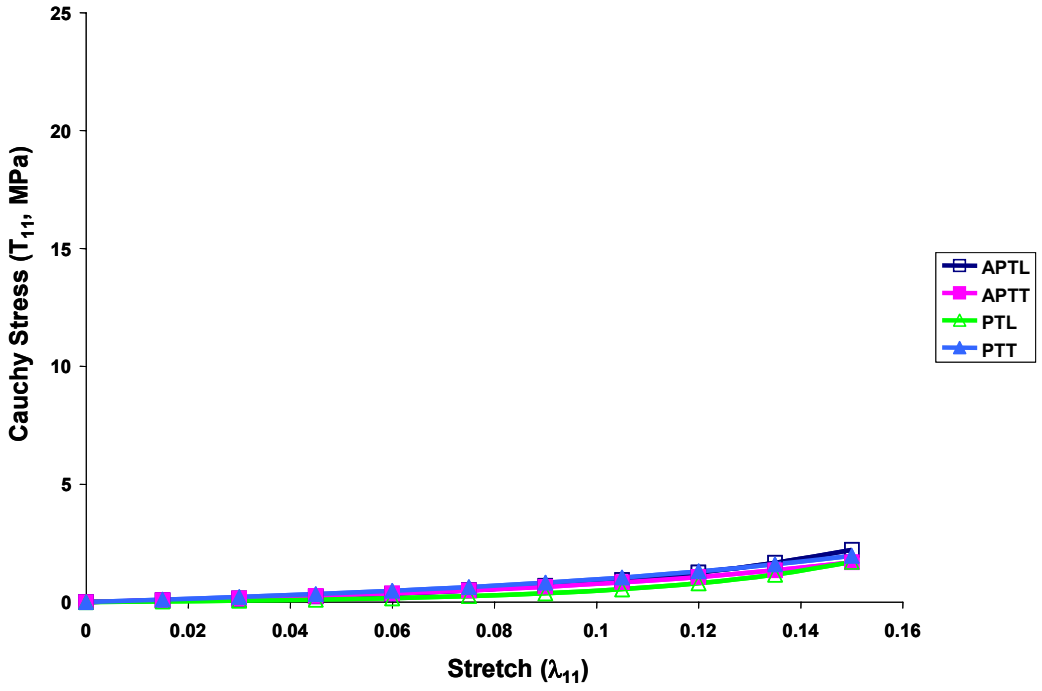

Figure 4.59: Stress-stretch curves for pure tension of specimen ID: 05-10043R

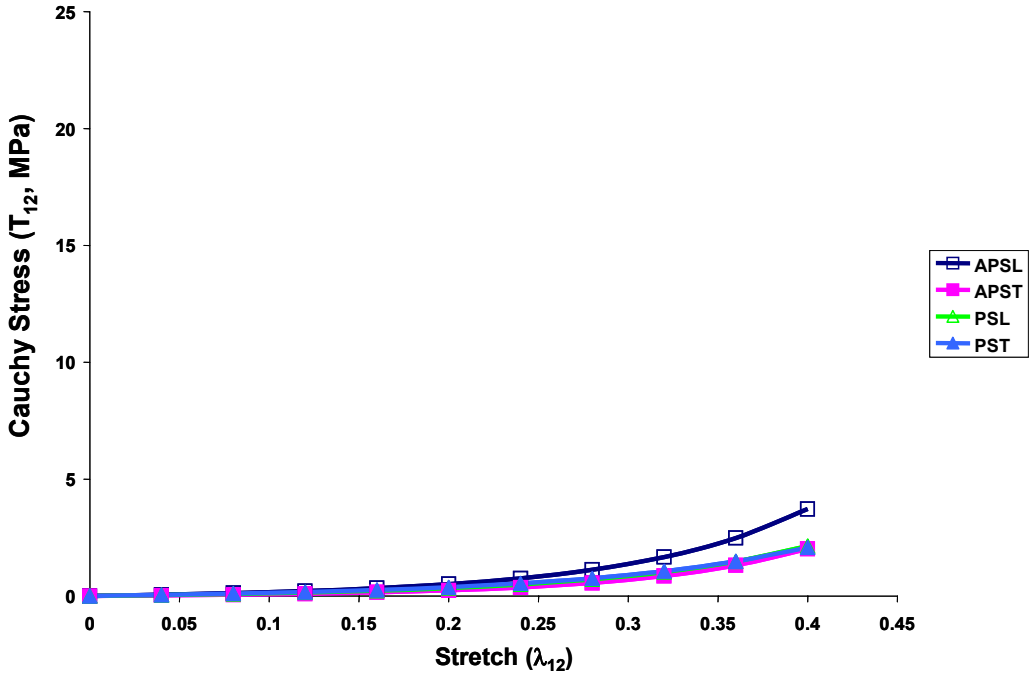

Figure 4.60: Stress-stretch curves for simple finite shear of specimen ID: 05-10043R

Table 4.18: Stress-stretch data for specimen ID: 05-11007R

Shear					Tensile				
stretch	stress (MPa)				stress (MPa)				stretch
	APSL	APST	PSL	PST	APTL	APTT	PTL	PTT	
0.00	0.00	0.00	0.00	0.00	0.00	0.00	0.00	0.00	0.00
0.04	0.07	0.06	0.06	0.12	0.10	0.07	0.25	0.09	0.02
0.08	0.15	0.13	0.12	0.27	0.21	0.16	0.53	0.19	0.03
0.12	0.24	0.21	0.21	0.46	0.32	0.25	0.87	0.30	0.05
0.16	0.34	0.31	0.34	0.75	0.46	0.37	1.28	0.43	0.06
0.20	0.47	0.43	0.54	1.17	0.61	0.52	1.82	0.57	0.08
0.24	0.63	0.57	0.83	1.81	0.79	0.71	2.50	0.73	0.09
0.28	0.83	0.76	1.29	2.79	1.00	0.94	3.39	0.92	0.11
0.32	1.09	1.00	1.99	4.31	1.25	1.24	4.55	1.14	0.12
0.36	1.42	1.32	3.10	6.69	1.55	1.63	6.07	1.41	0.14
0.40	1.85	1.72	4.88	10.49	1.90	2.13	8.06	1.71	0.15

max diff	0.13	5.61	0.23	6.35
avg diff	0.05	1.41	0.07	1.98
correlation	1.000	1.000	0.995	0.991

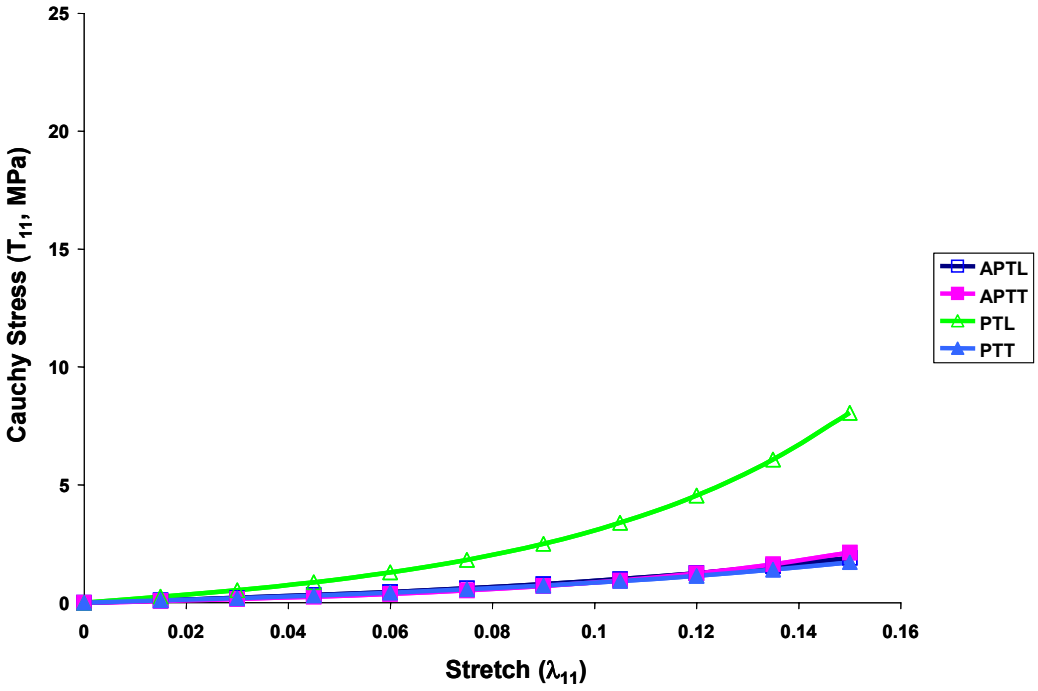

Figure 4.61: Stress-stretch curves for pure tension of specimen ID: 05-11007R

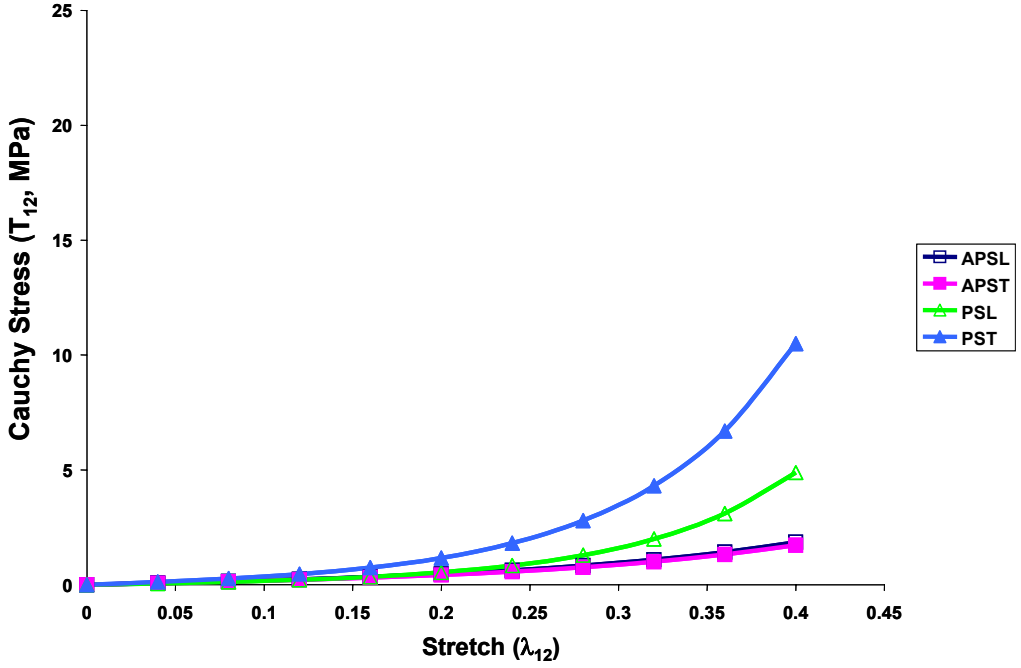

Figure 4.62: Stress-stretch curves for simple finite shear of specimen ID: 05-11007R

Table 4.19: Stress-stretch data for specimen ID: 05-08038L

Shear					Tensile				
stretch	stress (MPa)				stress (MPa)				stretch
	APSL	APST	PSL	PST	APTL	APTT	PTL	PTT	
0.00	0.00	0.00	0.00	0.00	0.00	0.00	0.00	0.00	0.00
0.04	0.03	0.06	0.08	0.04	0.08	0.04	0.25	0.21	0.02
0.08	0.06	0.14	0.16	0.10	0.16	0.09	0.53	0.43	0.03
0.12	0.10	0.22	0.28	0.19	0.27	0.15	0.84	0.68	0.05
0.16	0.15	0.33	0.45	0.32	0.41	0.21	1.22	0.97	0.06
0.20	0.23	0.47	0.70	0.55	0.59	0.29	1.69	1.31	0.08
0.24	0.36	0.67	1.06	0.94	0.83	0.39	2.27	1.72	0.09
0.28	0.54	0.93	1.62	1.61	1.15	0.50	2.99	2.20	0.11
0.32	0.81	1.29	2.46	2.78	1.59	0.65	3.89	2.78	0.12
0.36	1.24	1.78	3.76	4.89	2.18	0.83	5.03	3.49	0.14
0.40	1.89	2.47	5.79	8.82	2.98	1.05	6.47	4.34	0.15
max diff	0.58		3.03		1.93		2.13		
avg diff	0.27		0.46		0.55		0.64		
correlation	0.994		0.992		0.994		0.999		

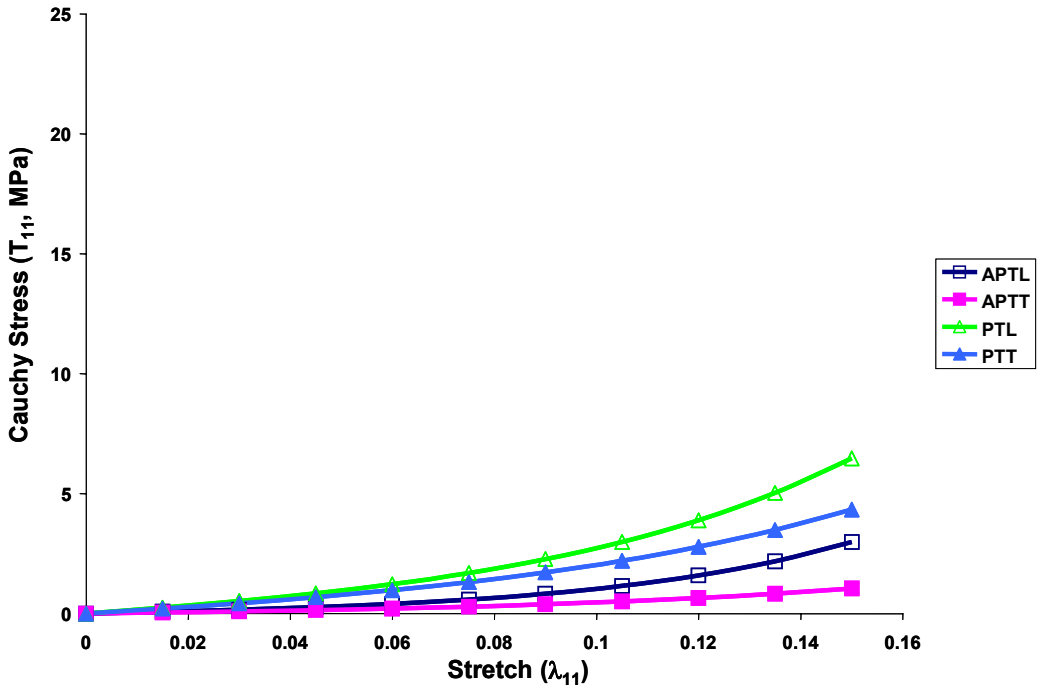

Figure 4.63: Stress-stretch curves for pure tension of specimen ID: 05-08038L

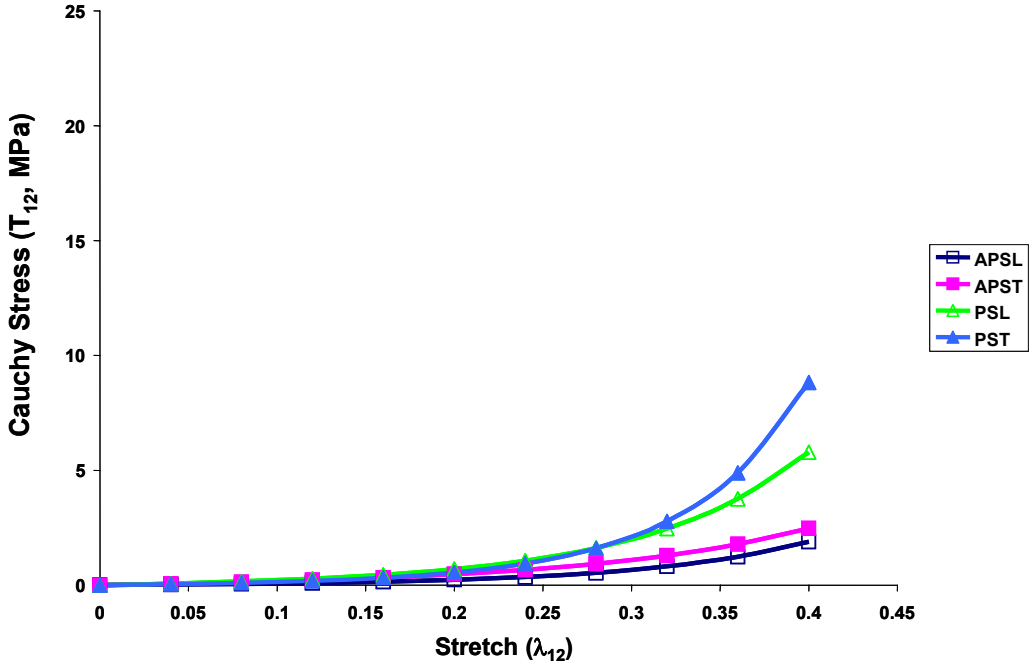

Figure 4.64: Stress-stretch curves for simple finite shear of specimen ID: 05-08038L

Table 4.20: Stress-stretch data for specimen ID: 05-08022L

Shear					Tensile				
stretch	stress (MPa)				stress (MPa)				stretch
	APSL	APST	PSL	PST	APTL	APTT	PTL	PTT	
0.00	0.00	0.00	0.00	0.00	0.00	0.00	0.00	0.00	0.00
0.04	0.03	0.05	0.03	0.06	0.11	0.06	0.10	0.06	0.02
0.08	0.06	0.11	0.07	0.13	0.24	0.13	0.21	0.13	0.03
0.12	0.10	0.18	0.12	0.23	0.38	0.20	0.34	0.20	0.05
0.16	0.16	0.27	0.18	0.36	0.55	0.29	0.50	0.29	0.06
0.20	0.25	0.39	0.25	0.56	0.76	0.40	0.70	0.38	0.08
0.24	0.39	0.54	0.35	0.84	1.00	0.54	0.94	0.50	0.09
0.28	0.60	0.75	0.49	1.26	1.31	0.70	1.26	0.64	0.11
0.32	0.93	1.03	0.67	1.89	1.69	0.91	1.66	0.80	0.12
0.36	1.44	1.41	0.92	2.85	2.15	1.18	2.18	1.00	0.14
0.40	2.27	1.93	1.26	4.31	2.73	1.51	2.84	1.24	0.15

max diff	0.34	3.05	1.22	1.59
avg diff	0.11	0.74	0.46	0.50
correlation	0.989	0.994	1.000	0.997

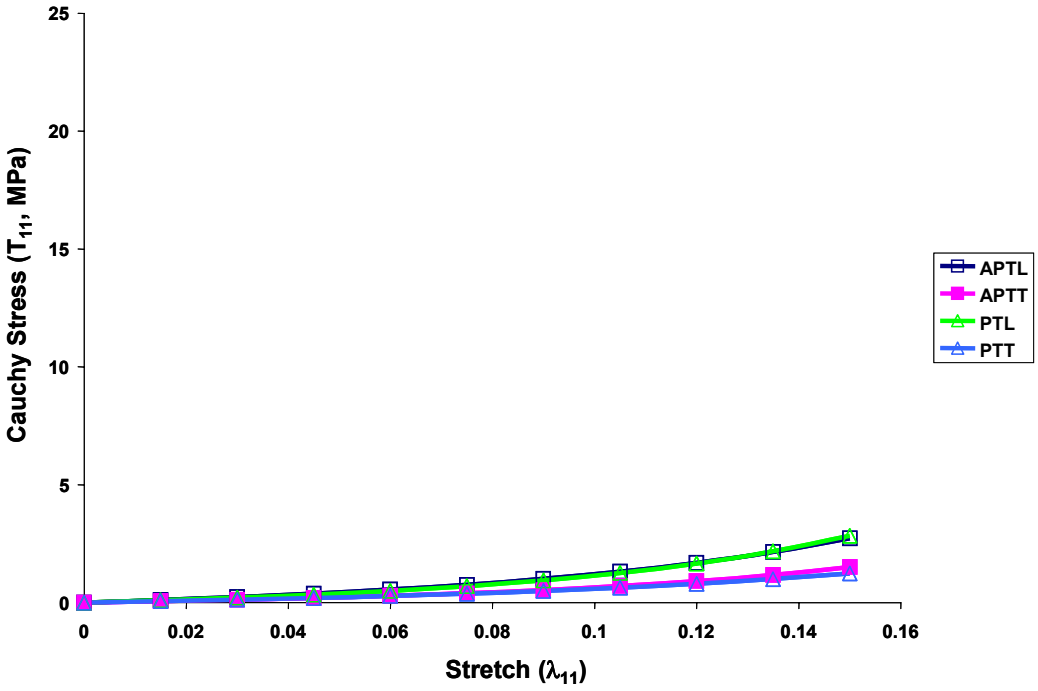

Figure 4.65: Stress-stretch curves for pure tension of specimen ID: 05-08022L

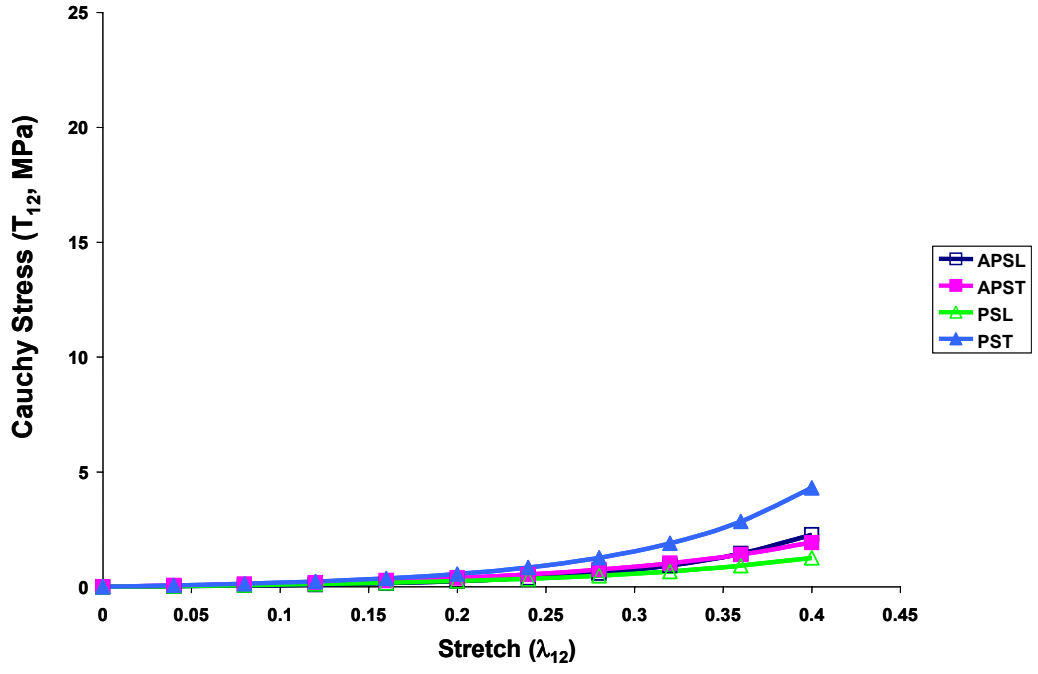

Figure 4.66: Stress-stretch curves for simple finite shear of specimen ID: 05-08022L

Table 4.21: Stress-stretch data for specimen ID: 05-08013L

Shear					Tensile				
stretch	stress (MPa)				stress (MPa)				stretch
	APSL	APST	PSL	PST	APTL	APTT	PTL	PTT	
0.00	0.00	0.00	0.00	0.00	0.00	0.00	0.00	0.00	0.00
0.04	0.02	0.05	0.07	0.05	0.08	0.02	0.12	0.17	0.02
0.08	0.05	0.12	0.15	0.11	0.16	0.05	0.26	0.36	0.03
0.12	0.09	0.21	0.24	0.20	0.27	0.08	0.41	0.57	0.05
0.16	0.14	0.34	0.36	0.34	0.40	0.12	0.59	0.81	0.06
0.20	0.23	0.55	0.52	0.55	0.57	0.16	0.81	1.10	0.08
0.24	0.36	0.87	0.74	0.89	0.80	0.22	1.07	1.45	0.09
0.28	0.56	1.39	1.04	1.44	1.10	0.28	1.40	1.86	0.11
0.32	0.89	2.22	1.45	2.35	1.50	0.37	1.80	2.37	0.12
0.36	1.42	3.58	2.01	3.86	2.04	0.47	2.30	2.98	0.14
0.40	2.29	5.85	2.80	6.45	2.75	0.60	2.91	3.73	0.15

max diff	3.57	3.65	2.15	0.81
avg diff	0.83	0.65	0.66	0.34
correlation	1.000	0.984	0.996	1.000

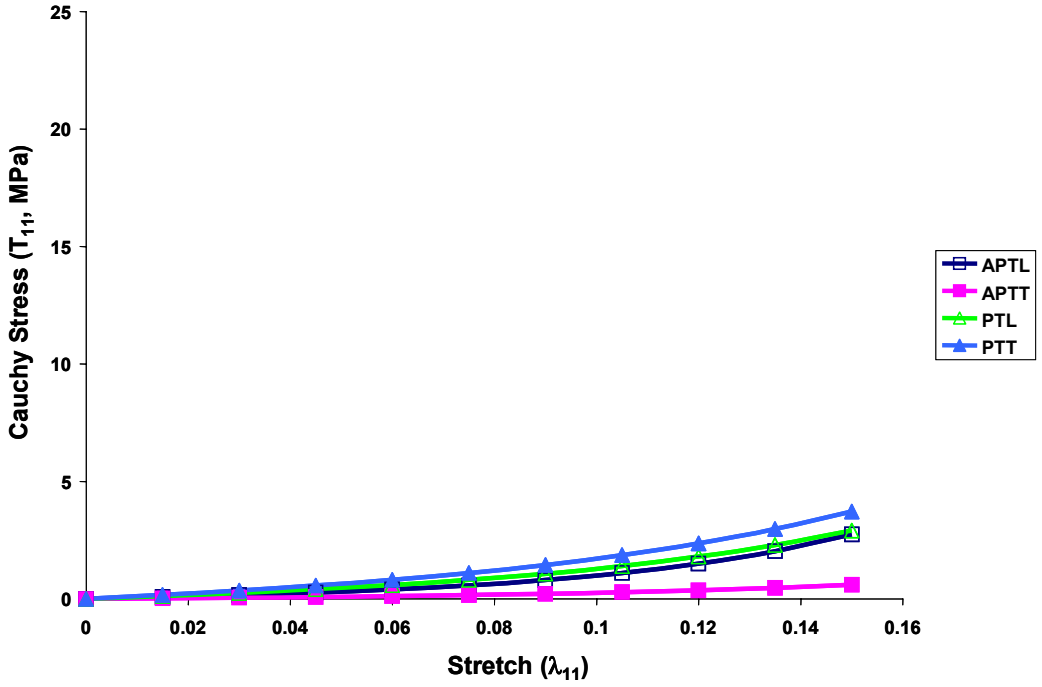

Figure 4.67: Stress-stretch curves for pure tension of specimen ID: 05-08013R

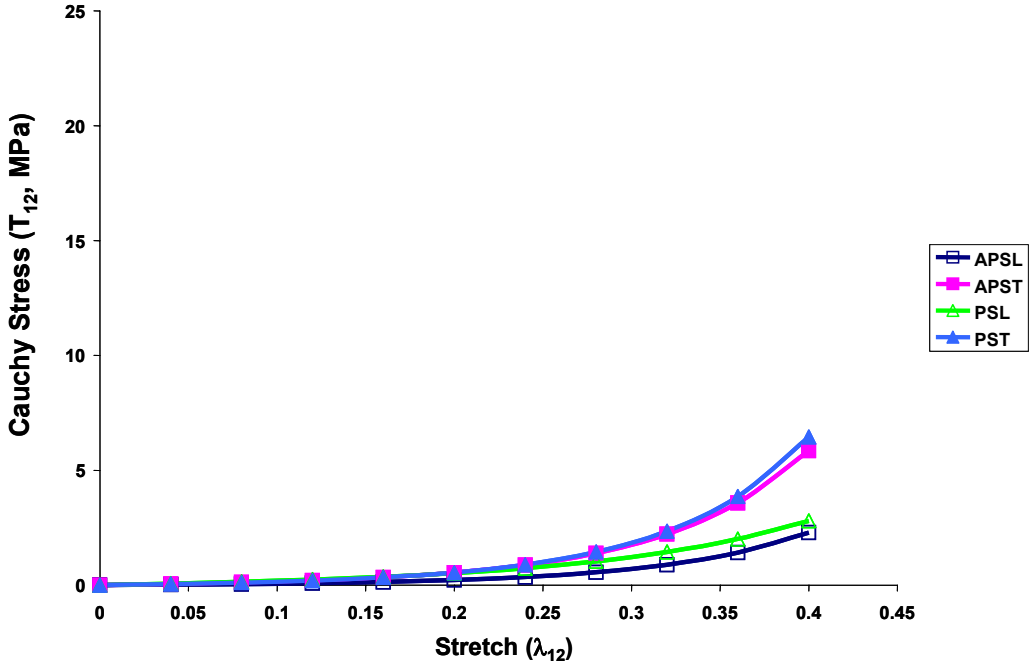

Figure 4.68: Stress-stretch curves for simple finite shear of specimen ID: 05-08013R

Table 4.22: Stress-stretch data for specimen ID: 05-08041R

Shear					Tensile				
stretch	stress (MPa)				stress (MPa)				stretch
	APSL	APST	PSL	PST	APTL	APTT	PTL	PTT	
0.00	0.00	0.00	0.00	0.00	0.00	0.00	0.00	0.00	0.00
0.04	0.04	0.21	0.04	0.04	0.12	0.05	0.10	0.07	0.02
0.08	0.08	0.44	0.10	0.09	0.25	0.11	0.21	0.15	0.03
0.12	0.14	0.73	0.17	0.17	0.41	0.17	0.35	0.24	0.05
0.16	0.23	1.11	0.28	0.30	0.60	0.25	0.52	0.35	0.06
0.20	0.35	1.62	0.45	0.52	0.85	0.34	0.73	0.49	0.08
0.24	0.54	2.31	0.72	0.92	1.17	0.45	1.01	0.67	0.09
0.28	0.82	3.28	1.15	1.63	1.58	0.59	1.38	0.89	0.11
0.32	1.24	4.64	1.85	2.94	2.12	0.76	1.85	1.18	0.12
0.36	1.90	6.55	3.00	5.43	2.83	0.98	2.47	1.55	0.14
0.40	2.92	9.26	4.93	10.33	3.75	1.24	3.30	2.02	0.15

max diff	6.35	5.40	2.50	1.28
avg diff	1.99	0.88	0.79	0.39
correlation	0.996	0.994	0.998	1.000

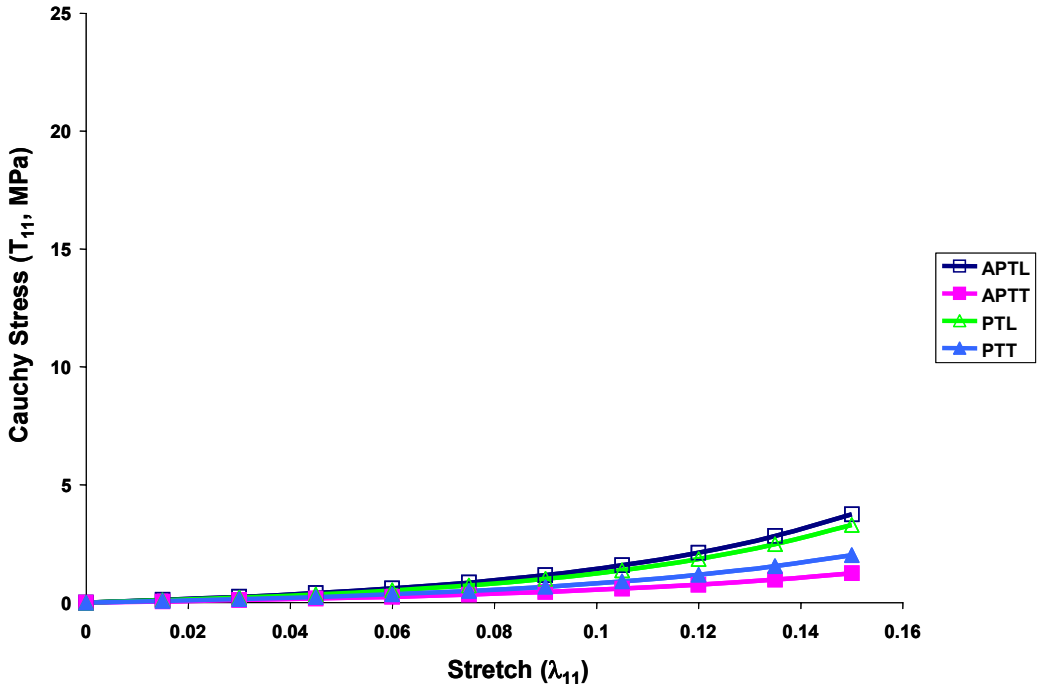

Figure 4.69: Stress-stretch curves for pure tension of specimen ID: 05-08041R

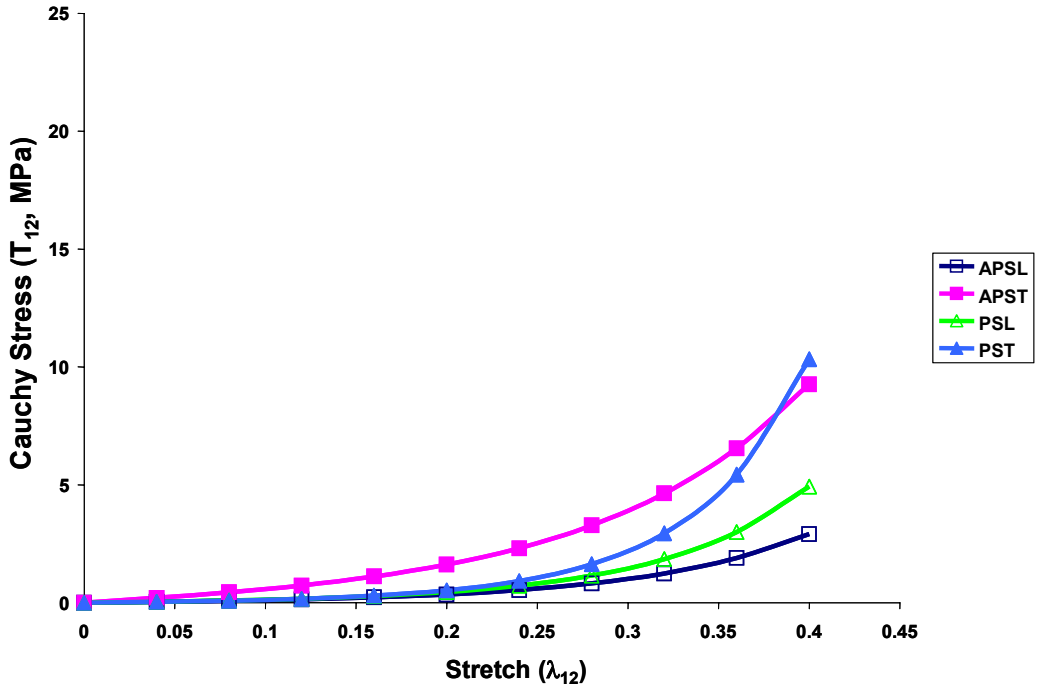

Figure 4.70: Stress-stretch curves for simple finite shear of specimen ID: 05-08041R

Table 4.23: Stress-stretch data for specimen ID: 05-08048L

Shear					Tensile				
stretch	stress (MPa)				stress (MPa)				stretch
	APSL	APST	PSL	PST	APTL	APTT	PTL	PTT	
0.00	0.00	0.00	0.00	0.00	0.00	0.00	0.00	0.00	0.00
0.04	0.09	0.09	0.05	0.32	0.11	0.11	0.14	0.73	0.02
0.08	0.18	0.19	0.10	0.70	0.24	0.24	0.29	1.56	0.03
0.12	0.29	0.33	0.17	1.18	0.40	0.41	0.45	2.53	0.05
0.16	0.40	0.51	0.27	1.83	0.61	0.62	0.65	3.75	0.06
0.20	0.53	0.76	0.40	2.76	0.91	0.92	0.89	5.29	0.08
0.24	0.68	1.13	0.58	4.09	1.32	1.32	1.18	7.27	0.09
0.28	0.85	1.66	0.84	6.02	1.89	1.89	1.54	9.84	0.11
0.32	1.06	2.44	1.22	8.85	2.68	2.67	1.98	13.17	0.12
0.36	1.31	3.59	1.77	13.02	3.80	3.76	2.52	17.52	0.14
0.40	1.61	5.31	2.57	19.26	5.38	5.29	3.19	23.21	0.15
max diff	3.70		16.69		0.08		20.03		
avg diff	0.82		4.55		0.02		6.55		
correlation	0.968		1.000		1.000		0.998		

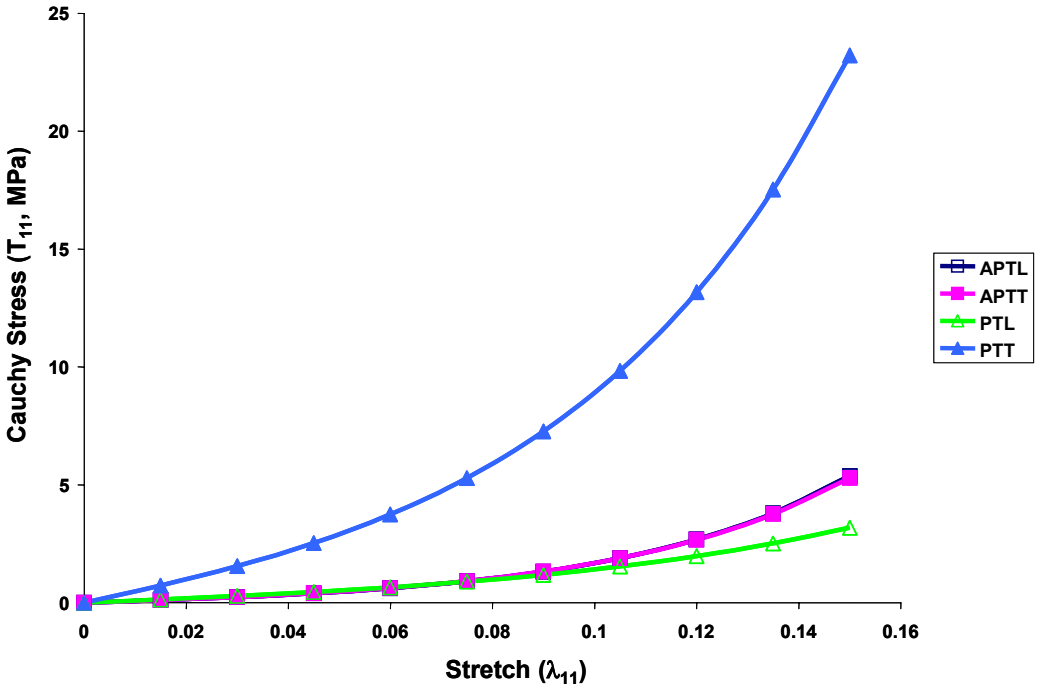

Figure 4.71: Stress-stretch curves for pure tension of specimen ID: 05-08048L

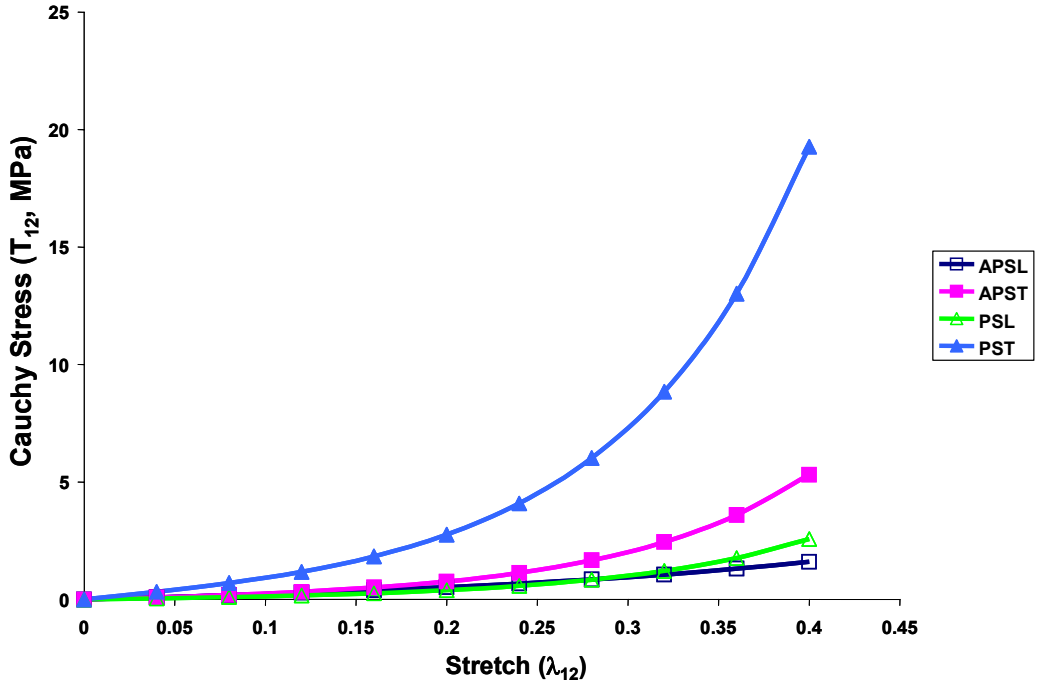

Figure 4.72: Stress-stretch curves for simple finite shear of specimen ID: 05-08048L

Table 4.24: Stress-stretch data for specimen ID: 05-10071R

Shear					Tensile				
stretch	stress (MPa)				stress (MPa)				stretch
	APSL	APST	PSL	PST	APTL	APTT	PTL	PTT	
0.00	0.00	0.00	0.00	0.00	0.00	0.00	0.00	0.00	0.00
0.04	0.01	0.03	0.09	0.05	0.05	0.04	0.40	0.09	0.02
0.08	0.03	0.07	0.18	0.11	0.10	0.09	0.84	0.19	0.03
0.12	0.04	0.11	0.27	0.16	0.16	0.15	1.33	0.30	0.05
0.16	0.06	0.16	0.37	0.23	0.25	0.22	1.89	0.43	0.06
0.20	0.09	0.22	0.48	0.31	0.36	0.31	2.57	0.60	0.08
0.24	0.11	0.30	0.60	0.41	0.51	0.43	3.37	0.80	0.09
0.28	0.15	0.40	0.73	0.53	0.72	0.57	4.34	1.05	0.11
0.32	0.20	0.53	0.87	0.67	1.00	0.76	5.52	1.36	0.12
0.36	0.26	0.70	1.04	0.85	1.39	1.01	6.96	1.75	0.14
0.40	0.34	0.92	1.23	1.07	1.92	1.33	8.71	2.23	0.15

max diff	0.58	0.20	0.60	6.47
avg diff	0.19	0.13	0.14	2.47
correlation	1.000	0.993	0.998	0.999

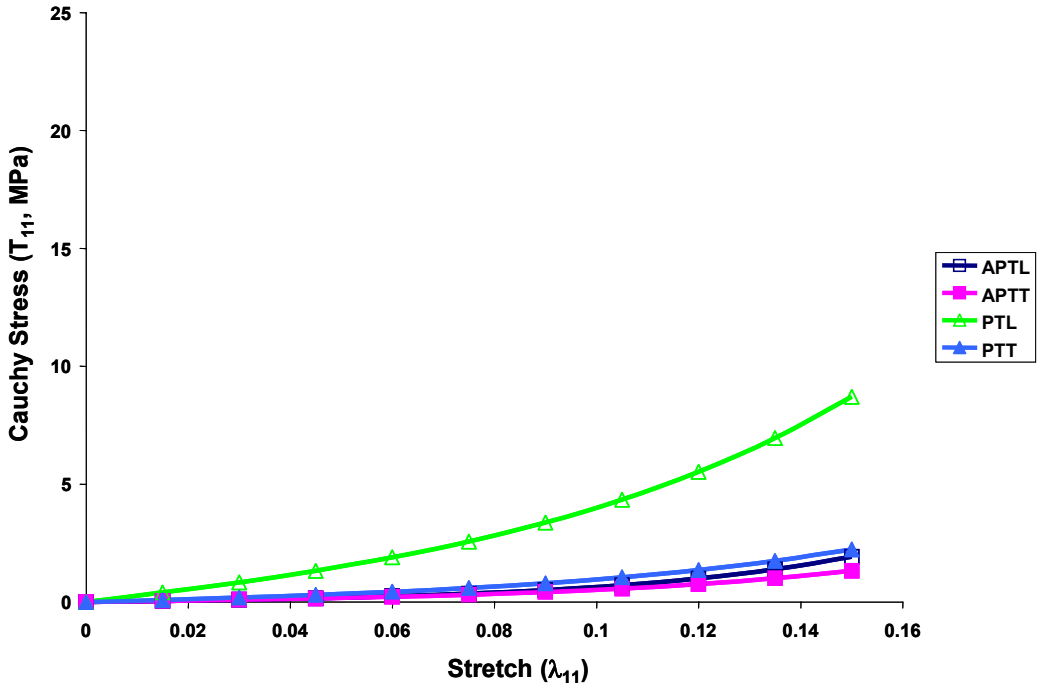

Figure 4.73: Stress-stretch curves for pure tension of specimen ID: 05-10071R

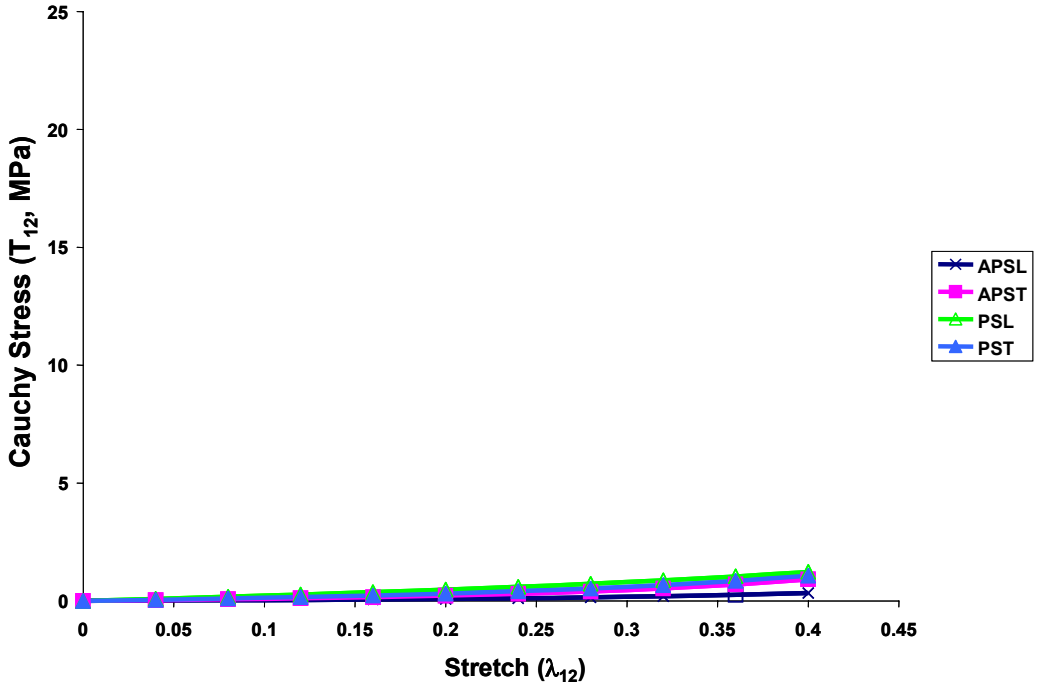

Figure 4.74: Stress-stretch curves for simple finite of specimen ID: 05-10071R

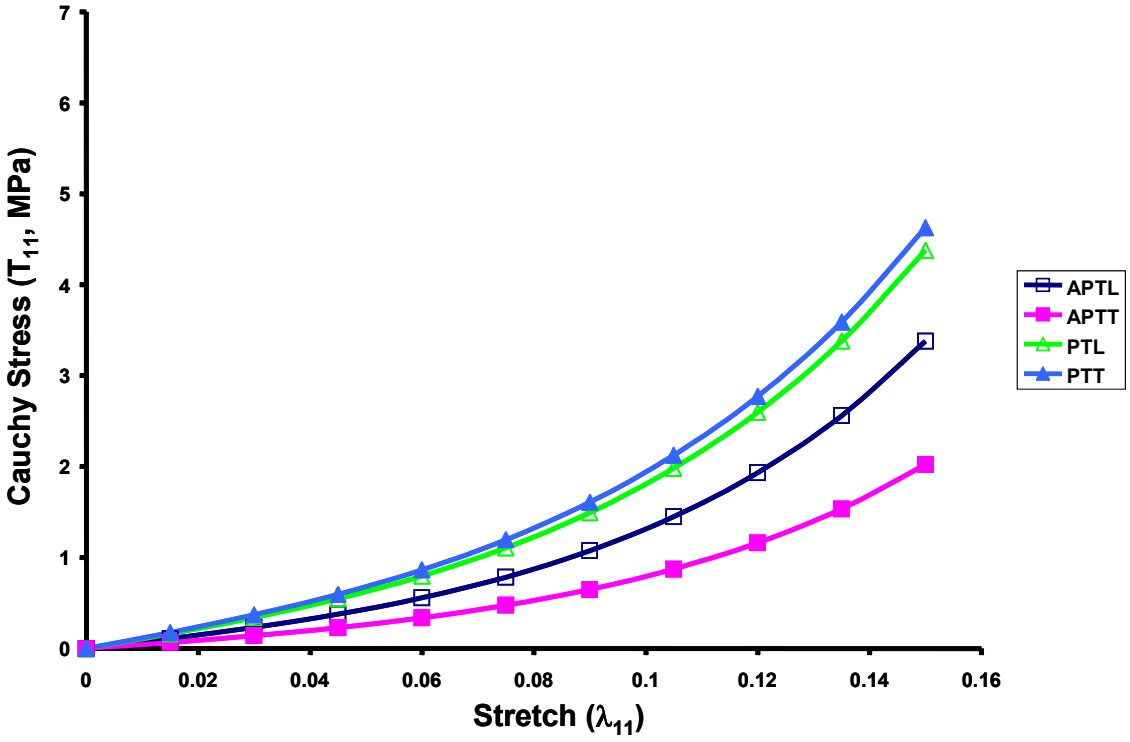

Figure 4.75: Average stress-stretch curves for pure tension

Table 4.25: Average stress-stretch data for pure tension

stretch	APTL	APTT	PTL	PTT
0	0	0	0	0
0.015	0.11	0.07	0.16	0.18
0.03	0.23	0.14	0.34	0.37
0.045	0.38	0.23	0.55	0.60
0.06	0.56	0.34	0.80	0.87
0.075	0.79	0.48	1.11	1.20
0.09	1.08	0.65	1.49	1.61
0.105	1.45	0.87	1.98	2.12
0.12	1.93	1.16	2.60	2.77
0.135	2.56	1.54	3.38	3.59
0.15	3.38	2.02	4.38	4.63
max diff	1.36		0.25	
avg diff	0.45		0.10	
correl	1.000		1.000	

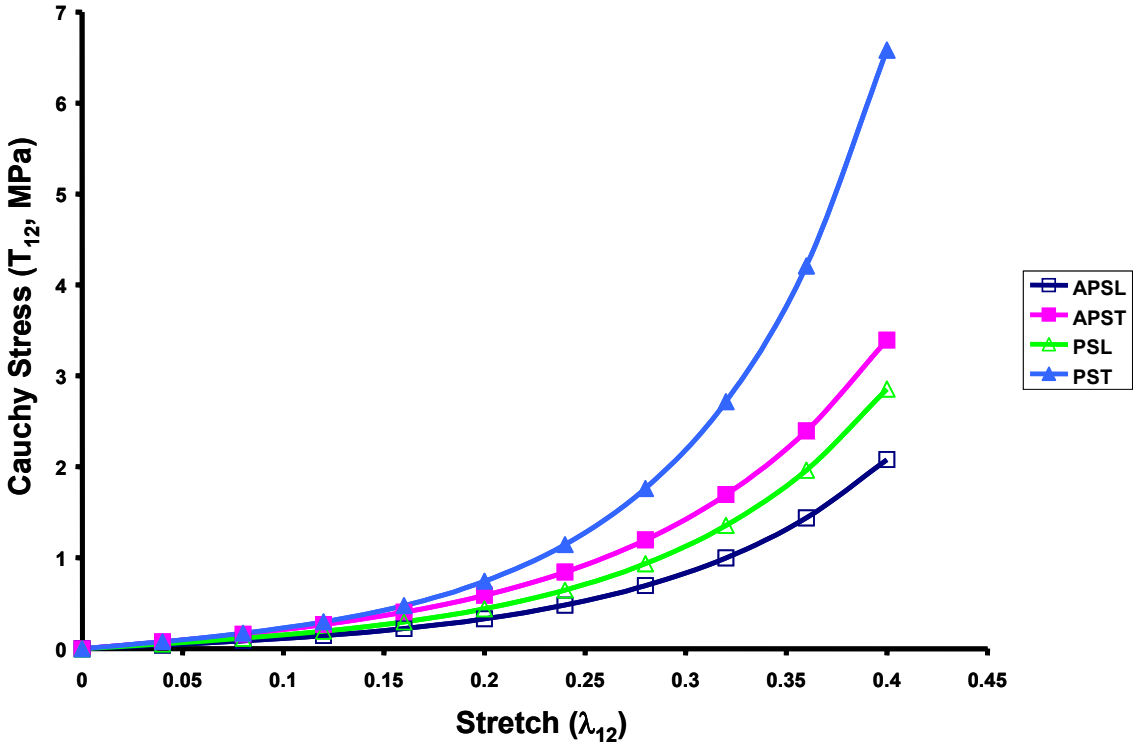

Figure 4.76: Average stress-stretch curves for simple finite shear

Table 4.26: Average stress-stretch data for simple finite shear

stretch	APSL	APST	PSL	PST
0	0	0	0	0
0.04	0.04	0.08	0.05	0.08
0.08	0.09	0.16	0.12	0.17
0.12	0.14	0.27	0.19	0.29
0.16	0.22	0.40	0.30	0.47
0.2	0.33	0.59	0.44	0.74
0.24	0.48	0.84	0.65	1.15
0.28	0.69	1.20	0.94	1.76
0.32	1.00	1.69	1.36	2.72
0.36	1.44	2.39	1.96	4.21
0.4	2.08	3.39	2.85	6.58
max diff	1.31		3.73	
avg diff	0.41		0.85	
correl	1.000		0.997	

4.3.2.3 Average coefficients for each loading condition

The C_1 and C_2 coefficients for the averaged stress-stretch curves of pure tension of the axillary pouch in the longitudinal direction were 0.21 MPa and 11.3, respectively. (Table 4.27) The average C_1 and C_2 coefficients for pure tension in the transverse direction were 0.13 MPa and 11.1, respectively. The average C_1 and C_2 coefficients for simple finite shear of the axillary pouch were 0.14 MPa and 7.1, respectively for the longitudinal direction, and 0.29 MPa and 6.4, respectively for the transverse direction. The average coefficients for the posterior capsule showed a trend of being more similar across all loading configurations, with the C_1 and C_2 coefficients being 0.36 MPa and 9.7 for pure tension in the longitudinal direction and 0.41 MPa and 9.3 for pure tension in the transverse direction. The average C_1 and C_2 coefficients for simple finite shear were 0.18 MPa and 7.3 for the longitudinal direction and 0.19 MPa and 9.9 for the transverse direction. Based on the sensitivity of the curves to the constitutive coefficients

(Section 4.2.3.3), the differences between the longitudinal and transverse directions, as well as between the axillary pouch and posterior regions are considered to be minimal since the difference in C_1 is less than 0.3 MPa and the difference in C_2 is less than 3.

When comparing the different loading directions for pure tension and finite simple shear, the lowest correlation coefficient was shown for the simple finite shear of the posterior region, at 0.997. The correlation coefficients for all other loading conditions were 1.000. The stress-stretch curves for pure tension and simple finite shear are shown in Figure 4.75 and Figure 4.76, respectively.

Table 4.27: Constitutive coefficients for average stress-stretch curves

	C1 (MPa)	C2
APSL	0.14	7.1
APST	0.29	6.4
APTL	0.21	11.3
APTT	0.13	11.1
ASTL	0.08	21.0
PSL	0.18	7.3
PST	0.19	9.9
PTL	0.36	9.7
PTT	0.41	9.3

5.0 DISCUSSION

The axillary pouch and posterior regions of the glenohumeral capsule have been characterized using a combined experimental and computational methodology. A hyperelastic isotropic constitutive model was used to model the tissues response to tensile and shear loading conditions in two perpendicular directions. No differences were found when comparing the coefficients of the constitutive model between loading directions for both tensile and shear loading conditions. In addition, no difference was found when comparing the coefficients between the axillary pouch and posterior region.

5.1 IMPLICATIONS OF FINDINGS

5.1.1 Engineering

The data presented in the current work have many implications for experimental and computational analyses, thus having relevance for the field of Bioengineering. Based on the fact that no differences could be found when comparing the constitutive coefficients or stresses between two perpendicular loading directions, an isotropic constitutive model should be used when creating finite element models of the glenohumeral capsule, rather than a transverse isotropic model which has been used for many other ligaments in the body. In addition, because

no differences could be found when comparing the constitutive coefficients and stresses of the axillary pouch to the posterior region, both these regions of the capsule can be modeled using the same constitutive model and constitutive coefficients.

The data obtained in the current work also have implications for studies that determine the mechanical or structural properties of different regions of the capsule at failure by isolating them into ligamentous regions with a high aspect ratio. To determine the biomechanical properties at failure, a uniform stress distribution across the cross-section is assumed. However, this may not be a valid assumption when the glenohumeral capsule is isolated into capsuloligamentous regions. To allow for the complex stress and strain distributions observed during loading of the capsule, the glenohumeral capsule may be highly heterogenous. Thus, a uniform stress distribution may not be possible.

The current work clearly suggests that the glenohumeral capsule should be evaluated as an isotropic sheet of fibrous tissue, rather than uniaxial ligamentous regions. However, experimentally evaluating the glenohumeral capsule as a sheet of fibrous tissue poses many experimental difficulties. Despite these difficulties, a thorough understanding as to the function of the glenohumeral capsule is necessary to improve patient outcomes. Thus, there exists a need to continue to develop and validate constitutive coefficients to determine if an average set of coefficients can be used to model groups of the population, i.e. male versus female. These validated coefficients can then be used to develop finite element models that should be utilized to evaluate the mechanisms by which the capsuloligamentous regions transmit loads at various joint positions to provide joint stability.

5.1.2 Clinical

In addition to engineering relevance, the results presented in the current work also have clinical relevance. Currently surgeons use a plicate and shift method to repair injuries to the glenohumeral capsule, whereby they create incisions in both the inferior-superior and medial-lateral directions, and then shift the leaflets across one another. The current work has shown that the axillary pouch is thicker than the posterior regions of the capsule, yet has similar mechanical properties suggesting that the axillary pouch experiences greater loads *in-vivo*. Therefore, when an injury occurs to the axillary pouch, the uninjured posterior region may be shifted inferiorly to help stabilize the joint, or if the posterior region is injured, the axillary pouch may be shifted superiorly to help maintain joint stability.

This theory could also be investigated via multiple validated finite element models whereby the obtained constitutive coefficients can be utilized, and the stress and strain distribution within the glenohumeral capsule could be determined. The stress distributions would provide a means for identifying locations within the glenohumeral capsule that are at risk for injury and could be assessed for various joint positions. Moreover, the constitutive coefficients could be altered, simulating diminishing mechanical properties of the different regions due to aging and gender, disease, or surgical repair procedures, such as thermocapsular shrinkage. [75, 76] Thus, utilizing these models to simulate the normal, injured, and repaired state, would provide scientific rationale to improve clinical exams for diagnosis and surgical planning, surgical repair techniques, and would enhance our understanding of normal function.

5.2 ADVANCEMENTS AND LIMITATIONS

5.2.1 Advancements

In the current work, a comprehensive analysis was performed in which experimental and computational methodologies to characterize the glenohumeral capsule were developed. Previously, mechanical testing of the glenohumeral capsule has been performed by isolating the capsule into ligamentous regions and then applying a tensile load in the direction parallel to their longitudinal axes. [3, 6, 21, 22, 24] However, in the current work, the mechanical response of the two regions, evaluated as a sheet of tissue rather than a ligament, were assessed bi-directionally under the application of both tensile and shear loading conditions, which more accurately describe the loading that the capsule experiences as it wraps around the humeral head during internal and external rotation.

In addition to experimental advancements, this work has demonstrated clear computational advancements as well. The constitutive coefficients obtained from the current work can be expanded by performing additional tests on more specimens to determine what effect of age on the mechanical properties of the glenohumeral capsule. These coefficients are novel and can be used in conjunction with finite element methods to create a powerful tool to improve our overall knowledge of the function of the glenohumeral joint.

5.2.2 Limitations

Despite the clear advancement to the engineering and clinical field, there are several limitations that should be noted. Only the axillary pouch and posterior regions of the capsule were

evaluated in the current work. Although these regions seem to have the largest role in joint stability, contributions from surrounding regions should also be considered.

The assumption of hyperelasticity is implicit in the current constitutive framework. It was believed that hyperelasticity was an appropriate starting point for the current work that provided a framework for elucidating capsular mechanical function. To determine constitutive coefficients, data from the tenth cycle of loading was used to minimize viscoelastic effects, since little work has been performed to analyze the viscoelastic effects of the capsule. Thus the constitutive framework described in this work is appropriate given the input data.

The assumption of uncoupled deviatoric-dilatational response is commonly employed in finite deformation elasticity for slightly compressible materials [72, 74, 77] – it greatly decreases the complexity of the constitutive model and finite element implementation. This assumption is justified by the fact that the vast majority of strain energy induced in ligaments is deviatoric because volumetric confinement of the tissue in physiological loading scenarios is minimal.

Finally, the current constitutive model requires an update to correctly account for tensile and shear elongations. Currently, the coefficients between two perpendicular loading directions compare well, thus an isotropic model is appropriate, however the coefficients should also compare well between tensile and shear loading conditions. Therefore, further work is required to revamp the current constitutive model until it can model both tensile and shear loading conditions in the same manner.

5.3 COMPARISON TO LITERATURE

Because such a constitutive model has not been developed in the past for the glenohumeral capsule, a direct comparison of the coefficients to literature is difficult. Instead, the stresses generated using the optimized coefficients were compared to values reported in the literature. The magnitude of stress from the tensile loading configuration compare well to ultimate stresses previously found for the axillary pouch (5.5 MPa) [3] and the posterior capsule (7.9 MPa) [78], even though significantly different experimental protocols were utilized. Previously, dog-bone samples were excised from the tissue, cutting inter-fiber connections, and only tensile loading conditions were applied. The shear loading condition utilized in the current study provides new information regarding the mechanical properties of the capsular tissue, in that it has not been reported in the literature. Therefore, stresses from the shear loading configuration were not compared to literature.

5.4 SUMMARY

The anatomy of the glenohumeral capsule is extremely complex; thus, researchers have proposed using computational methods to evaluate its function. However, the correct constitutive model that describes the stress-strain relationship of the tissue of interest is imperative to predicting accurate stress and strain distributions in the tissue. Therefore, the objective of this work was to characterize sheets of tissue from two different regions of the glenohumeral capsule using a combined experimental and computational methodology. Both experimental and computational methodologies for the characterization of the glenohumeral capsule were developed. These methodologies were then used to determine the coefficients of a hyperelastic isotropic

constitutive model, and thus the stress-strain relationship of each tissue sample was determined. The axillary pouch and posterior capsule have been shown to behave like isotropic materials during both tensile and finite simple shear tests. However, due to the constitutive coefficients not comparing well between tensile and shear loading conditions, it is necessary to update the current constitutive model. The axillary pouch and posterior region have also been shown to have similar mechanical properties, despite the clear differences in geometry. The current work has developed a methodology to characterize soft tissues in which the appropriate constitutive model is unknown. This methodology can be expanded to develop subject-specific finite element models and ultimately improve our understanding of the function of the glenohumeral joint.

APPENDIX A

MATHCAD PROGRAM TO DETERMINE AVERAGE CONSTITUTIVE COEFFICIENTS

SHEAR LOADING CONDITION

$$T := \begin{pmatrix} 0 \\ 0.06 \\ 0.127 \\ 0.208 \\ 0.314 \\ 0.457 \\ 0.656 \\ 0.94 \\ 1.352 \\ 1.963 \\ 2.886 \end{pmatrix} \qquad \lambda := \begin{pmatrix} 0 \\ 0.04 \\ 0.08 \\ 0.12 \\ 0.16 \\ 0.2 \\ 0.24 \\ 0.28 \\ 0.32 \\ 0.36 \\ 0.4 \end{pmatrix}$$

$i := 1 .. 10$

$$Tfit(\lambda, c1, c2) := \overrightarrow{\left[\lambda \cdot c1 \cdot c2 \cdot \left(2 \cdot e^{c2 \cdot \lambda^2} - 1\right)\right]}$$

$$SSE(c1, c2) := \sum_i \left(T_i - Tfit(\lambda_i, c1, c2)\right)^2$$

$c1 := .1$

$c2 := 10$

Given

$SSE(c1, c2) = 0$

$c1 > 0$

$c2 > 0$

$$\begin{pmatrix} c1 \\ c2 \end{pmatrix} := Minerr(c1, c2)$$

$c1 = 0.183$

$c2 = 7.271$

$Tfit(\lambda, c1, c2) =$

	0
0	0
1	0.054
2	0.117
3	0.195
4	0.3
5	0.446
6	0.651
7	0.945
8	1.366
9	1.978
10	2.873

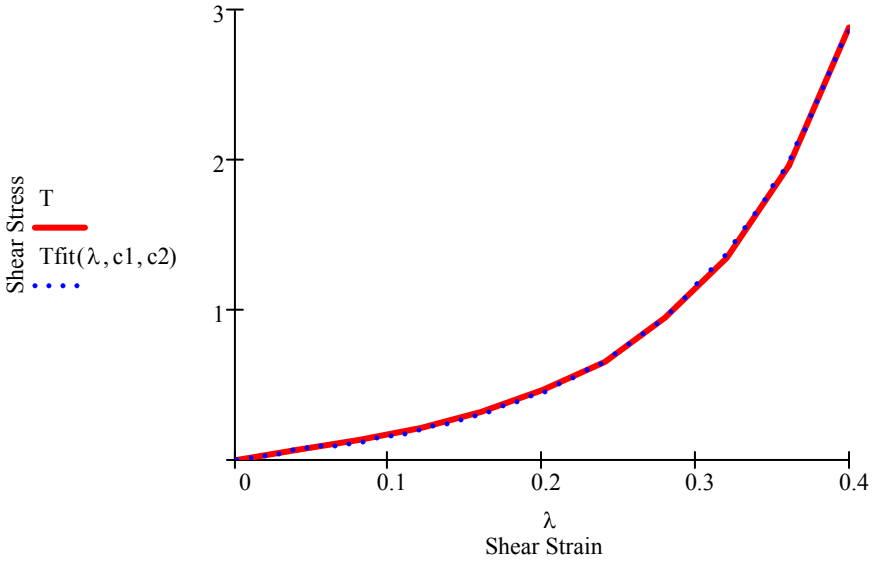

TENSILE LOADING CONDITIONS

$$T := \begin{pmatrix} 0 \\ 0.09 \\ 0.193 \\ 0.328 \\ 0.515 \\ 0.785 \\ 1.186 \\ 1.794 \\ 2.74 \\ 4.251 \\ 6.742 \end{pmatrix} \qquad \lambda := \begin{pmatrix} 0 \\ 0.04 \\ 0.08 \\ 0.12 \\ 0.16 \\ 0.2 \\ 0.24 \\ 0.28 \\ 0.32 \\ 0.36 \\ 0.4 \end{pmatrix}$$

$i := 1 .. 10$

$$Tfit(\lambda, c1, c2) := \overrightarrow{\left[\lambda \cdot c1 \cdot c2 \cdot \left(2 \cdot e^{c2 \cdot \lambda^2} - 1\right)\right]}$$

$$SSE(c1, c2) := \sum_i \left(T_i - Tfit(\lambda_i, c1, c2)\right)^2$$

$c1 := .1$

$c2 := 10$

Given

$SSE(c1, c2) = 0$

$c1 > 0$

$c2 > 0$

$$\begin{pmatrix} c1 \\ c2 \end{pmatrix} := Minerr(c1, c2)$$

$c1 = 0.193$

$c2 = 9.92$

$Tfit(\lambda, c1, c2) =$

	0
0	0
1	0.079
2	0.173
3	0.3
4	0.483
5	0.755
6	1.166
7	1.795
8	2.768
9	4.291
10	6.716

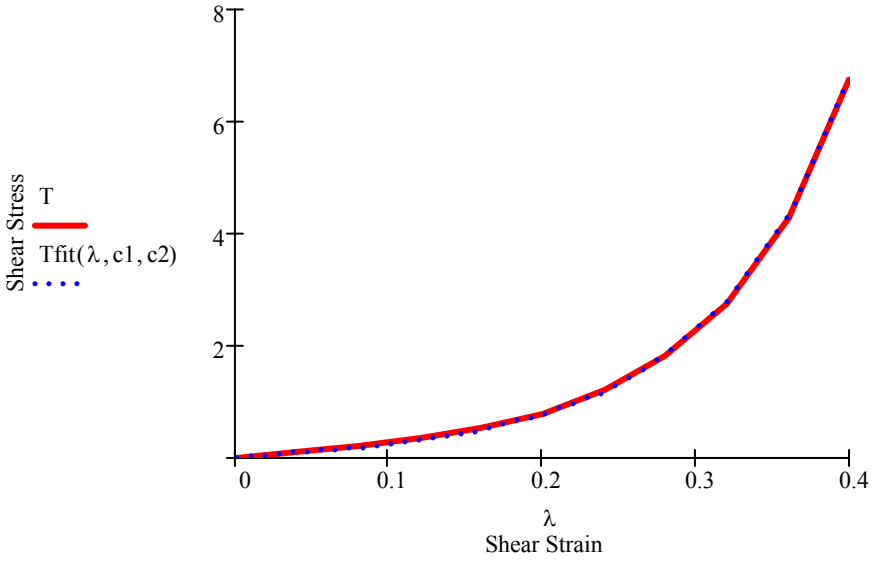

APPENDIX B

INPUT FILE FOR NIKE3D TO RUN FINITE ELEMENT SIMULATIONS

```
*-------------------------- CONTROL CARD #1 ---------------------------*

SpecimenID_Region_LoadingCondition
*
*-------------------------- CONTROL CARD #2 ---------------------------*
*
* Input format [1]
* Number of materials [2]
* Number of node points [3]
* Number of brick elements [4]
* Number of beam elements [5]
* Number of shell elements [6]
* Number of 1D slide lines [7]
* Number of sliding interfaces [8]
* Number of rigid walls and symmetry planes [9]
* Discrete element input flag [10]
*
FL  3      2320      1680         0         0    0    0    0    0  0  240
*
*-------------------------- CONTROL CARD #3 ---------------------------*
*
* Number of time steps [1]
* Time step size [2]
* Automatic time step control flag [3]
* Maximum number of retries allowable per step [4]
* Optimal number of iterations per step [5]
* Minimum allowable step size [6]
* Maximum allowable step size [7]
* Size of the iteration window [8
*
       10 1.000E-01 auto    0   50 1.000E-03 1.000E-01    0
```

```
*
*------------------------- CONTROL CARD #4 --------------------------*
*
* Number of load curves [1]
* Maximum number of points defining any load curve [2]
* Number of concentrated nodal loads [3]
* Number of element surfaces having pressure loads applied [4]
* Number of displacement boundary condition cards [5]
* Number of beam elements with aerodynamic drag loads [6]
* Number of node constraint cards [7]
* Body force loads due to base acceleration in x-direction [8]
* Body force loads due to base acceleration in y-direction [9]
* Body force loads due to base acceleration in z-direction [10]
* Body force loads due to angular velocity about the x-direction [11]
* Body force loads due to angular velocity about the y-direction [12]
* Body force loads due to angular velocity about the z-direction [13]
*
   1    5    0    0    0    0    0    0    0    0    0    0    0    0    0
*
*------------------------- CONTROL CARD #5 --------------------------*
*
* Output print interval [1]
* Output plotting interval [2]
* Number of node printblocks [3]
* Number of brick printout blocks [4]
* Number of beam printout blocks [5]
* Number of shell printout blocks [6]
* Number of time steps between restart file generation [7]
* Shell surface strain dump flag [8]
* Initial sense switch toggles [9]
* Acceleration data dump flag [10]
*
  -1    1   -1   -1   -1    0  999    0    036000    0    0    0
*
*------------------------- CONTROL CARD #6 --------------------------*
*
* Method of iterating for equilibrium [1]
* Bandwidth minimization flag [2]
* Number of steps between stiffness reformations [3]
* Number of steps between equilibrium iterations [4]
* Maximum number of equilibrium iterations between stiffness matrix
*   reformations [5]
* Maximum number of stiffness matrix reformations per time step [6]
* Convergence tolerance on displacement [7]
* Convergence tolerance on energy [8]
* Convergence tolerance line search [9]
```

```
* Convergence tolerance for the augmented Lagrangian [10]
* Convergence tolerance on residuals [11]
*
   1    2         1         1   10   50 1.000E-03 1.000E-03       0.0       0.0
*
*-------------------------- CONTROL CARD #7 ---------------------------*
*
* Analysis type [1]
* Initial condition parameter [2]
* Thermal effects option [3]
* Temperature profile input flag [4]
* Number of eigenvalues and eigenvectors to be executed [5]
* Frequency shift, cycles per unit time [6]
* First Newmark integration parameter [7]
* Second Newmark integration parameter [8]
*
   0    0    0    0    0 0.000E+00 5.000E-01 2.500E-01
*
*-------------------------- CONTROL CARD #8 ---------------------------*
*
* Percent of memory option [1]
* Buffer size (words)element I/O [2]
* Stiffness matrix storage option [3]
* BFGS update vectors storage option [4]
* Brick element formulation [5]
* Brick element geometric stiffness flag [6]
* Shell element formulation [7]
* Hourglass control parameter (Belytschko-Tsay shell only) [8]
* Shell element geometric stiffness flag [9]
* Beam element formulation [10]
* Beam element geometric stiffness flag [11]
*
   0         0    2    2   10    2    0 0.000E+00    0    0    0
*
*-------------------------- CONTROL CARD #9 ---------------------------*
*
* Number of unloading steps in modified arc length method (optional) [1]
* Solution method during arc length unloading [2]
* Node number for displacement arc length method [3]
* Direction of displacement at arc length controlling node [4]
* Desired arc length [5]
* Arc length constraint method [6]
* Arc length damping option [7]
* Number of user-specified integration rules for beams [8]
* Maximum number of user-specified integration points [9]
* Number of user-specified integration rules for shells [10]
```

```
* Maximum number of user-specified integration points [11]
*
   0    0    0    0 0.000E+00    0    0    0    0    0    0
*
*------------------------- CONTROL CARD #10----------------------------*
*
* Linear equation solver option [1]
* Iteration limit for linear solver [2]
* Iteration convergence tolerance [3]
* Buffer size (element) for out-of-core iterative linear solver [4]
* Print-out option for linear iterative solver [5]
*
   0    0 0.000E+00    0    0    0
*
*--------------------------- MATERIAL CARDS ---------------------------*
*
   1   187.0000E-04    00.0000E+000.0000E+000.0000E+00
```

experimental material type

```
 0.100E+00   1.000E+01   0.000E+00   0.000E+00   0.000E+00   0.000E+00   0.000E+00
0.000E+00
 1.000E+03   1.000E+01   0.000E+00   0.000E+00   0.000E+00   0.000E+00   0.000E+00
0.000E+00
 0.000E+00   0.000E+00   0.000E+00   0.000E+00   0.000E-00   0.000E+00   0.000E+00
0.000E+00
 0.000E+00   0.000E+00   0.000E+00   0.000E+00   0.000E+00   0.000E+00   0.000E+00
0.000E+00
 0.000E+00   0.000E+00   0.000E+00   0.000E+00   0.000E+00   0.000E+00   0.000E+00
0.000E+00
 0.000E+00   0.000E+00   0.000E+00   0.000E+00   0.000E+00   0.000E+00   0.000E+00
0.000E+00
   2   201.0000E+03    00.0000E+000.0000E+000.0000E+00
```

mvn - rigid

```
 1.000E+04   0.000E+00   0.000E+00   0.000E+00   0.000E+00   0.000E+00   0.000E+00
0.000E+00
 3.000E-01   0.000E+00   0.000E+00   0.000E+00   0.000E+00   0.000E+00   0.000E+00
0.000E+00
-1.000E+00      1.000E+00-1.000E+00-1.000E+00-1.000E+00-1.000E+00      0.000E+00
0.000E+00
 1.000E+00   0.000E+01   0.000E+00   0.000E+00   0.000E+00   0.000E+00   0.000E+00
0.000E+00
 0.000E+00   0.000E+00   0.000E+00   0.000E+00   0.000E+00   0.000E+00   0.000E+00
0.000E+00
 0.000E+00   0.000E+00   0.000E+00   0.000E+00   0.000E+00   0.000E+00   0.000E+00
0.000E+00
   3   201.0000E+03    00.0000E+000.0000E+000.0000E+00
```

fxd - rigid

```
        1.000E+04   0.000E+00   0.000E+00   0.000E+00   0.000E+00   0.000E+00   0.000E+00
0.000E+00
        3.000E-01   0.000E+00   0.000E+00   0.000E+00   0.000E+00   0.000E+00   0.000E+00
0.000E+00
       -1.000E+00-1.000E+00-1.000E+00-1.000E+00-1.000E+00-1.000E+00          0.000E+00
0.000E+00
        1.000E+00   0.000E+01   0.000E+00   0.000E+00   0.000E+00   0.000E+00   0.000E+00
0.000E+00
        0.000E+00   0.000E+00   0.000E+00   0.000E+00   0.000E+00   0.000E+00   0.000E+00
0.000E+00
        0.000E+00   0.000E+00   0.000E+00   0.000E+00   0.000E+00   0.000E+00   0.000E+00
0.000E+00
        *
        *------------------------- NODE DEFINITIONS -------------------------*
        *
            1   0   -1.353617310524    -4.967348098755   -0.9049999713898   0
            2   0   -1.353617310524    -4.967348098755   -0.4524999856949   0
            3   0   -1.353617310524    -4.967348098755                0   0
            4   0   -1.353617310524    -4.967348098755    0.4524999856949   0
```

(cont'd …)

```
        *
        *---------------------- HEXAHEDRON ELEMENT DECK ----------------------*
        *
            1   1     1    81    86     6     2    82    87     7
            2   1     2    82    87     7     3    83    88     8
            3   1     3    83    88     8     4    84    89     9
```

(cont'd …)

```
        *
        *---------------------- RIGID NODES AND FACET DECK ----------------------*
        *
          2     6    86    81     1
          2     5    85    90    10
          2    11    91    86     6
          2    10    90    95    15
          2    16    96    91    11
          2    15    95   100    20
          2    21   101    96    16
          2    20   100   105    25
          2    26   106   101    21
          2    25   105   110    30
          2    31   111   106    26
          2    30   110   115    35
          2    36   116   111    31
```

2	35	115	120	40
2	41	121	116	36
2	40	120	125	45
2	46	126	121	41
2	45	125	130	50
2	51	131	126	46
2	50	130	135	55
2	56	136	131	51
2	55	135	140	60
2	61	141	136	56
2	60	140	145	65
2	66	146	141	61
2	65	145	150	70
2	71	151	146	66
2	70	150	155	75
2	76	156	151	71
2	75	155	160	80
2	86	166	161	81
2	85	165	170	90
2	91	171	166	86
2	90	170	175	95
2	96	176	171	91
2	95	175	180	100
2	101	181	176	96
2	100	180	185	105
2	106	186	181	101
2	105	185	190	110
2	111	191	186	106
2	110	190	195	115
2	116	196	191	111
2	115	195	200	120
2	121	201	196	116
2	120	200	205	125
2	126	206	201	121
2	125	205	210	130
2	131	211	206	126
2	130	210	215	135
2	136	216	211	131
2	135	215	220	140
2	141	221	216	136
2	140	220	225	145
2	146	226	221	141
2	145	225	230	150
2	151	231	226	146
2	150	230	235	155
2	156	236	231	151

2	155	235	240	160
2	166	246	241	161
2	165	245	250	170
2	171	251	246	166
2	170	250	255	175
2	176	256	251	171
2	175	255	260	180
2	181	261	256	176
2	180	260	265	185
2	186	266	261	181
2	185	265	270	190
2	191	271	266	186
2	190	270	275	195
2	196	276	271	191
2	195	275	280	200
2	201	281	276	196
2	200	280	285	205
2	206	286	281	201
2	205	285	290	210
2	211	291	286	206
2	210	290	295	215
2	216	296	291	211
2	215	295	300	220
2	221	301	296	216
2	220	300	305	225
2	226	306	301	221
2	225	305	310	230
2	231	311	306	226
2	230	310	315	235
2	236	316	311	231
2	235	315	320	240
2	246	326	321	241
2	245	325	330	250
2	251	331	326	246
2	250	330	335	255
2	256	336	331	251
2	255	335	340	260
2	261	341	336	256
2	260	340	345	265
2	266	346	341	261
2	265	345	350	270
2	271	351	346	266
2	270	350	355	275
2	276	356	351	271
2	275	355	360	280
2	281	361	356	276

2	280	360	365	285
2	286	366	361	281
2	285	365	370	290
2	291	371	366	286
2	290	370	375	295
2	296	376	371	291
2	295	375	380	300
2	301	381	376	296
2	300	380	385	305
2	306	386	381	301
2	305	385	390	310
2	311	391	386	306
2	310	390	395	315
2	316	396	391	311
2	315	395	400	320
3	1926	2006	2001	1921
3	1925	2005	2010	1930
3	1931	2011	2006	1926
3	1930	2010	2015	1935
3	1936	2016	2011	1931
3	1935	2015	2020	1940
3	1941	2021	2016	1936
3	1940	2020	2025	1945
3	1946	2026	2021	1941
3	1945	2025	2030	1950
3	1951	2031	2026	1946
3	1950	2030	2035	1955
3	1956	2036	2031	1951
3	1955	2035	2040	1960
3	1961	2041	2036	1956
3	1960	2040	2045	1965
3	1966	2046	2041	1961
3	1965	2045	2050	1970
3	1971	2051	2046	1966
3	1970	2050	2055	1975
3	1976	2056	2051	1971
3	1975	2055	2060	1980
3	1981	2061	2056	1976
3	1980	2060	2065	1985
3	1986	2066	2061	1981
3	1985	2065	2070	1990
3	1991	2071	2066	1986
3	1990	2070	2075	1995
3	1996	2076	2071	1991
3	1995	2075	2080	2000
3	2006	2086	2081	2001

3 2005 2085 2090 2010
3 2011 2091 2086 2006
3 2010 2090 2095 2015
3 2016 2096 2091 2011
3 2015 2095 2100 2020
3 2021 2101 2096 2016
3 2020 2100 2105 2025
3 2026 2106 2101 2021
3 2025 2105 2110 2030
3 2031 2111 2106 2026
3 2030 2110 2115 2035
3 2036 2116 2111 2031
3 2035 2115 2120 2040
3 2041 2121 2116 2036
3 2040 2120 2125 2045
3 2046 2126 2121 2041
3 2045 2125 2130 2050
3 2051 2131 2126 2046
3 2050 2130 2135 2055
3 2056 2136 2131 2051
3 2055 2135 2140 2060
3 2061 2141 2136 2056
3 2060 2140 2145 2065
3 2066 2146 2141 2061
3 2065 2145 2150 2070
3 2071 2151 2146 2066
3 2070 2150 2155 2075
3 2076 2156 2151 2071
3 2075 2155 2160 2080
3 2086 2166 2161 2081
3 2085 2165 2170 2090
3 2091 2171 2166 2086
3 2090 2170 2175 2095
3 2096 2176 2171 2091
3 2095 2175 2180 2100
3 2101 2181 2176 2096
3 2100 2180 2185 2105
3 2106 2186 2181 2101
3 2105 2185 2190 2110
3 2111 2191 2186 2106
3 2110 2190 2195 2115
3 2116 2196 2191 2111
3 2115 2195 2200 2120
3 2121 2201 2196 2116
3 2120 2200 2205 2125
3 2126 2206 2201 2121

```
   3   2125   2205   2210   2130
   3   2131   2211   2206   2126
   3   2130   2210   2215   2135
   3   2136   2216   2211   2131
   3   2135   2215   2220   2140
   3   2141   2221   2216   2136
   3   2140   2220   2225   2145
   3   2146   2226   2221   2141
   3   2145   2225   2230   2150
   3   2151   2231   2226   2146
   3   2150   2230   2235   2155
   3   2156   2236   2231   2151
   3   2155   2235   2240   2160
   3   2166   2246   2241   2161
   3   2165   2245   2250   2170
   3   2171   2251   2246   2166
   3   2170   2250   2255   2175
   3   2176   2256   2251   2171
   3   2175   2255   2260   2180
   3   2181   2261   2256   2176
   3   2180   2260   2265   2185
   3   2186   2266   2261   2181
   3   2185   2265   2270   2190
   3   2191   2271   2266   2186
   3   2190   2270   2275   2195
   3   2196   2276   2271   2191
   3   2195   2275   2280   2200
   3   2201   2281   2276   2196
   3   2200   2280   2285   2205
   3   2206   2286   2281   2201
   3   2205   2285   2290   2210
   3   2211   2291   2286   2206
   3   2210   2290   2295   2215
   3   2216   2296   2291   2211
   3   2215   2295   2300   2220
   3   2221   2301   2296   2216
   3   2220   2300   2305   2225
   3   2226   2306   2301   2221
   3   2225   2305   2310   2230
   3   2231   2311   2306   2226
   3   2230   2310   2315   2235
   3   2236   2316   2311   2231
   3   2235   2315   2320   2240
*
*------------------------- LOAD CURVE DECK -------------------------*
*
```

* y-displacement of moving clamp
1 2
0.000E+00 0.000E+00
1.000E+00 5.600E+00

BIBLIOGRAPHY

1. DePalma, A.F., Callery, G., Bennett, G.A.: Variational anatomy and degenerative lesions of the shoulder joint. *American Academy of Orthopaedic Surgery Instructional Course Lecture Series* 6:225-81, 1949.

2. O'Brien, S.J., Arnoczsky, S.P., Warren, R.F., Rozbruch, S.R.: Developmental anatomy of the shoulder and anatomy of the glenohumeral joint. In: *The Shoulder,* ed by Matsen, F.A., 3rd and Rockwood, C.A., Philadelphia, PA, W. B. Saunders Co., 1990, pp 1-33.

3. Bigliani, L.U., Pollock, R.G., Soslowsky, L.J., Flatow, E.L., Pawluk, R.J., Mow, V.C.: Tensile properties of the inferior glenohumeral ligament. *J Orthop Res* 10(2):187-97, 1992.

4. McMahon, P.J., Dettling, J.R., Sandusky, M.D., Lee, T.Q.: Deformation and strain characteristics along the length of the anterior band of the inferior glenohumeral ligament. *J Shoulder Elbow Surg* 10(5):482-8, 2001.

5. Turkel, S.J., Panio, M.W., Marshall, J.L., Girgis, F.G.: Stabilizing mechanisms preventing anterior dislocation of the glenohumeral joint. *J Bone Joint Surg Am* 63(8):1208-17, 1981.

6. Itoi, E., Grabowski, J.J., Morrey, B.F., An, K.N.: Capsular properties of the shoulder. *Tohoku J Exp Med* 171(3):203-10, 1993.

7. Ferrari, D.A.: Capsular ligaments of the shoulder. Anatomical and functional study of the anterior superior capsule. *Am J Sports Med* 18(1):20-4, 1990.

8. Flood, V.: Discovery of a new ligament of the shoulder joint. *Lancet*:671, 1829.

9. Sarrafian, S.K.: Gross and functional anatomy of the shoulder. *Clin Orthop* (173):11-9, 1983.

10. Bost, F.C. and Inman, V.T.: The pathological changes in recurrent dislocation of the shoulder. *J Bone Joint Surg Am* 24A:595, 1942.

11. Rowe, C.R., Patel, D., Southmayd, W.W.: The Bankart procedure: a long-term end-result study. *J Bone Joint Surg Am* 60(1):1-16, 1978.

12. Neer, C.S., 2nd and Foster, C.R.: Inferior capsular shift for involuntary inferior and multidirectional instability of the shoulder. A preliminary report. *J Bone Joint Surg Am* 62(6):897-908, 1980.

13. Warner, J.J.P., Caborn, D.N., Berger, R., Fu, F.H., Seel, M.: Dynamic capsuloligamentous anatomy of the glenohumeral joint. *J Shoulder Elbow Surg* 2:115-33, 1993.

14. Warner, J.J.P., Deng, X.H., Warren, R.F., Torzilli, P.A.: Static capsuloligamentous restraints to superior-inferior translation of the glenohumeral joint. *Am J Sports Med* 20(6):675-85, 1992.

15. Schwartz, R.E., O'Brien, S.J., Warren, R.F., Torzilli, P.A.: Capsular restraints to anterior-posterior motion of the abducted shoulder. A biomechanical study. *Orthopaedic Transactions* 12:727, 1988.

16. Gohlke, F., Essigkrug, B., Schmitz, F.: The patterns of the collagen fiber bundles of the capsule of the glenohumeral joint. *J Shoulder Elbow Surg* 3(3):111-28, 1994.

17. O'Brien, S.J., Neves, M.C., Arnoczky, S.P., Rozbruck, S.R., Dicarlo, E.F., Warren, R.F., Schwartz, R., Wickiewicz, T.L.: The anatomy and histology of the inferior glenohumeral ligament complex of the shoulder. *Am J Sports Med* 18(5):449-56, 1990.

18. Clark, J.M. and Harryman, D.T., 2nd: Tendons, ligaments, and capsule of the rotator cuff. Gross and microscopic anatomy. *J Bone Joint Surg Am* 74(5):713-25, 1992.

19. Cooper, D.E., Arnoczky, S.P., O'Brien, S.J., Warren, R.F., DiCarlo, E., Allen, A.A.: Anatomy, histology, and vascularity of the glenoid labrum. An anatomical study. *J Bone Joint Surg Am* 74(1):46-52, 1992.

20. Debski, R.E., Moore, S.M., Mercer, J.L., Sacks, M.S., McMahon, P.J.: The collagen fibers of the anteroinferior capsulolabrum have multi-axial orientation to resist shoulder dislocation. *J Shoulder Elbow Surg* in press2002.

21. Boardman, N.D., Debski, R.E., Warner, J.J., Taskiran, E., Maddox, L., Imhoff, A.B., Fu, F.H., Woo, S.L.-Y.: Tensile properties of the superior glenohumeral and coracohumeral ligaments. *J Shoulder Elbow Surg* 5(4):249-54, 1996.

22. Ticker, J.B., Bigliani, L.U., Soslowsky, L.J., Pawluk, R.J., Flatow, E.L., Mow, V.C.: Inferior glenohumeral ligament: geometric and strain-rate dependent properties. *J Shoulder Elbow Surg* 5(4):269-79, 1996.

23. McMahon, P.J., Dettling, J., Sandusky, M.D., Tibone, J.E., Lee, T.Q.: The anterior band of the inferior glenohumeral ligament. Assessment of its permanent deformation and the anatomy of its glenoid attachment. *J Bone Joint Surg Br* 81(3):406-13, 1999.

24. McMahon, P.J., Tibone, J.E., Cawley, P.W., Hamilton, C., Fechter, J.D., Elattrache, N.S., Lee, T.Q.: The anterior band of the inferior glenohumeral ligament: biomechanical properties from tensile testing in the position of apprehension. *J Shoulder Elbow Surg* 7(5):467-71, 1998.

25. Lee, T.Q., Dettling, J., Sandusky, M.D., McMahon, P.J.: Age related biomechanical properties of the glenoid-anterior band of the inferior glenohumeral ligament-humerus complex. *Clin Biomech (Bristol, Avon)* 14(7):471-6, 1999.

26. Stefko, J.M., Tibone, J.E., Cawley, P.W., ElAttrache, N.E., McMahon, P.J.: Strain of the anterior band of the inferior glenohumeral ligament during capsule failure. *J Shoulder Elbow Surg* 6(5):473-9, 1997.

27. Moore, S.M., McMahon, P.J., Debski, R.E.: Bi-directional Mechanical Properties of the Axillary Pouch of the Glenohumeral Capsule: Implications for Surgical Repair. *J Biomech Eng* 126(2):284-288, 2004.

28. Debski, R.E., Wong, E.K., Woo, S.L.-Y., Sakane, M., Fu, F.H., Warner, J.J.: In situ force distribution in the glenohumeral joint capsule during anterior-posterior loading. *J Orthop Res* 17(5):769-76, 1999.

29. Ovesen, J. and Nielsen, S.: Stability of the shoulder joint. Cadaver study of stabilizing structures. *Acta Orthop Scand* 56(2):149-51, 1985.

30. Malicky, D.M., Soslowsky, L.J., Blasier, R.B., Shyr, Y.: Anterior glenohumeral stabilization factors: progressive effects in a biomechanical model. *J Orthop Res* 14(2):282-8, 1996.

31. Warner, J.J.P., Deng, X.H., Warren, R.F., Torzilli, P.A., O'Brien, S.J.: Superior-inferior translation in the intact and vented glenohumeral joint. *J Shoulder Elbow Surg* 2(2):99-105, 1993.

32. Hoffmeyer, P., Browne, A., Korinek, S., Morrey, B.F., An, K.N.: Stabilizing mechanism of the glenohumeral ligaments. *Biomed Sci Instrum* 26:49-52, 1990.

33. O'Connell, P.W., Nuber, G.W., Mileski, R.A., Lautenschlager, E.: The contribution of the glenohumeral ligaments to anterior stability of the shoulder joint. *Am J Sports Med* 18(6):579-84, 1990.

34. Terry, G.C., Hammon, D., France, P., Norwood, L.A.: The stabilizing function of passive shoulder restraints. *Am J Sports Med* 19(1):26-34, 1991.

35. Miller, M.C., Smolinski, P.J., Bains, P.K., Klein, A.H., Fu, F.H.: A mathematical and experimental model of length change in the inferior glenohumeral ligament in the late cocking phase of pitching. *Transcripts of the Orthopaedic Research Society* 16:609, 1991.

36. Malicky, D.M., Soslowsky, L.J., Kuhn, J.E., Bey, M.J., Mouro, C.M., Raz, J.A., Liu, C.A.: Total strain fields of the antero-inferior shoulder capsule under subluxation: a stereoradiogrammetric study. *J Biomech Eng* 123(5):425-31, 2001.

37. Moseley, H. and Overgaard, B.: The anterior capsular mechanism in recurrent anterior dislocation of the shoulder: Morphological and clinical studies with special reference to the glenoid labrum and glenohumeral ligaments. *J Bone Joint Surg Br* 44:913-27, 1962.

38. Peat, M.: Functional anatomy of the shoulder complex. *Phys Ther* 66(12):1855-65, 1986.

39. Lew, W.D., Lewis, J.L., Craig, E.V.: Stabilization by capsule, ligaments, and labrum: Stability at the extremes of motion. In: *The Shoulder: A Balance of Mobility and Stability,* ed by Matsen, F.A., 3rd, Fu, F.H., and Hawkins, R.J., Rosemont, IL, American Academy of Orthopaedic Surgeons, 1993, pp 69-90.

40. Debski, R.E., Wong, E.K., Woo, S.L.-Y., Fu, F.H., Warner, J.J.: An analytical approach to determine the in situ forces in the glenohumeral ligaments. *J Biomech Eng* 121(3):311-5, 1999.

41. Novotny, J.E., Beynnon, B.D., Nichols, C.E.: Modeling the stability of the human glenohumeral joint during external rotation. *J Biomech* 33(3):345-54, 2000.

42. Cave, E., Burke, J., Boyd, R., *Trauma Management*. 1974, Chicago, IL: Year Book Medical Publishers. 437.

43. Hawkins, R.J. and Mohtadi, N.G.: Controversy in anterior shoulder instability. *Clin Orthop Relat Res* (272):152-61, 1991.

44. Arciero, R.A., Wheeler, J.H., Ryan, J.B., McBride, J.T.: Arthroscopic Bankart repair versus nonoperative treatment for acute, initial anterior shoulder dislocations. *Am J Sports Med* 22(5):589-94, 1994.

45. Baker, C.L., Uribe, J.W., Whitman, C.: Arthroscopic evaluation of acute initial anterior shoulder dislocations. *Am J Sports Med* 18(1):25-8, 1990.

46. Caspari, R.B.: Arthroscopic reconstruction for anterior shoulder instability. *Techniques in Orthopaedics* 3:59-66, 1988.

47. Field, L.D., Bokor, D.J., Savoie, F.H., 3rd: Humeral and glenoid detachment of the anterior inferior glenohumeral ligament: a cause of anterior shoulder instability. *J Shoulder Elbow Surg* 6(1):6-10, 1997.

48. Morgan, C.D. and Bodenstab, A.B.: Arthroscopic Bankart suture repair: technique and early results. *Arthroscopy* 3(2):111-22, 1987.

49. Nelson, B.J. and Arciero, R.A.: Arthroscopic management of glenohumeral instability. *Am J Sports Med* 28(4):602-14, 2000.

50. Hovelius, L.: Incidence of shoulder dislocation in Sweden. *Clin Orthop* (166):127-31, 1982.

51. *United States Census 2000*. 2000, United States Census Bureau:

52. Hovelius, L.: Shoulder dislocation in Swedish ice hockey players. *Am J Sports Med* 6(6):373-7, 1978.

53. Zebas, C.J., Loudon, K., Chapman, M., Magee, L., Bowman, S.: Musculoskeletal injuries in a college-age population during a 1-semester term. *J Am Coll Health* 44(1):32-4, 1995.

54. Mahaffey, B.L. and Smith, P.A.: Shoulder instability in young athletes. *American Family Physician* 59(10):2773-82, 1999.

55. Henry, J.H. and Genung, J.A.: Natural history of glenohumeral dislocation--revisited. *Am J Sports Med* 10(3):135-7, 1982.

56. Hovelius, L.: Anterior dislocation of the shoulder in teen-agers and young adults. Five-year prognosis. *J Bone Joint Surg Am* 69(3):393-9, 1987.

57. McLaughlin, H.L. and MacLellan, D.I.: Recurrent anterior dislocation of the shoulder. II. A comparative study. *J Trauma* 7(2):191-201, 1967.

58. Rowe, C.R., Zarins, B., Ciullo, J.V.: Recurrent anterior dislocation of the shoulder after surgical repair. Apparent causes of failure and treatment. *J Bone Joint Surg Am* 66(2):159-68, 1984.

59. Simonet, W.T. and Cofield, R.H.: Prognosis in anterior shoulder dislocation. *Am J Sports Med* 12(1):19-24, 1984.

60. Wheeler, J.H., Ryan, J.B., Arciero, R.A., Molinari, R.N.: Arthroscopic versus nonoperative treatment of acute shoulder dislocations in young athletes. *Arthroscopy* 5(3):213-7, 1989.

61. Neviaser, R.J., Neviaser, T.J., Neviaser, J.S.: Anterior dislocation of the shoulder and rotator cuff rupture. *Clin Orthop* (291):103-6, 1993.

62. Bigliani, L.U., Kurzweil, P.R., Schwartzbach, C.C., Wolfe, I.N., Flatow, E.L.: Inferior capsular shift procedure for anterior-inferior shoulder instability in athletes. *Am J Sports Med* 22(5):578-84, 1994.

63. Montgomery, W.H., 3rd and Jobe, F.W.: Functional outcomes in athletes after modified anterior capsulolabral reconstruction. *Am J Sports Med* 22(3):352-8, 1994.

64. Sperber, A., Hamberg, P., Karlsson, J., Sward, L., Wredmark, T.: Comparison of an arthroscopic and an open procedure for posttraumatic instability of the shoulder: a prospective, randomized multicenter study. *J Shoulder Elbow Surg* 10(2):105-8, 2001.

65. Moore, S.M., McMahon, P.J., Azemi, E., Debski, R.E.: Bi-directional mechanical properties of the posterior region of the glenohumeral capsule. *J Biomech* 38(6):1365-9, 2005.

66. Reeves, B.: Experiments on the tensile strength of the anterior capsular structures of the shoulder in man. *J Bone Joint Surg Br* 50(4):858-65, 1968.

67. Weiss, J.A., Gardiner, J.C., Bonifasi-Lista, C.: Ligament material behavior is nonlinear, viscoelastic and rate-independent under shear loading. *J Biomech* 35(7):943-50, 2002.

68. Marsden, J.E.a.H., T. J. R.: *Mathematical Foundations of Elasticity* 1983.

69. Gardiner, J.C. and Weiss, J.A.: Simple shear testing of parallel-fibered planar soft tissues. *Journal of Biomechanics* 123:1-5, 2001.

70. Sacks, M.S.: Biaxial mechanical evaluation of planar biological materials. *Journal of Elasticity* 61:199-246, 2000.

71. Runciman, R.J., Bryant, J.T., Small, C.F., Fujita, N., Cooke, T.D.: Stereoradiogrammetric technique for estimating alignment of the joints in the hand and wrist. *Journal of Biomedical Engineering* 15(2):99-105, 1993.

72. Weiss, J.A., Maker, B.N., Govindjee, S.: Finite element implementation of incompressible, transversely isotropic hyperelasticity. *Comp Meth Appl Mech Eng* 135:107-28, 1996.

73. Veronda, D.R. and Westmann, R.A.: Mechanical characterization of skin-finite deformations. *Journal of Biomechanics* 3:111-124, 1970.

74. Marsden, J.E. and Hughes, T.J.R.: Mathematical Foundations of Elasticity. 1994.

75. Chen, S., Haen, P.S., Walton, J., Murrell, G.A.: The effects of thermal capsular shrinkage on the outcomes of arthroscopic stabilization for primary anterior shoulder instability. *Am J Sports Med* 33(5):705-11, 2005.

76. Levine, W.N., Bigliani, L.U., Ahmad, C.S.: Thermal capsulorrhaphy. *Orthopedics* 27(8):823-6, 2004.

77. Simo, J.C.: On the dynamics in space of rods undergoing large motions: A geometrically exact approach. *Comp Meth Appl Mech Eng* 66:125-161, 1988.

78. Bey, M.J., Hunter, S.A., Kilambi, N., Butler, D.L., Lindenfeld, T.N.: Structural and mechanical properties of the glenohumeral joint posterior capsule. *J Shoulder Elbow Surg* 14(2):201-6, 2005.